UNCLASSIFIED

AD NUMBER

AD402336

NEW LIMITATION CHANGE

TO

Approved for public release, distribution unlimited

FROM

Distribution authorized to U.S. Gov't. agencies and their contractors; Administrative/Operational Use; Feb 1963. Other requests shall be referred to Rome Air Development Center, Research & Technology Div., AFSC, Griffiss AFB, NY

AUTHORITY

RADC ltr dtd 20 Dec 1965

THIS PAGE IS UNCLASSIFIED

This Document
Reproduced From
Best Available Copy

UNCLASSIFIED

AD 402336

DEFENSE DOCUMENTATION CENTER

FOR

SCIENTIFIC AND TECHNICAL INFORMATION

CAMERON STATION, ALEXANDRIA, VIRGINIA

UNCLASSIFIED

NOTICE: When government or other drawings, specifications or other data are used for any purpose other than in connection with a definitely related government procurement operation, the U. S. Government thereby incurs no responsibility, nor any obligation whatsoever; and the fact that the Government may have formulated, furnished, or in any way supplied the said drawings, specifications, or other data is not to be regarded by implication or otherwise as in any manner licensing the holder or any other person or corporation, or conveying any rights or permission to manufacture, use or sell any patented invention that may in any way be related thereto.

This Document
Reproduced From
Best Available Copy

402336

RADC-TDR-63-80

February 1963

FINAL REPORT ~~ON~~
NEW METHODS FOR MEASURING SPURIOUS EMISSIONS

by

J. Goldberg, O. F. Hinckelmann, L. J. Kuskowski,
D. S. Levinson, R. L. Sleven, and J. J. Taub

AD No.
ASTIA FILE COPY

REPORT NO. 1112-1
CONTRACT AF 30(602)-2511

Prepared for

ROME AIR DEVELOPMENT CENTER
Research and Technology Division
Air Force Systems Command
United States Air Force
Griffiss AFB
New York

ASTIA

This document is furnished under U.S. Government, Contract No. AF 30(602)-2511 and shall not be used, or duplicated for procurement or manufacturing purposes, except as otherwise authorized by said contract without the permission of Airborne Instruments Laboratory, a Division of Cutler-Hammer. This legend shall be marked on any reproduction thereof in whole or in part.

AIRBORNE INSTRUMENTS LABORATORY
A DIVISION OF CUTLER-HAMMER, INC.

Deer Park, Long Island, New York

NO OTS 402336

(15) - (26750)

17

(13) 765700 RADC-TDR-63-80

(9) February 1963

(7) FINAL REPORT, ~~ON~~

(6) NEW METHODS FOR MEASURING SPURIOUS EMISSIONS

(8) by

J. Goldberg, O. F. Hinckelmann, ~~L. J. Kuskowski~~,
~~D. S.~~ Levinson, R. L. Sleven, and J. J. Taub and others.

(10) iv. unpaginated, tables, 12 refs.

(11) REPORT NO. 1112-1

(15) CONTRACT AF 30(602)-2511,

PRO~~JECT NO~~. 4540

TASK NO. 454001

Prepared for

ROME AIR DEVELOPMENT CENTER
Research and Technology Division
Air Force Systems Command
United States Air Force
Griffiss AFB
New York

G. C.

This document is furnished under U.S. Government Contract No. AF 30(602)-2511 and shall not be used, or duplicated for procurement or manufacturing purposes, except as otherwise authorized by said contract without the permission of Airborne Instruments Laboratory, a Division of Cutler-Hammer. This legend shall be marked on any reproduction thereof in whole or in part.

AIRBORNE INSTRUMENTS LABORATORY
A DIVISION OF CUTLER-HAMMER, INC.

Deer Park, Long Island, New York

NOTICES

Qualified requestors may obtain copies from ASTIA. Orders will be expedited if placed through the librarian or other person designated to request documents from ASTIA.

This document may be reproduced to satisfy official needs of U.S. Government Agencies. No other reproduction authorized except with permission of: Commander,
RADC (ATTN: RAUMA)
GRIFFISS AFB NY

LEGAL NOTICES

When U. S. Government drawings, specifications, or other data are used for any purpose other than a definitely related government procurement operation, the government thereby incurs no responsibility nor any obligation whatsoever; and the fact that the government may have formulated, furnished, or in any way supplied the said drawings, specifications, or other data is not to be regarded by implication or otherwise, as in any manner licensing the holder or any other person or corporation, or conveying any rights or permission to manufacture, use, or sell any patented invention that may in any way be related thereto.

This document made available for study upon the understanding that the U. S. Government's proprietary interests in and relating thereto shall not be impaired. In case of apparent conflict between the government's proprietary interests and those of others, notify the Staff Judge Advocate, Air Force Systems Command, Andrews Air Force Base, Washington 25, D.C.

FOREWORD

This is the Final Report on Contract AF 30(602)-2511 entitled "New Methods for Measuring Spurious Emissions". The report describes the effort expended in the investigation of new methods for measuring the spurious emission power of microwave transmitters. This work was sponsored by Rome Air Development Center, Research and Technology Division, Air Force Systems Command, United States Air Force, Griffiss Air Force Base, New York. The management and technical supervision of this program was under the cognizance of Messrs. R. Powers and L. F. Moses of RADC.

Reproduced From
Best Available Copy

This Document
Reproduced From
Best Available Copy

Final Report on New Methods for Measuring
Spurious Emissions
RADC-TDR-63-80

ABSTRACT

Newer, simpler, and more accurate methods of measuring the spurious-emission power of microwave transmitters were ~~have been~~ investigated. Two of these methods--the fixed-probe and the movable-probe methods--measure the power in the waveguide. A third, the free-space method, measures the power outside the transmission line. All of the methods are capable of accuracies of ±1 db or better.

In all three methods, the electric-field amplitude is measured in a region where the modal phase constants and the wave impedance have essentially their free-space values. For the waveguide methods, this region is an oversize section of waveguide. For the free-space method, this region is outside the transmission line.

The fixed-probe method lends itself most readily to automatic instrumentation and ~~has~~ received the greatest emphasis during this program. Instrumentation was ~~has been~~ developed to measure peak power levels as low as -40 dbm in the 3 to 10 Gc frequency range in less than 5 minutes per frequency.

Primary emphasis was ~~has been~~ on measurements of power flow into matched loads. However, the extension of the fixed-probe method to the measurement of power transferred into mismatched loads is also described.

Final Report on New Methods for Measuring
Spurious Emissions
RADC-TDR-63-80

PUBLICATION REVIEW

This report has been reviewed and is approved.

Approved: Louis F. Moses
LOUIS F. MOSES
Task Engineer
Applied Research Branch

Approved: Samuel D. Zaccari
SAMUEL D. ZACCARI, Chief
Electromagnetic Vulnerability Lab
Directorate of Communications

FOR THE COMMANDER: Irving J. Gabelman
IRVING J. GABELMAN
Director of Advanced Studies

This Document
Reproduced From
Best Available Copy

TABLE OF CONTENTS

		Page
	Abstract	iii
A.	Introduction	1
B.	Fixed-Probe Method	5
	1. Theory of Operation	5
	2. Trombone Line Stretcher	6
	3. Taper	9
	4. Fixed-Probe Section	10
	5. Multimode High-Power Load	12
	6. Probe-Sampling Commutators	13
	7. Receiver	14
	8. Averaging Amplifier	16
	9. Packaging	19
	10. Experimental Results	20
	11. Calibration	25
	12. Multimode Power Flow with Mismatched Terminations	27
C.	Movable-Probe Method	29
	1. Theory of Operation	29
	2. Taper	31
	3. Enlarged Waveguide Section	31
	4. Probe and Carriage Assemblies	31
	5. Multimode Load	37
D.	Free-Space Method	39
	1. Theory	39
	2. Scanning Dipole Probe	42
	3. Rotating Scatterer	43
	4. Multiple Stationary Probes	45
E.	Conclusions	47
F.	References	49

Reproduced From
Best Available Copy

		Page
Appendices		
I.	Power Flow in Rectangular Waveguide in Terms of Power Measured by Probes at the Boundary	I-1
II.	Power Flow in Multimode Rectangular Waveguide	II-1
III.	Power Flow in Enlarged Waveguide	III-1
IV.	Determination of Average Probe Power Using a Commutator-Averaging Technique	IV-1
V.	Commutator Averaging Correction	V-1
VI.	Derivation of Receiver Noise Figure and Bandwidth Product	VI-1
VII.	Difference Between Top-Wall and Bottom-Wall Electric Fields for TE_{10}- and TE_{51}- Mode Propagation	VII-1
VIII.	Measurements in Presence of Multimode Mismatches	VIII-1

Reproduced From
Best Available Copy

LIST OF ILLUSTRATIONS

Figure	
1	Block Diagram of Fixed Probe Multimode Spurious Emission Power Measuring Equipment
2	Trombone Line Stretcher
3	Top- and Bottom-Wall Electric Field Plots, with Straight and Trombone Line Stretchers
4	Nonlinear Taper
5	Comparison of Measured TE_{10} Electric-Field Amplitude Transformed by Four Tapers to Theoretical TE_{10} Electric-Field Amplitude
6	Fixed Probe
7	Noncontacting Commutator
8	Band I Commutator, Typical Transfer Function
9	Probe-Sampling Unit
10	Upper-Limit Error vs Power Level
11	Block Diagram of Averaging Amplifier
12	Output of Squaring Amplifier vs Commutator Rotation Angle
13	Charge-Storage-Circuit Voltage vs Commutator Rotation Angle
14	Averaging Amplifier Chassis
15	Waveguide Components and Supporting Carts
16	Control Panel
17	Instrumentation Rack
18	Measured TE_{10} Electric-Field Amplitude at 4.3 Gc
19	Mode Launcher
20	Measured TE_{20} Electric-Field Amplitude at 4.3 Gc
21	Measured TE_{10} and TE_{20} Electric-Field Amplitude at 4.3 Gc for Various Dispersive Lengths
22	Measured Multimode Electric-Field Amplitude at 7.0 Gc for Various Dispersive Lengths
23	Ratio of Waveguide Power to Average Probe-Coupled Power vs Length of Dispersive Line Stretcher

Reproduced From
Best Available Copy

Figure

24 Averaging Amplifier Calibration Curve

25 Fixed Probe Calibration Constant

26 Diagram of Equipment to Measure Spurious Emission Power Absorbed by Mismatched Antenna

27 Enlarged Waveguide and Arrangement of Movable Probes for Measuring $|E_x|$ and $|E_y|$

28 Probe and Carriage Assembly and Probe and Enlarged Section of Waveguide

29 Slotted Balanced Dipole Probe

30 TE_{10} Electric-Field Amplitude Measured with Slotted Dipole at 3.8 Gc

31 Balanced Dipole Probe

32 TE_{10} Electric-Field Amplitude Measured with Balanced Dipole Probe at 4.3 Gc

33 TE_{20} Electric-Field Amplitude Obtained with Balanced Dipole Probe at 4.3 Gc

34 Z-Axis Balanced Dipole Probe

35 Electric-Field Plot Obtained with $|E_x|$ and $|E_y|$ Probes with Dominant Mode Propagating in Small Guide at 3.8 Gc

36 Free-Space Measurement Setup

37 Comparison of Densities of Measured Power and Computed Power of S-Band Horn for TE_{10} Mode

I-1 Cross Section of Enlarged Waveguide with Fixed Probes

II-1 Coordinate System for Rectangular Waveguide

IV-1 Transmission as a Function of Rotor Angle for a Single Commutator Segment

IV-2 Transmission as a Function of Rotor Angle for all Commutator Segments

IV-3 Output Power as a Function of Rotor Angle for all Commutator Segments

VI-1 E-Field Distribution with TE_{30}

VI-2 Receiver Output when Noise is Present in Receiver

VII-1 TE_{10} and TE_{51} Electric-Field Amplitude for R = 20 DB

VII-2 TE_{10} and TE_{51} Electric-Field Amplitude for R = 25 DB

Reproduced From Best Available Copy

A. INTRODUCTION

This report describes the effort expended on Contract AF 30(602)-2511 in investigating new methods for measuring the spurious emission power of microwave transmitters.

The complexity of the measurement problem is due almost entirely to the large number of modes in which the spurious emission power can propagate. Conventional (dominant mode) power measuring equipment cannot be used to measure multimode power unless the modes and the relative power in each mode are known. In practice, these powers are not known, and, therefore, multimode power measuring equipment is required.

Previously, methods for measuring the power of harmonic and anharmonic spurious emission were developed by Forrer and Tomiyasu, Price, and Lewis (references 1, 2, and 3).

Forrer and Tomiyasu used a movable-probe assembly in standard-size waveguide to measure the amplitude and phase of the electric field on the walls. By performing a Fourier analysis on the measured data, the power propagating in each mode was determined. A computer was required to analyze the data at each frequency at which measurements were made. The authors reported that their probe tended to arc while being moved in the waveguide. For this reason, the transmitter was turned off between measurements, thereby precluding repeatability in the measurements.

Price developed a fixed-probe technique to measure the electric fields normal to the boundary of a standard-size waveguide. The power in each mode was then calculated in a manner similar to that used by Forrer and Tomiyasu. Price's

method eliminated the problem of arcing, but computer services were still required to reduce the data at each measurement frequency.

Lewis developed a series of mode couplers, each of which selectively couples a given mode to a separate output port. By calibrating the mode couplers, it was possible to measure the total spurious-emission power by summing the power at each output port. This method is satisfactory if the spurious-emission power is concentrated in a known limited number of modes.

During the present program, three methods of measuring the multimode spurious-emission power were investigated--a fixed-probe method and a movable-probe method, which measure the power in an oversize section of waveguide, and a free-space method, which measures the power outside the transmission line. The goal of the investigation was to develop a measuring technique that avoided the limitations of the earlier methods--that is, the need for computer services, breakdown at high powers, and the dependence of accuracy on the propagating modes.

The fixed-probe method is based on averaging the power coupled by 36 short electric probes located on the periphery of an enlarged section of waveguide. In the enlarged section the phase constant and the wave impedance for all the modes that can exist in the standard-size waveguide are essentially equal. With this type of propagation, the equations for power flow are greatly simplified and the average of the power coupled by the probes is proportional to the waveguide power plus an error term. This error term is caused by the presence of certain mode pairs in the waveguide. When these modes are present, their effect on the coupled power is canceled to a great extent by adjusting a line stretcher in the standard-size waveguide for maximum and minimum coupled power and averaging the results. Measurements made over the 3 to 10 Gc frequency range showed an accuracy of 1 db or better.

The fixed-probe method lends itself to automatic sampling techniques that enable spurious-emission power to be measured rapidly. Continuously rotating probe-sampling commutators and an averaging circuit were designed and fabricated. A receiver has been incorporated in the system to facilitate the measurement of spurious-emission power levels of -35 to -40 dbm over the 3 to 10 Gc frequency range. To demonstrate the feasibility of the technique, the waveguide components have been designed to make spurious-emission measurements in S-band waveguide.

The movable-probe method that was investigated used a scanning electric probe to measure the electric-field amplitude over a plane transverse to the direction of propagation in an oversize section of waveguide. Two balanced dipole probes are used to measure the vertically and horizontally polarized components of the electric field. Measurements made at 4.3 and 5.0 Gc gave an accuracy of 0.44 db or better.

Three free-space methods of measuring spurious-emission power were also investigated during this program--a scanning dipole probe, a scanning passive scatterer, and multiple stationary probes. The most successful technique, the scanning dipole probe, is very similar to the in-guide movable-probe method.

B. FIXED-PROBE METHOD

The fixed-probe method of measuring spurious-emission multimode power flow is based on averaging the power coupled by a number of short electric probes located on the periphery of an enlarged section of waveguide. This method has been automated to permit rapid measurements of spurious-emission power. The equipment required for this automated method is: a line stretcher, a taper to the enlarged waveguide, a section of enlarged waveguide for mounting the fixed probes, a multimode matched termination, probe-sampling commutators, a microwave detector, and an electronic circuit to average the power coupled by the probes. A block diagram of the equipment is shown in Figure 1. The underlying theory of operation and the development of this equipment are described in this section. The modifications required to measure the spurious-emission multimode power transferred to mismatched loads is also discussed.

1. THEORY OF OPERATION

In Appendix I, it is shown that the average of the power coupled by a large number of probes located on the periphery of an enlarged section of waveguide is given by:

$$P = C_p P_p + \varepsilon$$

where

C_p = calibration constant,

ε = error term,

P_p = average of power coupled by probes.

Preceding Page Blank

There are two theoretical sources of error in the actual measurement of the waveguide power. The first is due to the term $\mathcal{E}$. $\mathcal{E}$ will be non-zero only if certain mode pairs are present in the waveguide. In S-band guide, $\mathcal{E}$ can be non-zero only above 6.06 Gc. As shown in Appendix I, $\mathcal{E}$ is a function of the length of the transmission line between the transmitter and the enlarged waveguide. By varying this length with a line stretcher, $\mathcal{E}$ takes on positive and negative values, and P passes through maximum and minimum points. If the maximum coupled power ($\mathcal{E}$ maximum positive) and the minimum coupled power ($\mathcal{E}$ maximum negative) are averaged, $\mathcal{E}$ is, to a large extent, canceled.

The second source of error is caused by an ambiguity of 3 db in the value of the calibration constant C_p. If the system is calibrated with m,0 and 0,n modes and is then used to measure power which is propagating wholly in m,n type modes ($m,n \neq 0$), the indicated power will be 3 db higher than the true power. There are two ways to minimize this error. The first is to adjust the calibration constant C_p so that the maximum error is ± 1.5 db. The second is to display the electric-field pattern sampled by the probes on an oscilloscope. If the broad- and narrow-wall field amplitudes are approximately equal, and if this relationship is constant as the line stretcher length is adjusted, the power flow is predominantly in m,n type modes ($m,n \neq 0$). When this situation occurs, 3 db can be subtracted from the indicated power to yield the actual power flow in the waveguide (assuming that the system has been calibrated with m,0 and 0,n modes). However, it should be mentioned that experience with low-power coaxial-to-waveguide transitions and the limited measured data on an S-gand magnetron have shown that this is not an important source of error. More data is needed to verify this conclusion in all practical cases.

2. TROMBONE LINE STRETCHER

The trombone line stretcher has the internal dimensions of standard S-band waveguide (Figure 2). When the error producing modes are present in the waveguide, the error term ε in equation 1 can take on maximum positive and negative values by adjusting the line stretcher length properly.

The 90-degree bends are standard S-band H-plane bends with inside radii of 6 inches. The sliding electrical contact is made by solid spring stock with additional thickness at the point where sliding contact occurs. Although the line stretcher was tested at 3.1 megawatts, no breakdown occurred. The trombone line stretcher was constructed with sliding teflon pressure seals because the power-measuring equipment must operate in pressurized waveguide systems. The leakage rate, measured while the line length was changing, was 0.16 cfm at an internal pressure of 1 atmosphere (gage).

The line stretcher is driven by an electric motor that can stop and reverse with less than 5 degrees overrun at the motor--that is, less than 0.006 inch overrun in path length through the line stretcher. This capability simplifies setting the line stretcher to obtain the maximum and minimum coupled power in the procedure to minimize the effect of the error terms. The rate of change of path length through the line stretcher is 14.4 inches per minute. This relatively slow speed also simplifies setting the line stretcher.

For the initial testing of the fixed-probe method, a linear line stretcher was fabricated. In the final equipment, however, a trombone line stretcher was required to eliminate the relative movement between the transmitter under test and the measuring equipment. The bends required in a trombone line stretcher inevitably cause mode conversion, and, to test the effect on the power-measuring accuracy of the 6-inch radius bends, three types of tests were made.

The first test measured the dominant mode SWR of the line stretcher at 4.0 Gc. The measured SWR was 1.15, corresponding to a reflective insertion loss of 0.02 db.

The second test compared the probe constants (C_p) obtained with the straight line stretcher with those obtained with the trombone line stretcher. The results of this test are shown in Table I.

TABLE I

COMPARISON OF PROBE CONSTANTS OBTAINED WITH TROMBONE AND STRAIGHT LINE STRETCHERS

Frequency (Gc)	Trombone Line Stretcher	Straight Line Stretcher
3.0	45.5 db	46.4 db
4.0	43.8 db	44.1 db
7.7	42.8 db	43.1 db
8.2	40.7 db	40.5 db

It can be seen from this data that the error introduced by the trombone line stretcher is less than 1 db.

In the third test, a predominantly TE_{10} field pattern was launched in the S-band waveguide and transmitted through the straight line stretcher. The relative electric-field amplitudes coupled by the top-and bottom-wall probes were then measured. This test was repeated after the straight line stretcher had been replaced by the trombone line stretcher. The results of these tests are shown graphically in Figure 3. The greater irregularity of the field plots taken with the trombone line stretcher installed show that more mode conversion does take place with this line stretcher than with the straight line stretcher. The presence of some additional modes was also indicated by the dependence on the line length of the average of the power coupled by the probes. It is significant that,

using the error-term averaging technique, the constants in the third column in Table I agree within 1 db with the corresponding constants in the second column.

3. TAPER

The taper transforms the fields from the standard size waveguide (S-band) to the enlarged waveguide with very little reflection and mode conversion.

Because the description of the field in the nonuniform (tapered) waveguide is basically different from that in a uniform waveguide, the generation of some higher-order rectangular modes is unavoidable. However, for gradual tapers, the fields in the nonuniform region differ only slightly from those in the uniform rectangular guide so that mode conversion is low.

When the accuracy of the system is considered, mode conversion near the large end of the taper is more detrimental than that occurring at the small end. This is because propagating modes generated near the small end have their cut-off frequencies reduced by nearly the same factor as the cut-off frequencies of the modes present in the standard-size guide. However, propagating modes generated near the large end of the taper may be near their cut-off frequencies in the large guide and, thus, will have a more serious effect on the accuracy of the system (Appendix III).

In terms of a mode-conversion distribution function, it is desirable to weight the function so that it favors low-mode conversion near the larger end of the taper.

During the course of this program, four tapers were fabricated--three linear tapers 7.1, 20, and 36 inches long, and a nonlinear taper 36 inches long. All the tapers have

transverse dimensions of 5.81 by 8.52 inches at the large end to mate with the fixed-probe section. The contour of the nonlinear taper was designed so that the rate of change of the phase constant is zero at both ends of the taper (reference 4 and Figure 4). The maximum rate of change of the transverse dimensions occurs at a distance one-third of the total length (12 inches) from the small end.

The tapers were evaluated by launching a TE_{10} mode at 3.8 Gc in the small end and measuring the relative field strengths at the fixed-probe locations in the enlarged waveguide. By comparing the measured field strengths with those computed for a TE_{10} mode, the effectiveness of the tapers could be estimated. The enlarged guide was terminated in a matched load. The results of these measurements are shown in Figure 5. It can be seen that the nonlinear taper transforms the TE_{10} mode from the S-band guide to the enlarged guide with the least amount of distortion.

The nonlinear taper fabricated for the final equipment has small end dimensions of 2.98 by 1.48 inches to mate with the output of the trombone line stretcher. The walls of the taper were reinforced with angle iron to prevent bulging of the taper walls when the power-measuring equipment is pressurized.

4. FIXED-PROBE SECTION

The fixed-probe section consists of an enlarged section of waveguide with internal transverse dimensions of 5.81 by 8.52 inches. Mounted on this enlarged waveguide are two sets of short electric probes; each set contains 36 probes.

The inner transverse dimensions of the enlarged waveguide were chosen on the basis of two criteria. The first criterion was that the phase constant of all modes in the enlarged guide should be sufficiently close to the free-space

phase constant so that the error caused by this condition would be less than 0.25 db. Taking the worst case, a mode at cut-off in the S-band guide, equation III-11 in Appendix III, requires that the cut-off frequency be reduced by a factor of 3. Hence, the transverse dimensions of the enlarged guide must be at least three times those of the S-band guide. The second criterion that was applied to the choice of the transverse dimensions was that the wave impedance of the enlarged guide should be equal to the wave impedance of the TE_{10} mode in S-band waveguide at the center of S-band.

The application of these criteria resulted in a wide dimension of 8.52 inches (three times the width of S-band guide) and a narrow dimension of 5.81 inches (4.34 times the height of S-band guide).

The choice of the length of the insertion of the probes is a compromise between two factors: small insertion to minimize field perturbations and large insertion to increase the sensitivity of the system and permit measurement of low power levels. The insertion length of the probes in the final equipment is 0.135 inches, giving a decoupling that varies from 51.1 db at 4.3 Gc to 45.2 db at 9.755 Gc. The increase in coupling with frequency is caused by the increase in the electrical length of the probes as the frequency is increased. System sensitivity is discussed in more detail in Section G.

The diameter of all the probes is 0.105 inches with a full radius at the tips to increase the breakdown voltage. The fixed-probe section was tested at peak power levels up to 3.1 megawatts with no indication of breakdown. A typical probe, which is somewhat shorter than the probes used in the final equipment, is shown in Figure 6.

To simplify the bandwidth requirement of the probe sampling commutators, two sets of probes are used--one, from 3 to 4 Gc and the other, from 4 to 10 Gc.

5. MULTIMODE HIGH-POWER LOAD

A high-power load, which is a good match for all possible modes, is required to terminate the fixed-probe section. A mismatched termination causes a partial standing wave in the enlarged waveguide. Depending on the phase length between the mismatch and the probes, the indicated power can be greater or less than the true power.

The shape of the load is a hollow pyramid with the base toward the transmitter. The material is an epoxy-iron mixture with the proportion: 5 parts of iron to 1 part of epoxy. The load waveguide has the same transverse dimensions as the fixed-probe section waveguide. The length of the load is 36 inches.

With the hollow-based pyramid configuration, the part of the load nearest the transmitter is in contact with the walls of the waveguide. This is ideal for heat transfer because this portion of the load dissipates the greatest amount of power.

Dominant mode SWR tests of the load were made by terminating the large end of the nonlinear taper with the load, connecting a slotted line to the S-band end of the taper, and sliding the load. In the 2.7 to 4.0 Gc range, the maximum SWR of the load is 1.008. At 9.755 Gc, an estimate of the load SWR was obtained by measuring the average of the power coupled by the probes with the load at several different distances from the probes. The ratio of the maximum average to the minimum average was 0.2 db--a direct measure of the error which could occur in an actual power measurement. An S-band high-power doorknob was used as the launching structure to provide a multimode field. The maximum-to-minimum ratio of

0.2 db corresponds to an apparent SWR of 1.02. Although the true SWR for a particular mode could be higher than 1.02, this value, obtained at 9.755 Gc, and the low SWR obtained between 2.7 and 4.0 Gc indicate that the load is a good multimode absorber.

The temperature rise of the load without cooling fins, measured at an incident power level of 117 watts (average), was 27°F (maximum). The maximum temperature capability of the eqoxy-iron mixture is 500 to 600°F.

Cooling fins and a supporting framework have been added to the waveguide that contains the load. Without forced-air cooling, the fins (totaling 4600 square inches of surface) can dissipate 3 kw at 176°F (reference 5). By operating the load at 276°F, dissipation can be increased to an average power of 5.4 kw. The dissipation can be increased to 10 kw by cooling with a forced air flow of about 1000 cfm (reference 6).

6. PROBE-SAMPLING COMMUTATORS

To make the fixed-probe power-measuring equipment capable of furnishing power-spectrum data rapidly and conveniently, automatic and continuous probe-power sampling and averaging circuits have been incorporated in the final equipment. The theoretical considerations involved in automatic probe-power sampling are analyzed in Appendix IV.

Two commutators have been fabricated--one covers the range from 3 to 4 Gc and the other, from 4 to 10 Gc. A typical commutator is shown in Figure 7. Each of the 36 stators is connected to a probe on the fixed-probe waveguide. The rotor is a choked noncontacting type and is motor driven so that the power coupled by each of the 36 probes is continuously sampled.

Transmission through a typical segment of the 3 to 4 Gc commutator as a function of the rotor angle in relation to that segment is shown in Figure 8. At 5 degrees, the rotor is midway between two stators, and it is at this point that adjacent transmission curves overlap. The lowest crossover occurs at 3.5 Gc, where the transmission is down 12.8 db. This is more than adequate because the averaging amplifier is designed to respond only to the highest amplitude pulse that occurs during the time that the rotor sweeps past a stator.

The rotation speed of the rotor is 29.5 rpm. At this speed, at least five transmitter pulses will occur in the time that it takes the rotor to move from the +5 degree crossover to the -5 degree crossover at a PRF of 100 pps.

In deriving the average of the power coupled by the probes (Appendix I), the powers coupled by the broad-wall probes and the powers coupled by the narrow-wall probes were averaged separately. In the initial testing, the probe power was sampled manually, and the separate averaging presented no problem. However, in the automatic averaging, the separate averaging complicated the instrumentation. This problem could have been eliminated entirely by redesigning the fixed-probe section to have equal numbers of broad- and narrow-wall probes. However, an analysis of the error caused by averaging all probes together was made, and it was found that the maximum error likely to occur was ± 0.37 db (Appendix V). The original design of the fixed-probe section with 22 broad-wall probes and 14 narrow-wall probes has, therefore, been retained in the final equipment. The mounting of the two commutators and the magnetic trigger generator in the probe-sampling unit is shown in Figure 9.

7. RECEIVER

The required sensitivity of the detector used to detect the RF field coupled by the probes is governed by the

power levels that the equipment must measure. Since the equipment developed on this program was required to detect very low-level spurious emissions, a microwave superheterodyne receiver was required.

Several commercial microwave field-intensity receivers were evaluated. As a result of this evaluation, an Empire Devices Model NF-112 receiver was purchased.

The noise figure for the NF-112 is 22 db in the 3 to 10 Gc range. This is a high noise figure when compared with noise figures of less than 10 db, which are easily attainable in a fixed-tuned receiver. The higher noise figure of the tunable field-intensity receivers is probably caused by tracking errors between the elements of the preselector and between the preselector and the local oscillator and by the very high IF that is used.

The high receiver noise figure raises the lower limit of the spurious power that can be measured with a given amount of probe decoupling. The relationship between the upper limit of the power-measurement error and the noise-figure bandwidth product of the detector is derived in Appendix VI. Figure 10 is a plot of the upper limit of the measurement error versus the power level calculated for a 22-db noise figure, receiver bandwidths of 1 and 5 Mc, and a probe decoupling of 40 db.

A decrease in the upper-limit error for a given power level, or a decrease in the power level for a given error, can be accomplished by (1) decreasing the receiver bandwidth, (2) increasing the probe-coupling, or (3) decreasing the receiver noise figure.

Decreasing the receiver bandwidth can introduce two sources of error--one caused by the frequency instability of the spurious emission and the other by the amount of sideband power for narrow pulses. The frequency instability problem is magnified because commercial microwave receivers do not have

an effective AFC circuit for pulsed signals. Greatly increasing the probe coupling has the disadvantage of field perturbation and decreased power-handling capability. However, the coupling can probably be increased to 30 db without incurring any difficulty.

The best solution is to decrease the overall noise figure of the receiver. Table II shows the improvement in minimum-power detection level that can be obtained by using a state-of-the-art parametric amplifier as a preamplifier and placing it ahead of a 22-db noise-figure receiver.

TABLE II

MINIMUM POWER DETECTION LEVELS USING A PARAMETRIC AMPLIFIER AS A PREAMPLIFIER

Frequency Range (Gc)	Parametric Gain (db)	Amplifier Noise Figure (db)	Improvement in Receiver Sensitivity (db)
2 to 4	20	3.0	18.4
4 to 7	20	4.5	15.5
7 to 10	20	5.5	14.8

8. AVERAGING AMPLIFIER

The averaging amplifier takes the video pulses from the receiver, which is a linear voltage detector, and produces an output current that is proportional to the average of the peak power coupled by the 36 waveguide probes. The circuit is a modification of the boxcar detector described in reference 7. Figure 11 is a block diagram of the circuit.

The output of the receiver is a continuous train of video pulses whose widths are approximately the same as those of the transmitted pulses. Because the commutator rotor

sequentially samples the voltage coupled by each probe, the amplitudes of the video pulses from the receiver will be proportional to the voltage coupled by each probe and amplitude-modulated by the transfer function of the commutator.

The input circuit of the averaging amplifier is a voltage-squaring circuit whose output is proportional to the square of the input voltage and, therefore, to the power coupled by the probes.

The squared video pulses from the squaring amplifier are shown as a function of the commutator rotation angle in Figure 12 (a TE_{10} mode has been assumed).

The solid vertical lines represent the pulses. The envelope (dashed lines) of each set of pulses is directly proportional to the transfer function of one commutator segment. Since the transfer function is unity when the rotor and stator are aligned (assuming an ideal commutator), the voltage of the video pulse at the peak of each envelope is directly proportional to the power coupled by the probe connected to that segment of the commutator. The envelope of the peaks, therefore, is directly proportional to the square of the electric field along the waveguide walls.

Following the squaring amplifier, the pulses are amplified by a three-stage video amplifier (Figure 11). This amplifier provides 29 db of gain to overcome voltage drops that occur in the peak-reading and charge-transfer circuits and to provide a conveniently measurable output current.

A capacitor in the peak-reading circuit charges to the highest pulse voltage that occurs during a commutator-segment sampling interval (56.5 msec). At each 10-degree commutator crossover point (Figure 12), a pulse, from a magnetic pulse generator synchronized with the commutator, triggers the charge-transfer circuit and transfers the peak voltage from the peak-reading circuit to the charge-storage circuit.

The resulting voltage across the charge-storage capacitor is shown in Figure 13. A jack for observing the sampled waveform on an oscilloscope has been provided on the front panel of the averaging amplifier. This waveform can be considered to be composed of a series of rectangles with equal base widths and with heights directly proportional to the power coupled by the associated probe. If the waveform of Figure 13 is represented by a Fourier series, the DC term is given by:

$$V_{average} = \frac{A}{W}$$

where

A = area under the curve,
W = base of the curve.

Using the rectangle interpretation of Figure 12,

$$V_{average} = \frac{\sum_{n=1}^{N} V_n \Delta\theta}{N\Delta\theta} = \frac{1}{N} \sum_{n=1}^{N} V_n \qquad (2)$$

where

N = 36.

Since the V_n are proportional to the peak power coupled by the probes, $V_{average}$ is proportional to the average of the peak power coupled by the probes.

The next to last circuit in the averaging amplifier is a cathode follower that has a load impedance with a very

long time constant (Figure 11). Because of this time constant, the cathode follower responds only to the DC term in the Fourier series representation of the output from the charge-storage circuit.

The long time-constant load impedance is DC coupled to the output cathode follower, which drives the current readout meter. The output current is, therefore, proportional to the average voltage given by equation 2, which, in turn, is proportional to the average of the peak power coupled by the probes. Two time constants, long and short, selected by a front panel switch have been provided. The short time constant is convenient when adjusting the line stretcher. The long time constant is used when making a power measurement.

The averaging amplifier chassis is shown in Figure 14.

9. PACKAGING

To facilitate transportation, setup, and operation, the final equipment was divided into three major units: (1) trombone line stretcher, (2) fixed-probe section, multimode load, and probe-sampling unit, and (3) instrumentation.

Units 1 and 2 are mounted on separate carts. When the equipment is assembled for operation, the taper is connected between the carts. Both carts have provisions for adjusting the heights of the waveguide components to facilitate flange alignment. The assembled waveguide components are shown in Figure 15.

The pulse instrumentation, consisting of the receiver, averaging amplifier, and power supplies, and the control panel, consisting of the line stretcher controls, readout meter, and main power switch, are mounted in a standard 19-inch relay rack. A drawer for cables has also been included. Figure 16 shows the control panel. The complete relay rack is shown in Figure 17.

10. EXPERIMENTAL RESULTS

Extensive experimental testing of the fixed-probe equipment was performed in the 3 to 10 Gc frequency range. A variety of launching structures was used to test the equipment with both simple and complex modal configurations. Typical examples of the tests performed follow.

a. TE_{10} Mode

A TE_{10} mode was launched in the S-band waveguide at 4.3 Gc using a conventional coaxial-to-waveguide adapter. The power, P, in the waveguide was computed with a correction for the reflection loss at the adapter. The power coupled by the probes was averaged to obtain P_p, and a calibration constant was determined from:

$$C_p = \frac{P}{P_p}$$

The measured electric-field amplitudes at the top-wall and bottom-wall probes are shown in Figure 18. The top-wall and bottom-wall fields differ because of the presence of some higher-order modes. These were generated by either the load or the taper. (This data was taken early in the program using a linear taper and an Eccosorb load.) The side-wall electric-field maximum was 26 db below the top-wall maximum. Appendix VII shows that a side-wall maximum which is small in relation to the top-wall maximum can cause the top-wall and bottom-wall fields to differ appreciably.

The TE_{10} calibration constant, C_{p10}, was computed from the data and found to be 14.6×10^4 (51.6 db).

Changing the length of the S-band waveguide did not change the field configuration. This indicates that, since the S-band guide would be dispersive for any modes that could propagate at 4.3 Gc, a small amount of higher-order mode power was generated in the enlarged waveguide.

b. TE_{20} Mode

A TE_{20} mode was launched in the S-band waveguide at 4.3 Gc using a waveguide mode launcher. This consisted of a section of S-band waveguide with two probes projecting into the guide from opposite broad walls (Figure 19). The probes carried equal-amplitude and equal-phase signals and were placed at positions corresponding to TE_{20} maxima in the S-band waveguide. The measured data is shown in Figure 20. Distortion is caused by a small side-wall contribution as discussed in Appendix VII.

The TE_{20} calibration constant, C_{p20}, was found to be 18.1×10^4 (52.6 db). Changing the line length of the S-band waveguide resulted in a peak-to-peak variation in the constant of 0.2 db.

c. Simultaneous TE_{10} and TE_{20} Modes

TE_{10} and TE_{20} modes were launched simultaneously at 4.3 Gc using the mode launcher and measurements were made with several different lengths of S-band waveguide. P and P_p were measured for each dispersive length of S-band guide.

The measured plots are shown in Figure 21. It should be noted that the field pattern changes as dispersive sections of guide are added. This is to be expected because there are at least two propagating modes in the S-band guide. The calculated calibration constants are as listed in Table III.

TABLE III

LENGTH OF DISPERSIVE SECTION VERSUS CALIBRATION CONSTANT (C_{p10} and C_{p20})

Length of Dispersive Section (inches)	Calibration Constant ($C_{p10,\ 20}$)
16	19.0×10^4
18	20.3×10^4
20	15.7×10^4

This is a peak-to-peak variation of 1.1 db.

Summarizing all the measurements at 4.3 Gc, the variation in the probe constant for three types of propagating modes--TE_{10}, TE_{20}, and mixed TE_{10} and TE_{20}--is ± 0.7 db. This indicates that the probe constant is independent of the particular modal power distribution at 4.3 Gc. Up to 4.41 Gc, only the TE_{10} and TE_{20} modes can propagate in S-band waveguide.

d. Multimode Propagation

The variation of C_p was investigated with multimode propagation. A frequency of 7.0 Gc was chosen. At this frequency, propagation in the following modes is possible: TE_{10}, TE_{20}, TE_{01}, TE_{11}, TM_{11}, TE_{21}, TM_{21}, and TE_{30}. A center-fed electric-probe coaxial-to-waveguide transition was used as the launching structure and the electric field was plotted for several dispersive lengths of S-band guide. The field plots are shown in Figure 22. Since several modes are propagating, the field pattern changes as the S-band guide length is changed. The calibration constants are shown in Table I..

TABLE IV

LENGTH OF DISPERSIVE GUIDE VERSUS CALIBRATION CONSTANT

Length of Dispersive Guide (inches)	Calibration Constant
16	4.56×10^4
17	5.95×10^4
18	6.00×10^4
19	4.22×10^4
21	5.98×10^4
22	6.50×10^4

Despite the large variation in the field configuration with dispersion, the maximum variation in the probe constant is less than ± 1 db.

Although the frequency is high enough to permit the propagation of the E_{01x} E_{21x} error term (equation I-16 in Appendix I), the small variation in the probe constant indicates that its amplitude is negligible.

The sources of error in this data are variations in the probe couplings and mode conversion by the taper and load. In the fixed-probe section developed for the final equipment, the coupling of the individual probes was carefully adjusted to ± 0.1 db.

e. Tests at 9.755 Gc

The initial calibration at 9.755 Gc was obtained with a single electric-probe launching structure. The probe was located in the center of the broad wall of the S-band waveguide.

To improve the precision of the calibration, only relative power measurements were made. The equation governing this method of calibration can be obtained by solving

equation I-15 (Appendix I) for the ratio of true power in the waveguide to the average of the power coupled by the probes. The result is:

$$\frac{P}{P_p} = C_p - \frac{\mathcal{E}}{P_p}$$

The error terms, $\mathcal{E}$, are a function of the length of the line stretcher.

For each length of the line stretcher, the quantity P/P_p was measured, and the data was plotted (Figure 23A). The dependence of P/P_p on the length of the line stretcher shows that error terms are present.

Averaging the absolute maximum and minimum values over the interval of measurements yields a calibration constant of 0.573×10^5. Hence, at the calibration frequency of 9.755 Gc, the power in the waveguide, P, is given by:

$$P = (0.573 \times 10^5)\ P_p$$

or

$$P = P_p + 47.6 \text{ dbm}$$

where P_p is expressed in dbm.

To check the accuracy of the system under conditions simulating an actual transmitter, a conventional high-power S-band doorknob coaxial-to-waveguide transition was used as the launching structure and the calibration procedure was repeated. The resulting data is shown in Figure 23B.

The period of the error term caused by the simultaneous presence of the TE_{11} and TE_{31} modes is 12.4 cm at 9.755 Gc. The data shows that this error term is predominant. However, the fine structure in the plotted curve indicates the

presence of additional error terms at lower amplitudes. The fact that modes with odd indices predominate is consistent with the symmetry of the doorknob launching structure.

Averaging the absolute maximum and minimum yields a constant of 0.540×10^5 or 47.3 db.

This result indicates that, using the initial calibration constant, the power measured at 9.755 Gc with the doorknob transition would be higher than the true power by 0.3 db. This result is particularly significant since the doorknob launcher produces mode patterns which closely simulate the higher-order modes that would be encountered in measuring the spurious emission of an actual transmitter. The way in which these measurements were made, using relative power, and the care which was used, all sources of experimental error greater than 0.2 db were eliminated, make this measurement indicative of the ultimate accuracy attainable with the fixed-probe equipment under carefully controlled conditions.

11. CALIBRATION

The final fixed-probe equipment was calibrated in two stages--first, the averaging amplifier and receiver, and second, the combination of probe coupling, commutator insertion loss, and cable insertion loss.

The averaging amplifier and the receiver were calibrated by supplying a pulsed signal from a calibrated signal generator to the input of the receiver. The detected video pulses from the receiver were connected to the input of the averaging amplifier. The input signal levels were high enough to ensure at least a 20-db signal-to-noise ratio for the lowest amplitude calibrating signal.

For constant amplitude pulses, the average peak signal amplitude is equal to the peak signal amplitude. Pulsed signals of known peak amplitude can be obtained from standard calibrated signal generators.

Since the average of the peak signal amplitude is equal to the peak signal amplitude in this setup, the proportionality between the current output of the averaging amplifier and the average peak input signal can be obtained. The data that was taken was the RF output amplitude of the generator versus the output current of the averaging amplifier. This calibration curve is shown in Figure 24. The constant 20-db attenuation has been subtracted to adjust the calibration for the maximum sensitivity range of the receiver (0-db input attenuation).

In an actual power measurement, the current indicated on the readout meter is noted, and, using the calibration curve of Figure 24, the corresponding input power is obtained. Any attenuation present at the input of the receiver is added and the sum is the average of the power coupled by the probes. This calibration is not frequency-sensitive because the sensitivity of the receiver is standarized at any frequency by the internal impulse calibration.

The combination of probe coupling, commutator insertion loss, and cable loss was calibrated by feeding a known amount of power into the S-band guide through a standard coaxial-to-waveguide transition. Dominant mode transitions were used at frequencies above 4 Gc, and short linear tapers were used to transform from the transition to the S-band input guide of the fixed-probe equipment.

Dominant mode transitions were used to avoid the generation of error terms and thereby simplify the calibration procedure. The resulting calibration curve is shown in Figure 25.

The frequency sensitivity of the curves is due primarily to the high SWR "seen" looking into the coaxial side of the probes interacting with mismatches "seen" looking into the commutator. This is particularly evident in the 3 to 4 Gc

band where the insertion loss of the probe cables is low. At the higher frequencies, the insertion loss of the probe cables provides isolation between the probes and the commutator and the variation in the curves is due only to the natural frequency sensitivity of the probe coupling and the variation with frequency of the commutator insertion loss.

In the 3 to 4 Gc band, calibration points were taken at 50-Mc intervals. From 4 to 10 Gc, the calibration points were taken at 200-Mc intervals. These calibration intervals were arrived at by calibrating at successively smaller increments until intermediate spot-checked frequencies showed good agreement with the curves.

12. MULTIMODE POWER FLOW WITH MISMATCHED TERMINATIONS

The fixed-probe equipment developed on the present contract measures the spurious-emission power transferred into a matched load. This is useful for testing transmitting systems with standardized load conditions and for the determination of their emission spectra as a function of controlled mismatches inserted between the transmitter and a matched load. For this type of measurement the power measuring equipment would be inserted between the mismatch and the matched load.

In an operational system, however, consideration must be given to the fact that the antenna is a mismatched load impedance outside the intended range of operation. This section describes modifications to the fixed-probe method that will make it capable of measuring the spurious-emission power transferred to an arbitrary multimode mismatched termination. Three methods of measurement are considered: the first two are exact; the third is an approximate method.

a. EXACT METHODS

The fixed-probe equipment can be adapted to measure the spurious-emission power absorbed by a mismatched load by varying the phase of the reflected wave at the plane of the measuring probes. It is shown in Appendix VIII that, by varying this phase, the power coupled by the fixed probes is equal to a constant plus a sinusoidally varying function of the phase length. By taking the arithmetic average of the indicated power for a half-wavelength phase variation, an equivalent power P_a is obtained:

$$P_a = P_M + P_R \tag{3}$$

where

P_M = power that would be absorbed by a matched load

P_R = total reflected power from the multimode mismatched termination

The power absorbed by a mismatched load P_T is given by

$$P_T = P_M - P_R \tag{4}$$

Eliminating P_R from equations 3 and 4 gives

$$P_T = 2P_M - P_a \tag{5}$$

The right side of equation 5 consists of two measureable quantities and, therefore, the power P_T absorbed by the mismatched load can be determined. In the actual measurement procedure, the necessary phase variation of the reflected wave required to determine P_a can be obtained by measuring

the power coupled by three sets of probes located at three different cross sections along the axis of the oversize waveguide. This measurement is made with the normal system termination in place. The power P_M is measured with the multimode matched loading terminating the system. The power P_T absorbed by the antenna can then be computed with equation 5. Figure 26 is a diagram of the equipment.

A more direct approach to the problem of measuring the power absorbed by a mismatch is to use directional coupling rather than the non-directional probes used in the present equipment. Directional coupling can be done with pairs of holes or pairs of probes. Using this technique the incident and reflected powers are measured directly and the transmitted power is simply the difference between the two. This approach has the advantage that the normal system termination (antenna) is never removed and continuous monitoring is, therefore, possible.

b. APPROXIMATE METHOD

The approximate method eliminates the need for making measurements with a matched load as required by the first exact method. Instead of computing the average power from the three sets of probes, the geometric mean P_g of the maximum and minimum is computed.* The value of P_g given by

$$P_g = \sqrt{P_{max} P_{min}} \qquad (6)$$

---

* This was suggested by S. Cohn of ECAC.

is approximately equal to the power absorbed by the mismatched load. For SWR's of 3 and 10, the error would be 1 and 6 db, respectively. This degree of accuracy may be acceptable for many applications.

The equipment for the approximate-measurement method is identical with that required for the first exact measurement method with the exception of a multimode matched load. Both methods require making power measurements for different phases of the load-multimode reflection coefficients.

Instead of using three sets of probes and additional commutators to obtain the reflection phase variation, an additional line stretcher could be used either in the oversize waveguide or in the standard-size output waveguide.

C. MOVABLE-PROBE METHOD

The movable-probe method measures multimode power flow by directly integrating the square of the electric field amplitude over a plane transverse to the direction of propagation in an enlarged section of waveguide. Measurements of the electric field amplitude are made with a movable probe.

This section describes the theory of operation, the equipment developed, and the experimental results obtained with the movable-probe equipment.

1. THEORY OF OPERATION

a. General

The movable-probe method, measuring power inside a waveguide by directly integrating the electric field-strength measurements, uses a movable probe in a raster-type scan. It has an advantage over fixed-probe waveguide methods in that error terms are not present in the integrated power. The probes must be made small, however, to avoid generating spurious modes. The method described on the following pages is for rectangular waveguide; it can be adapted for coaxial line.

b. Basic Principle

The movable-probe method is based on the expression for the incident-power flow in a rectangular waveguide. Appendix III derives this expression by integrating the Poynting vector.

Generally, the phase and magnitude of the quantities E_x, E_y, $\frac{\partial E_x}{\partial z}$, $\frac{\partial E_y}{\partial z}$, $\frac{\partial E_z}{\partial x}$, and $\frac{\partial E_z}{\partial y}$ must be measured over the entire x-y plane to obtain the data for performing the desired

integration. The operation is quite complex and is not considered to be within the scope of this investigation because it necessitates the use of a computer.

A considerable reduction in complexity can be achieved by taking the measurements in a waveguide with an enlarged cross section that is inserted in the transmission line (Figure 27A). The enlarged waveguide is about three times as wide and three times as high as the transmission-line waveguide to which it is connected by tapered transition sections. The taper of the transition sections is very gradual to avoid generating additional modes.

The effect of the enlarged waveguide is to make the z-axis propagation constant independent of mode (TE or TM of any index); the propagation constant approaches that of free space. This permits the substitution of

$$-j\omega\sqrt{\mu\epsilon}$$

where

ω = radian frequency
μ = permeability of dielectric within the waveguide
ϵ = permittivity of dielectric within the waveguide
for the derivative operator $\frac{\partial}{\partial z}$.

The enlarged waveguide markedly reduces the values of $\frac{\partial E_z}{\partial x}$ and $\frac{\partial E_z}{\partial y}$ to the point where they can be neglected.

These simplifications result in an expression, derived in Appendix III, for power flow that is approximately

$$P = \frac{1}{\eta}\int_0^b \int_0^a \left(|E_x|^2 + |E_y|^2 \right) dx\, dy \qquad (3)$$

In Appendix III, it is shown that the maximum error is 6 percent.

Equation 3 forms the basis of the movable-probe method. By using sampling probes whose output is proportional to the electric field strength, it is possible to determine P by having two probes, one sampling E_x and the other, E_y (Figure 27B). Each probe is moved in a raster-scan--that is, it scans the x-axis at discrete vertical levels. Scanning at about ten levels should be adequate to integrate the fields accurately. This method is similar to that for determining spurious power from free-space field measurements, but it is accomplished in a fully shielded waveguide.

2. TAPER

The requirements for a tapered waveguide transition section between the standard-size guide and the oversize guide are identical with those of the fixed-probe method.

Three lengths of linear tapers, 7.1, 20, and 36 inches and a 36-inch nonlinear taper were used during this phase of the program.

3. ENLARGED WAVEGUIDE SECTION

The design considerations for the enlarged waveguide section are the same as for the fixed-probe method.

An additional requirement of the enlarged guide used with the movable-probe method is that the top broad-wall and one narrow-wall must be slotted and machined to permit the insertion of E_x and E_y probes and to provide bearing surfaces for the probe carriages.

4. PROBE AND CARRIAGE ASSEMBLIES

Each of the two probes samples a component of the transverse electric field in the enlarged waveguide. The probes are identical except for the length of their 1/8-inch-diameter coaxial cables (Figures 28A and 28B); the coaxial cable

of the probe that is to be inserted through the narrow wall of the enlarged waveguide is 1-3/8 inches longer than that of the other probe. (Both probes must be able to reach halfway into the waveguide, and the distance from the narrow wall to the waveguide center is greater than the distance from the wide wall.)

Although both probes are capable of insertion only halfway into the guide, it is possible to probe the full cross-section by rotating the enlarged waveguide section 180 degrees around its longitudinal axis. By limiting the probe insertion to 50 percent, the voltage breakdown problem is greatly alleviated.

Two basic types of probes were tested--unbalanced and balanced. The first unbalanced probe tested was simply a piece of rigid coaxial line with the center conductor extending a short distance beyond the shield.

The coupling of this probe was found to be strongly dependent on the length of the outer conductor within the waveguide. An artificial ground plane was added to this probe to reduce the effect of currents induced on the outer surface of the coaxial shield (Figure 28A). Although this was an improvement over the first probe, it was not entirely satisfactory.

The first balanced dipole probe, shown in Figure 29, was designed in accordance with the principles outlined in reference 8. The TE_{10} mode was launched in the S-band waveguide and electric-field measurements were made in the enlarged guide using this probe. The experimental curve is compared with the theoretical curve for one-half of the guide in Figure 30.

It can be seen that the measured points lie below the theoretical points. On the basis of this result and

because the slots in this type of probe made it impossible to make field measurements closer than one inch from the guide wall through which the probe was inserted, a second balanced dipole was constructed.

The second balanced dipole probe (Figure 31) has a balanced two-wire coaxial feed. For the initial testing a Stripline® hybrid was used as the balanced-to-unbalanced transformer. The TE_{10} field plot obtained with this probe is compared with the theoretical curve in Figure 32. The measured curve shows good agreement with the theoretical curve. The data was then integrated numerically to obtain the probe coupling constant from

$$K = \frac{P}{\int_0^b \int_0^a \left(|E_x|^2 + |E_y|^2 \right) dx\, dy} \qquad (4)$$

To check the ability of the probe to make an accurate power measurement with a different field configuration, a TE_{20} mode was launched.

The experimental curve and the theoretical curve are compared in Figure 33. The data was then used to obtain a second probe-coupling constant.

The second probe-coupling constant differs from the first by only 0.44 db; this indicates that the probe-coupling constant is essentially independent of the field configuration and that this probe is capable of making accurate power measurements when the field is predominantly m,0 or 0,n.

A further requirement of the probe was that it be capable of measuring the electric field of one polarization in the presence of another electric field with orthogonal polarization. Tests indicated that the directivity of the balanced dipole probe was poor. Another probe was then

constructed (Figure 34) whose supporting structure in the vicinity of the probe is in the z-direction--the direction of propagation. The advantage of this type of support is that there is no field component parallel to the supporting structure near the dipole because, in the enlarged guide, the propagating wave is nearly a plane wave. Wide-band baluns were used with these probes (Figure 34). The design method for these baluns is given in reference 9.

To test the directivity of the probes, a TE_{10} mode was launched in the S-band waveguide and the field amplitude was measured with the E_x and E_y probes. For probes with perfect directivity and an ideal TE_{10} mode, the response of the E_x probe would be zero, since this mode has no E_x component. The measured data are shown in Figure 35. If it is assumed that there is no mode conversion in the system, the difference between the E_y and the E_x plots in db is a conservative measure of the directivity. From Figure 35, it can be seen that the directivity is greater than 14 db except when the probe is less than 2 cm from the side wall. A similar test at 5.0 Gc showed that the average directivity was about 14 db.

An estimate of the effect of imperfect directivity on system accuracy can be obtained by assuming the presence of only one electric field component in the waveguide. The apparent power will be greater than the true power by the amount of power coupled by the probe that is orthogonal to the field. The error in db is then given by

$$\text{Error in db} = 10 \log \left(1 + 10^{\frac{-D}{10}}\right) \qquad (5)$$

where D is the directivity in db. With a directivity of 14 db, the maximum error is 0.14 db. With both E_x and E_y

field components present in the waveguide, the error will probably be less.

To check the overall accuracy in making a power measurement, a standard S-band electric-probe coaxial-to-waveguide transition was used as a launching structure at 5.0 Gc. The output of the E_x and E_y probes as a function of position in the enlarged waveguide cross section was obtained. The probe constant was found by numerically integrating the data. The result gave a constant, K, of 0.1369.

The above procedure was repeated with the transition cross-guided to give a different field configuration. For this case, the K obtained was 0.1358. The difference of 0.04 db between the two values of K indicates the accuracy that could be obtained in a power measurement.

The probes were tested for breakdown by connecting the enlarged waveguide directly to an S-band magnetron through a nonlinear taper. The maximum peak power available was 500 kw. At this power level, there was no indication of breakdown. Sliding the probes during the test had no effect. On the basis of the increased thickness of the z-axis dipoles, the breakdown power, without pressurization, is estimated to be about 1 megawatt.

5. MULTIMODE LOAD

The requirements for a multimode load for the movable-probe method are identical with those for the fixed-probe method and the same load can be used with both methods.

The low-power testing of the movable-probe equipment was done with a batt of Eccosorb inclined about 45 degrees toward the direction of propagation. The measured SWR of this configuration for the dominant mode was 1.05.

D. FREE-SPACE METHOD

Three methods of measuring the radiated spurious emissions of a microwave transmitter in free space were investigated. These methods were: (1) a scanning dipole probe, (2) a passive scatterer, and (3) multiple stationary probes. This section discusses the theory and the results obtained in this phase of the program.

1. THEORY

The total power radiated by an antenna can be determined by making measurements over a spherical surface enclosing the antenna. Given the power density at all points on the spherical surface, $P(\theta,\phi)$, the total radiated power is given by

$$P_T = \int_{-\frac{\pi}{2}}^{\frac{\pi}{2}} \int_{0}^{2\pi} P(\theta,\phi) \cos\theta \, d\phi \, d\theta \qquad (6)$$

Measurement of the power in this manner would require a complete pattern range and pattern recording equipment.

For certain aperture distributions, the energy radiated is contained in an area the size of the aperture for a distance of $D^2/2\lambda$, where D is the aperture dimension and λ is the free-space wavelength. Thus, it is possible to determine total power by measuring the radiated energy over the aperture area only, thereby decreasing the pattern-range requirements. It is now possible to use a probe to scan the aperture in any plane from the aperture plane ($z = o$) to $z = D^2/2\lambda$ and still obtain the total power radiated.

Preceding Page Blank

If we let the transmission line (waveguide) taper gradually to an aperture of several wavelengths, the modal distribution should remain unchanged at the aperture. If we assume a power density of $P(x,y)$ at any point (x,y) in the aperture, then

$$P_T = \iint_S P(x,y)\, dS \tag{7}$$

would give the total power radiated by the aperture. If we have an aperture of width a and height b, then

$$P_T = \int_{-\frac{b}{2}}^{\frac{b}{2}} \int_{-\frac{a}{2}}^{\frac{a}{2}} P(x,y)\, dxdy \tag{8}$$

The total absolute power can be determined by integrating over the entire aperture. Since the aperture distribution is general, a multitude of polarizations can be propagated. To obtain the total amount of power radiated in all polarizations, the power in only two orthogonal polarizations need be detected. Thus,

$$P(x,y) = P_H(x,y) + P_Y(x,y) \tag{9}$$

If a probe is used to measure the power radiated by the aperture, the probe must be calibrated to determine

the absolute power density. The power density (P_d) in the aperture is determined by

$$P_d = \frac{P_r}{A_e} \text{ or } A_e = \frac{P_r}{P_d} \tag{10}$$

where

P_r = power received by the probe,

A_e = effective area of the probe.

To determine the effective area of the probe, the received power in a field of known power density is measured. By transmitting a known power into a horn that will support only the TE_{10} mode, the absolute power-density distribution across the aperture is determined. The power density in the H-plane is given by $P_o \cos^2(\pi x/a)$ and is constant in the E-plane. Thus

$$P_T = \int_{-\frac{b}{2}}^{\frac{b}{2}} \int_{-\frac{a}{2}}^{\frac{a}{2}} P_o \cos^2 \frac{\pi x}{a} \, dxdy \tag{11}$$

Integrating,

$$P_T = \frac{abP_o}{2} \tag{12}$$

or

$$P_o = \frac{2P_T}{ab} \tag{13}$$

where

P_T = the total power transmitted,

P_o = the maximum power density at the center of the aperture ($x = o$, $y = o$).

Thus, knowing P_T, a, and b, P_o can be determined. By then measuring the power received with the probe at the center of the aperture, the effective area of the probe can be determined from

$$A_e = \frac{P_r}{P_d} = \frac{P_r}{P_o} . \tag{14}$$

The results obtained with the three types of probes are given in the following sections.

2. SCANNING DIPOLE PROBE

The electric-field measurements were made with a small dipole connected to a balanced transmission line to minimize field perturbations and the effect of unbalanced currents induced by the incident field.

Measurements were made at a single frequency with the TE_{10} mode propagating in the S-band guide. With the dipole and transmission line in a plane perpendicular to the direction of propagation, the results differed by 0.5 db from measurements made with the dipole and transmission line parallel to the direction of propagation. In both cases, the dipole was parallel to E_y. The equipment setup is shown in Figure 36. The experimentally determined power densities are shown in Figure 37.

Separate power measurements were also made at 5.5 Gc with TE_{10} and TE_{01} propagation. The difference between the measured powers was 0.2 db indicating that, using the probe constant calculated from the TE_{10} data, the power in the TE_{01} mode could be determined with an accuracy of 0.2 db.

Since it is possible to have modes with orthogonal polarizations propagating, it is necessary to measure the two components. This can be done by scanning the aperture twice

with the probe orthogonal in both cases. It may also be possible to use crossed dipoles and have two outputs, one for each polarization, and continuously monitor each or switch rapidly between them while scanning.

An important factor in the sensitivity of the scanning probe system is the degree of the coupling of the probe to the incident field. The coupling for a small matched probe depends on the effective area of the probe; this, in turn, is proportional to the square of the wavelength. Thus, the coupling will vary as a function of frequency at the rate of 6 db per frequency octave. It is possible to use a different probe for each octave, thus limiting the change to 6 db. However, to simplify the equipment, it is more desirable to operate the probe over a wider band and calibrate the coupling variation.

The coupling is lowest near the fundamental frequency where the higher powers are to be expected and increases with frequency. Thus, the sensitivity increases as the expected output power decreases. The coupling at 5.5 Gc with the present experimental probe is about -30 db.

3. ROTATING SCATTERER

A technique for measuring the field distribution in the near field of an antenna used at Ohio State University (reference 10) and in England (reference 11) was investigated. This technique consisted of scanning the aperture of a waveguide horn with a scattering element. The element used was a short thin metal rod mounted on a nylon string. The energy scattered by the scattering element was received with a waveguide horn located away from the transmitting antenna. To separate the scattered signal from the energy being radiated from the transmitting horn, the scattered signal was modulated by spinning the element at 1200 rpm. The element was

spun about an axis perpendicular to the axis of the rod and in a plane containing the vectors designating the electric field and the direction of propagation. A heterodyne receiver was used to amplify and detect the received signal. At the output of the receiver, a tuned AF amplifier was used to amplify the detected signal. The output of the AF amplifier was dependent on the power-density level at the point at which the scattering element was located. By scanning the aperture of the transmitting horn with the scattering element, the distribution of power density in the aperture was determined. The total power transmitted was then found by integrating over the aperture of the horn. To obtain absolute power, it was necessary to calibrate the receiver as a wattmeter. The main advantage of this method was that no transmission lines were required in the aperture of the transmitting horn.

When measurements were made using this approach, the distribution across the aperture was not that expected for the TE_{10} mode. Instead, rapid variations occured in the distribution. These variations were caused by the scattered field reflecting off the waveguide walls. Previous experimenters were able to minimize the effects of these reflections by using a very short scattering element and a directional coupler in the waveguide of the transmitting horn to receive the scattered signal.

For this task, the use of a directional coupler is not feasible because the power to be measured will be in waveguide capable of supporting higher-order modes. In addition, a directional coupler that responds equally to all possible modes is beyond the state of the art. Also, the energy in the different modes would depend on the location of the scattering element in the aperture. Finally, the sensitivity of this system is below that obtainable with a scanning probe.

4. MULTIPLE STATIONARY PROBES

The possibility of using a number of stationary probes rather than a single scanning probe was investigated because switching between probes can be accomplished more rapidly than scanning the probe. To deflect the energy and to furnish a termination for the transmission lines of the probes, a ground plane was placed in front of the aperture and tilted at a 45-degree angle. Dipole probes were used in the plane of the aperture with the transmission lines running parallel to each other and perpendicular to the horn aperture back to the ground plane. By sampling the energy at each of these probes and integrating over the aperture area, the output power can be obtained. The multiple-probe method introduced several problems that were not solved completely. After the energy is reflected from the ground plane, the transmission lines were orthogonal to one polarization only and, thus, affected the other polarization. Also, the coupling between probes was troublesome. If the number of probes is reduced, both problems are alleviated somewhat but the accuracy is degraded.

Another multiple-probe arrangement used vertical stubs mounted on the 45-degree ground plane. Since these probes respond to only one polarization, the electric field at the horn must be measured in two orthogonal positions. Although this eliminated the transmission-line problem, the coupling was still troublesome, and probe responses were not equal. Also, since the probes are not in a plane parallel to the aperture, it is possible to obtain erroneous information because the measurements are being made in the near field where the energy distribution changes as a function of distance from the aperture. If the aperture distribution is known, it is possible to compensate for this condition.

E. CONCLUSIONS

The fixed-probe, movable-probe, and free-space methods are capable of measuring multimode power with an accuracy of ±1 db or better. No computer services are required for data reduction.

The fixed-probe method has three important advantages. The first two advantages, inherently high power-handling ability and small field perturbation, are the result of the small amount of probe insertion and the use of oversize waveguide. The highest power available for testing was 3.1 megawatts, and, at that level, no breakdown occurred. The third advantage is that fixed probes can be readily adapted to automatic sampling techniques. The fixed-probe method has error terms in the expression for the probe coupled power; however these terms are eliminated by using a line stretcher in the standard-size guide. Although the emphasis on this program has been the measurement of power into matched loads, the fixed-probe equipment can be adapted to make measurements of spurious emission power transferred to mismatched loads.

The movable-probe method does not require a line stretcher. However, the power-handling ability of this method is less than that of the fixed-probe method because the probe must be inserted at least half way into the enlarged waveguide. The time required to make a power measurement is longer than with the fixed-probe method since the probes must scan the entire cross section of the waveguide. The movable-probe method would be useful in an application where high precision is a prime factor and speed and power-handling ability are of secondary importance.

Preceding Page Blank

The results obtained with a dipole probe scanning the radiation aperture indicate that this is the most satisfactory method for measuring spurious-emission power in free space. This method is also relatively slow because of the scanning requirement. Another disadvantage of the free-space method is the radiation hazard when making measurements on high-power transmitters.

In view of the advantages of the fixed probe method, the instrumentation required for rapid and continuous spurious-emission power measurements was developed. The probe-sampling commutators and the averaging amplifier permit the multimode spurious-emission power to be read continuously at any given frequency. With the continuous tuning receiver, complete spurious-emission spectrum measurements can be made. The time required is less than 5 minutes per frequency.

A preliminary investigation of the problem of measuring the spurious emission power radiated by a mismatched antenna indicates that the fixed probe equipment can be modified to make such measurements.

F. REFERENCES

1. M. P. Forrer and K. Tomiyasu, "Effects and Measurement of Harmonics in High Power Waveguide Systems," 1957 IRE National Convention Record, pt 1, p 263-269.
2. V. G. Price, "Measurement of Harmonic Power Generated by Microwave Transmitters," IRE Transactions on Microwave Theory and Techniques, Vol MTT-7, p 116-120, January 1959.
3. D. J. Lewis, "Mode Couplers and Multimode Measurement Techniques," IRE Transactions on Microwave Theory and Techniques, Vol MTT-7, p 110-116, January 1959.
4. C. C. H. Tang, "Optimization of Tapers Capable of Multimode Propagation," IRE Trans, Vol MTT-9, No. 5, p 442, September 1961.
5. J. P. Welsh, "Design Manual of Natural Methods of Cooling Electronic Equipment," Cornell Aeronautical Laboratory Report No. HF-845-D-18, Contract No. NObsr-63043, November 1956.
6. J. P. Welsh, "Design Manual of Methods of Forced Air Cooling Electronic Equipment," Cornell Aeronautical Laboratory Report No. HF-845-D-19, Contract No. NObsr-63043, June 1958.
7. J. L. Lawson and G. E. Uhlenbeck, "Threshold Signals," MIT Rad Lab Series, McGraw-Hill Book Co., Inc., Vol 24, New York, 1950.
8. S. Silver, "Microwave Antenna Theory and Design," MIT Rad Lab Series, McGraw-Hill Book Co., Inc., p 246-248, New York, 1949.
9. J. W. McLaughlin, D. A. Dunn, and R. W. Grow, "A Wide Band Balun," IRE Trans, Vol MTT-6, No. 3, p 314, July 1958.
10. R. Justice and V. H. Rumsey, "Measurements of Electrical Field Distribution," IRE Trans, Vol AP-3, p 177.
11. A. L. Cullen and J. C. Parr, "A New Perturbation Method for Measuring Microwave Fields in Free Space," Proc IEE, Vol 102, pt B, p 836, No. 6, November 1955.
12. V. G. Price, J. P. Rooney, and C. Milazzo, "Final Report Phase I--Measurement and Control of Harmonic and Spurious Microwave Energy," Report TIS R58ELM112, Contract AF 30(602)-1670, 8 July 1958.

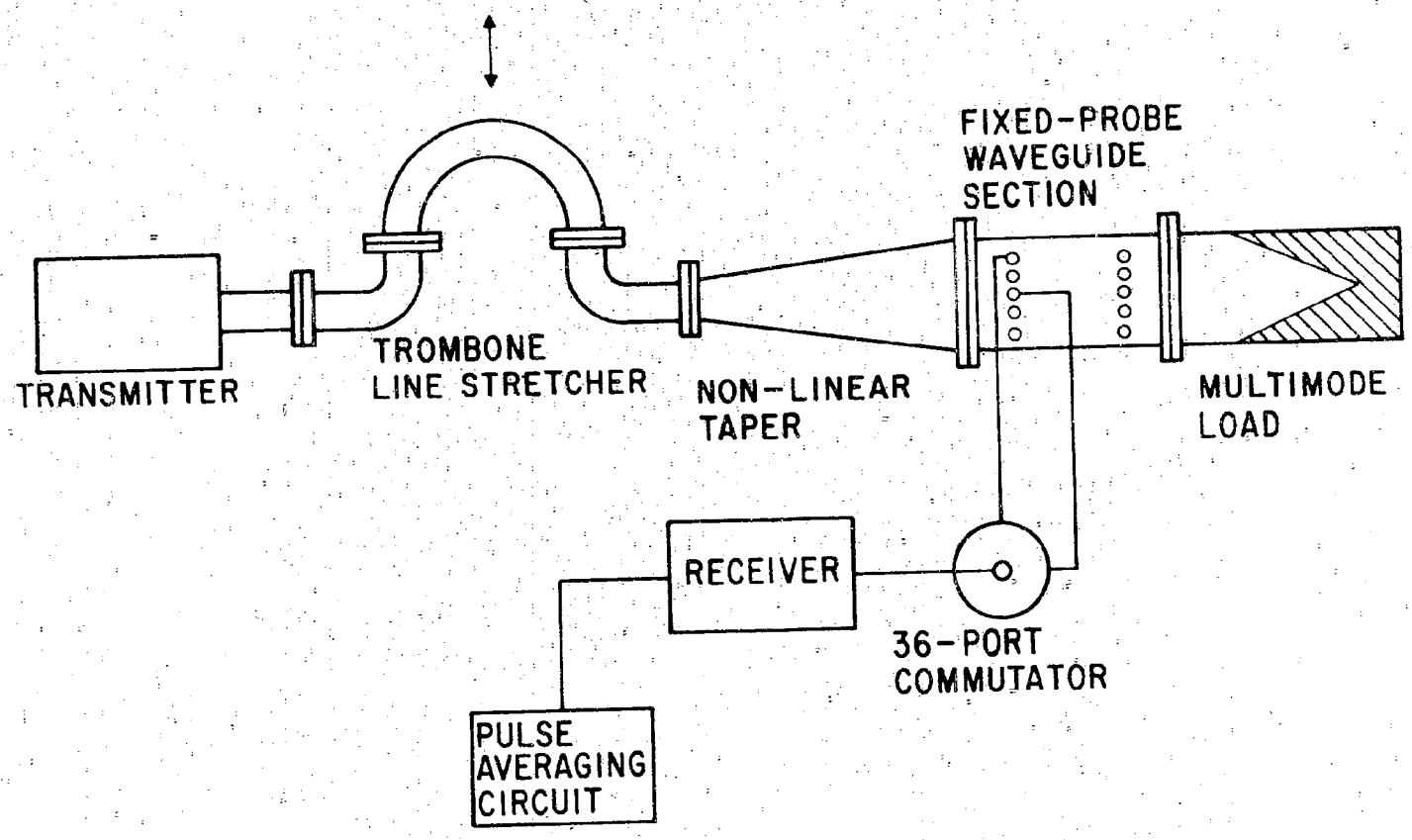

FIGURE 1. BLOCK DIAGRAM OF FIXED PROBE MULTIMODE SPURIOUS EMISSION POWER MEASURING EQUIPMENT

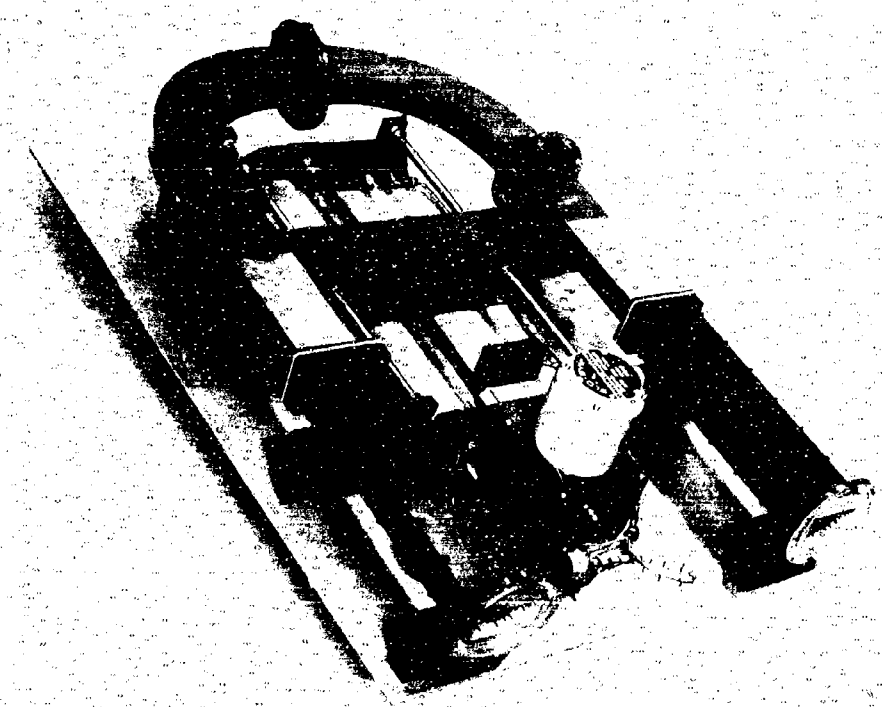

FIGURE 2. TROMBONE LINE STRETCHER

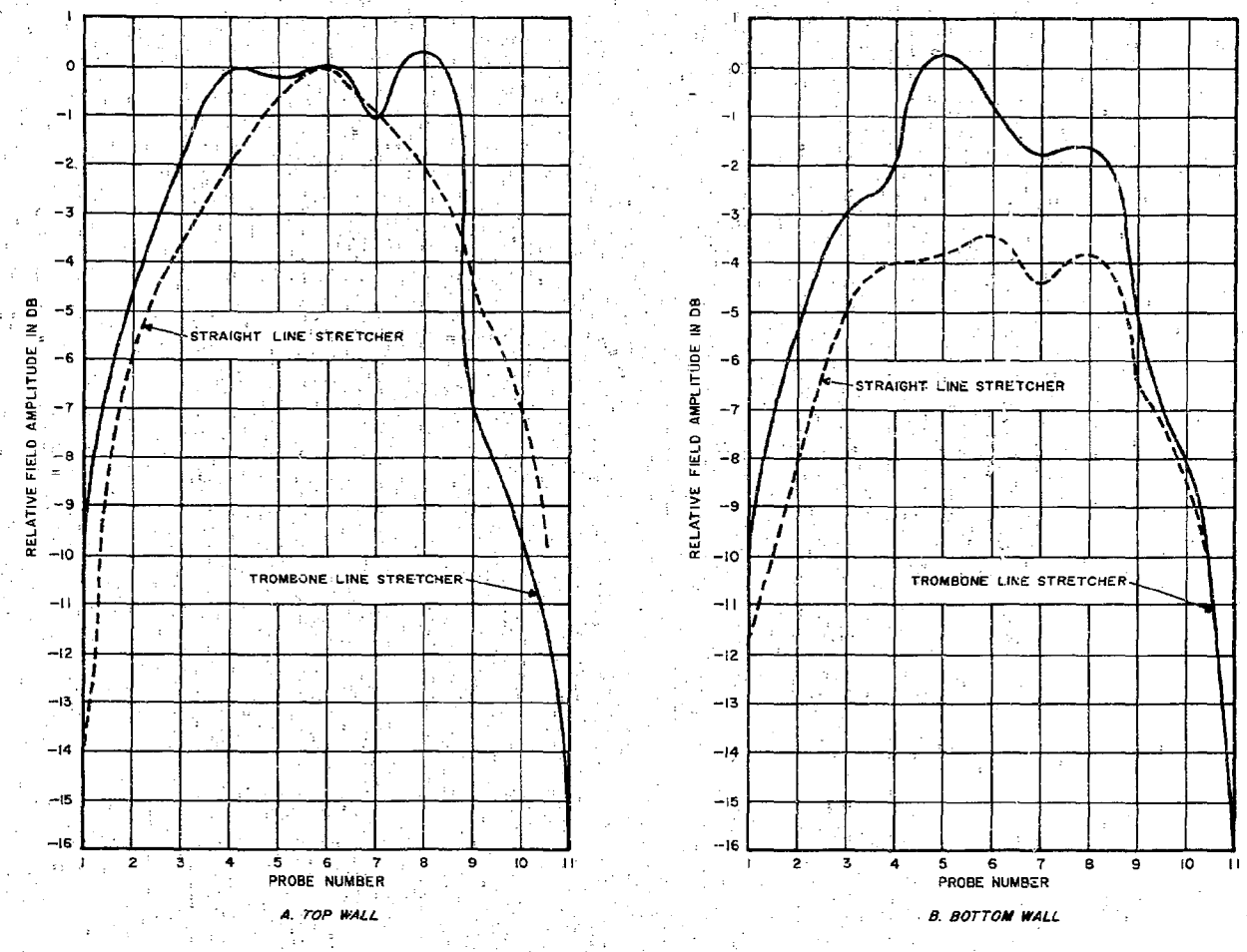

FIGURE 3. TOP- AND BOTTOM-WALL ELECTRIC-FIELD PLOTS, WITH STRAIGHT AND TROMBONE LINE STRETCHERS

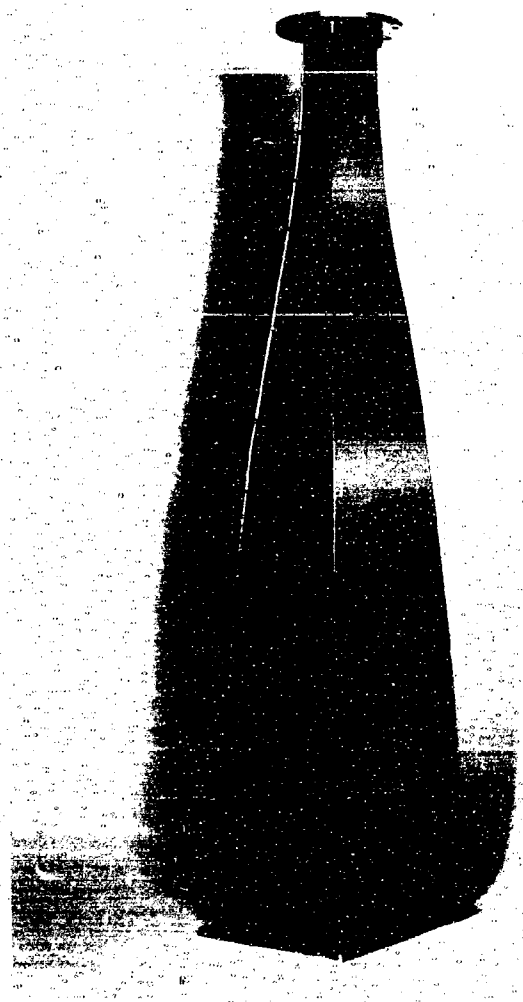

FIGURE 4. NONLINEAR TAPER

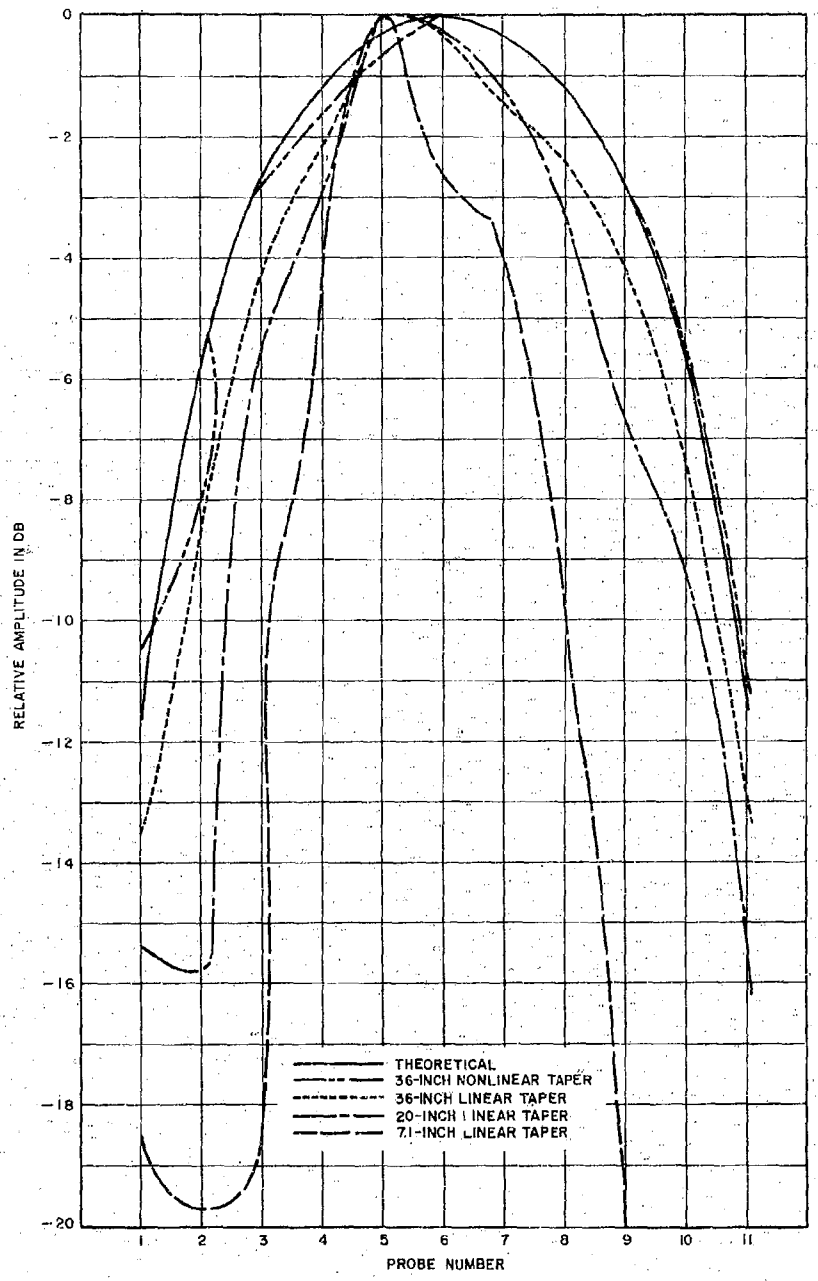

FIGURE 5. COMPARISON OF MEASURED TE_{10} ELECTRIC-FIELD AMPLITUDE TRANSFORMED BY FOUR TAPERS TO THEORETICAL TE_{10} ELECTRIC-FIELD AMPLITUDE

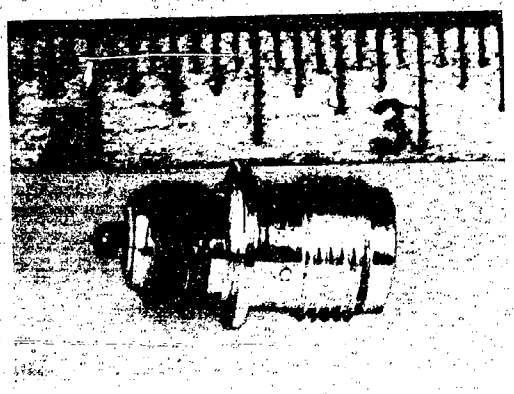

FIGURE 6. FIXED PROBE

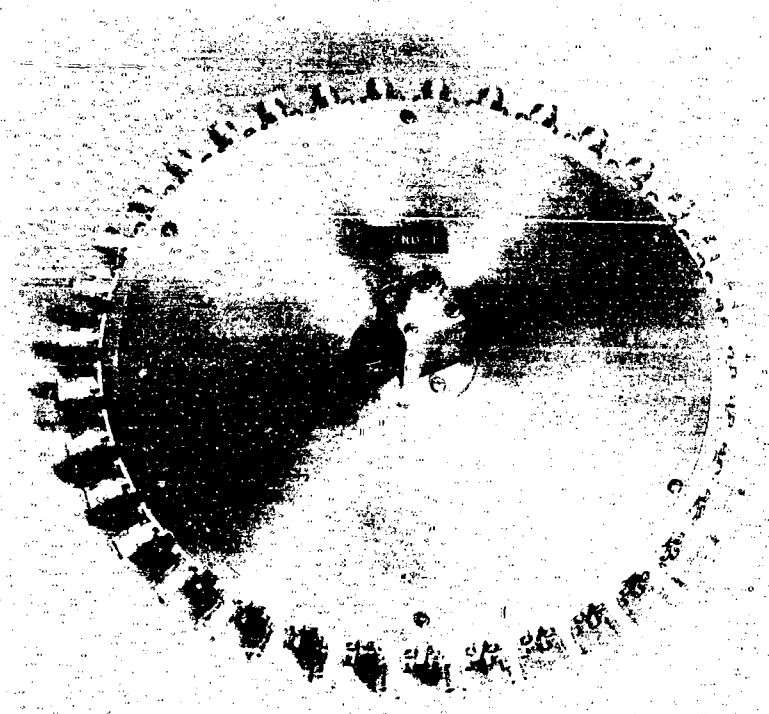

FIGURE 7. NONCONTACTING COMMUTATOR

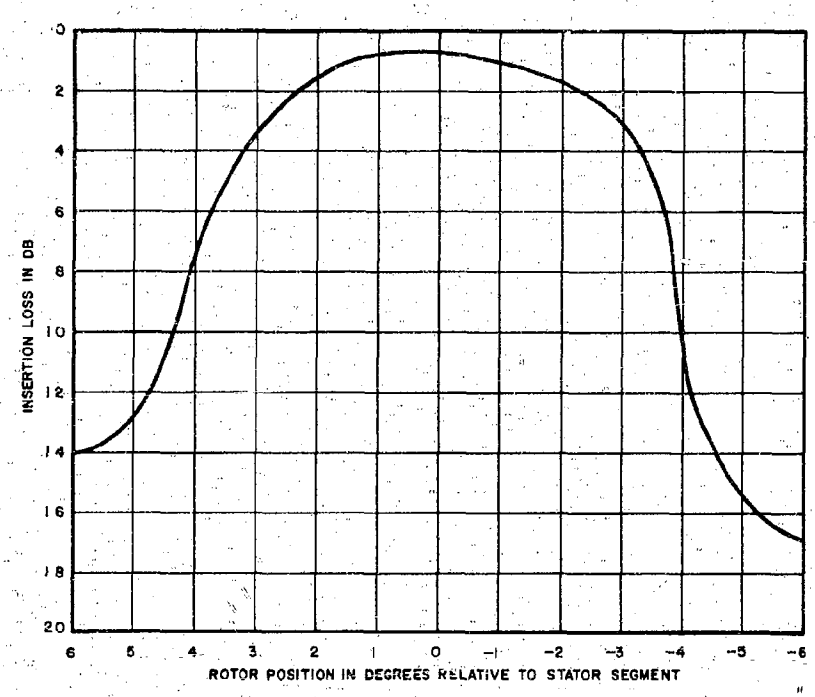

FIGURE 8. BAND I COMMUTATOR, TYPICAL TRANSFER FUNCTION

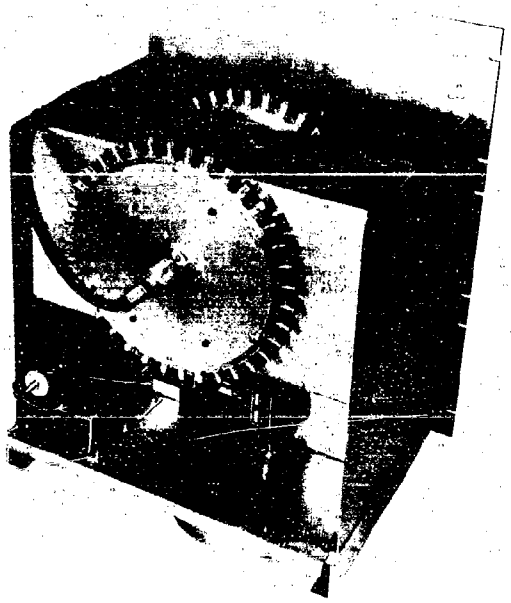

A. REAR VIEW

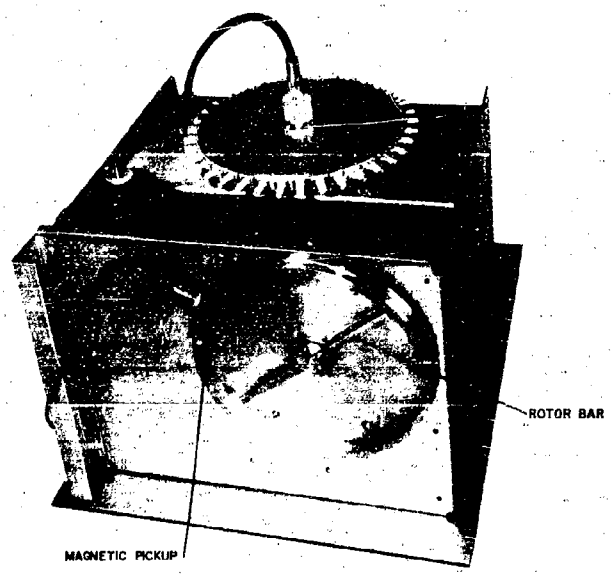

B. BOTTOM VIEW

FIGURE 9. PROBE-SAMPLING UNIT

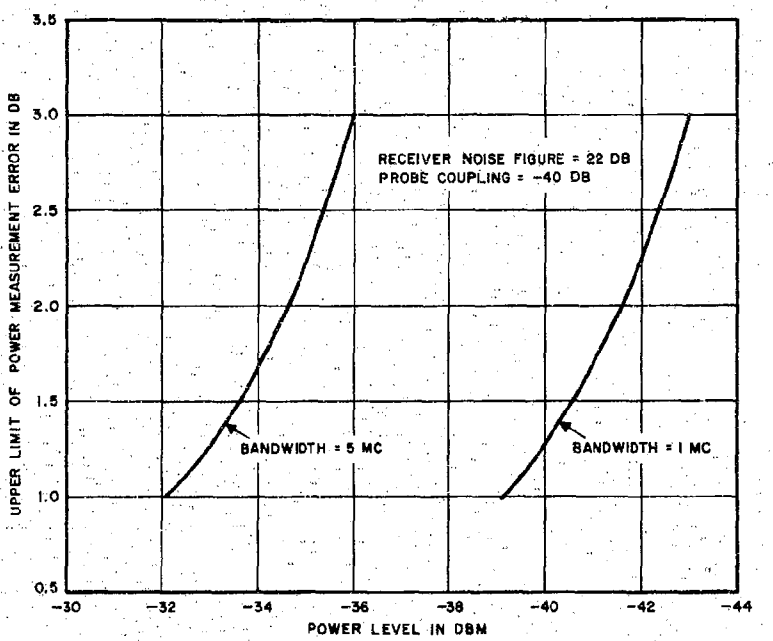

FIGURE 10. UPPER-LIMIT ERROR VS POWER LEVEL

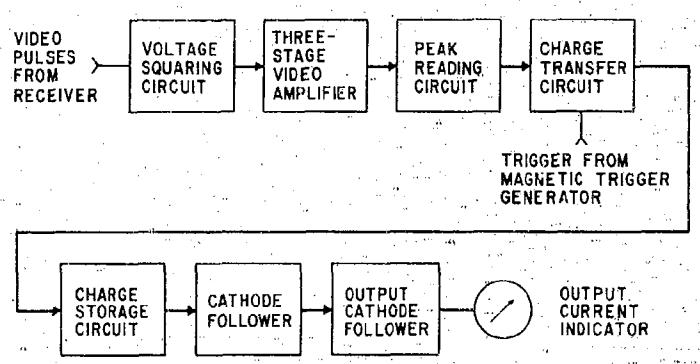

FIGURE 11. BLOCK DIAGRAM OF AVERAGING AMPLIFIER

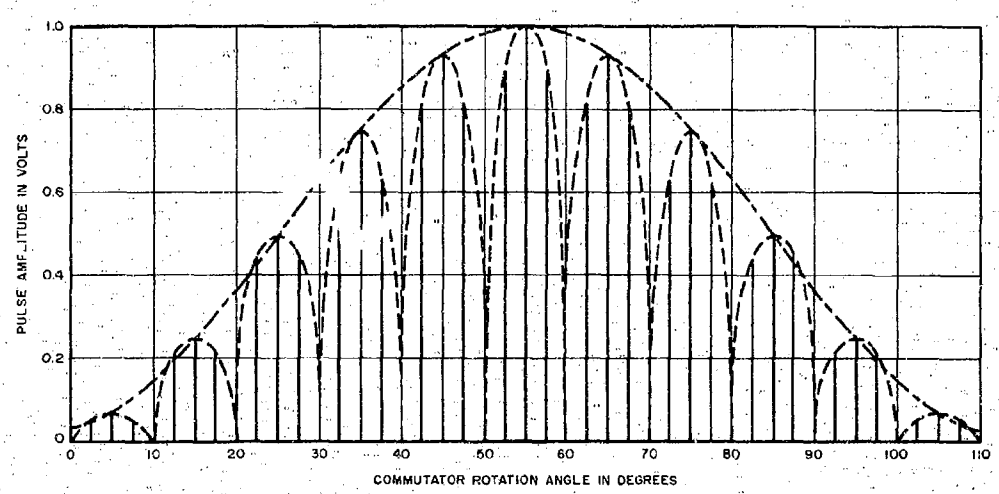

FIGURE 12. OUTPUT OF SQUARING AMPLIFIER VS COMMUTATOR ROTATION ANGLE

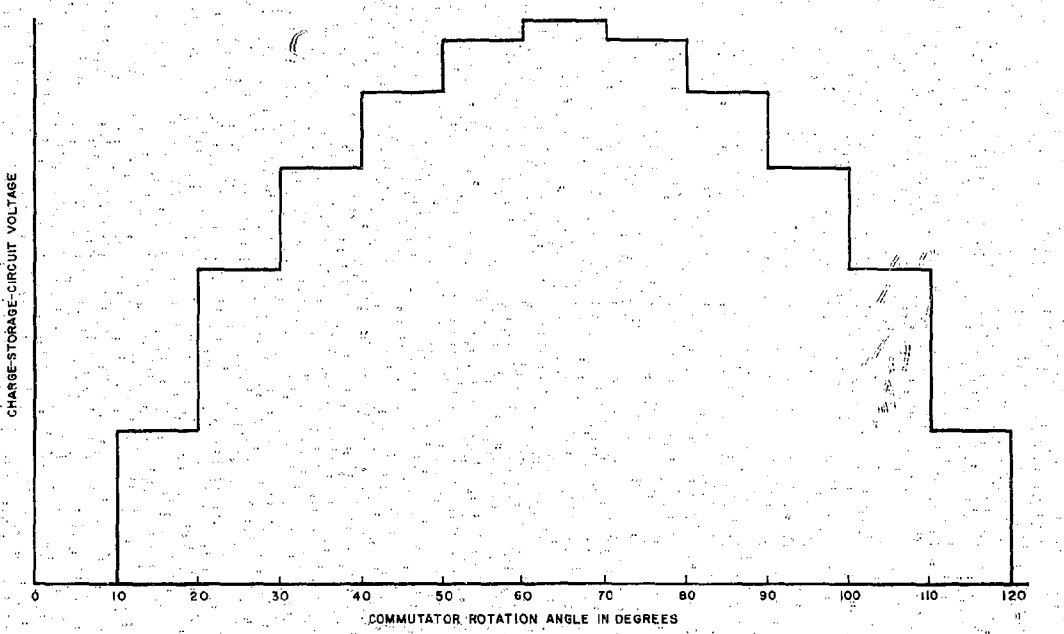

FIGURE 13. CHARGE-STORAGE-CIRCUIT VOLTAGE VS COMMUTATOR ROTATION ANGLE

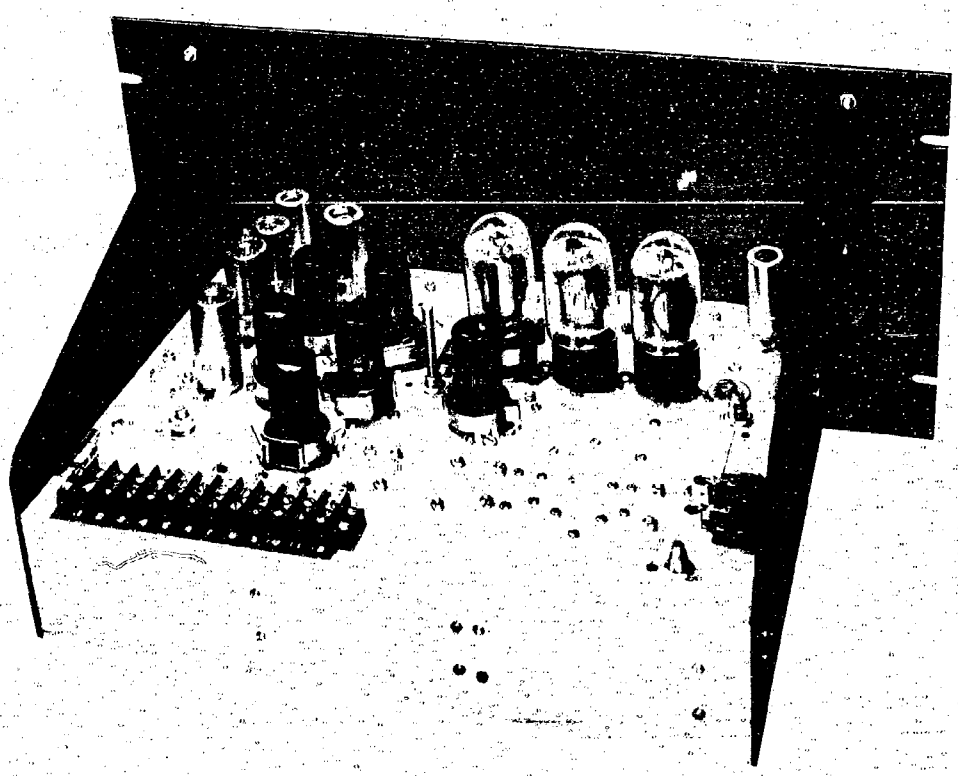

FIGURE 14. AVERAGING AMPLIFIER CHASSIS

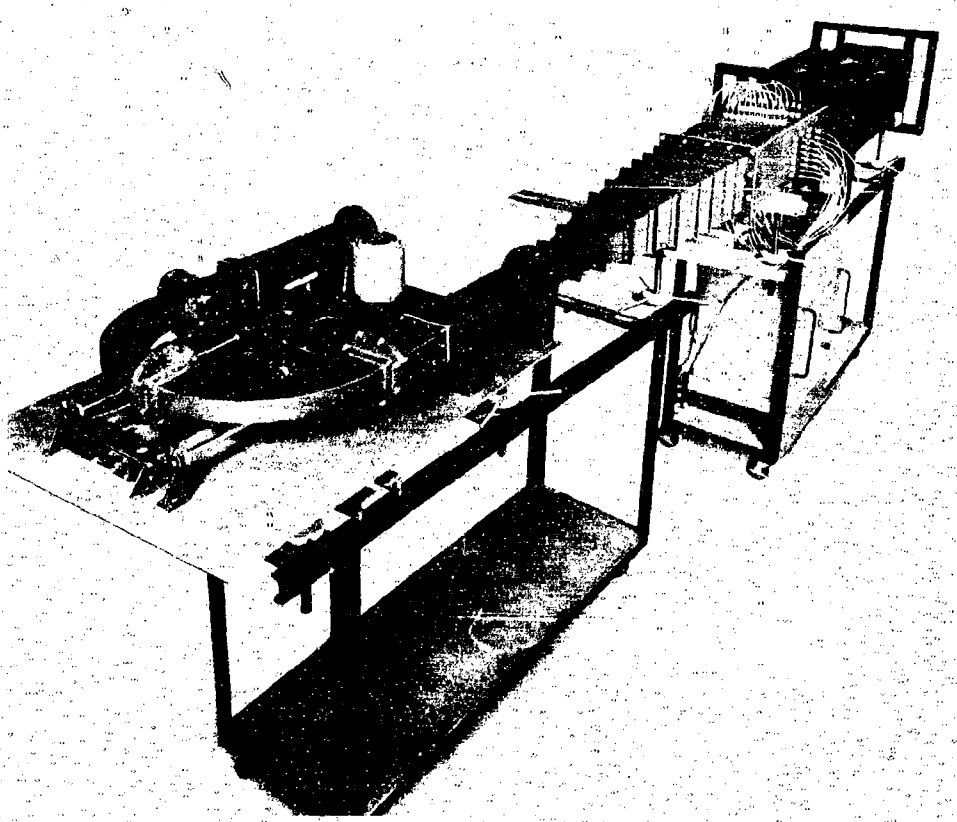

FIGURE 15. WAVEGUIDE COMPONENTS AND SUPPORTING CARTS

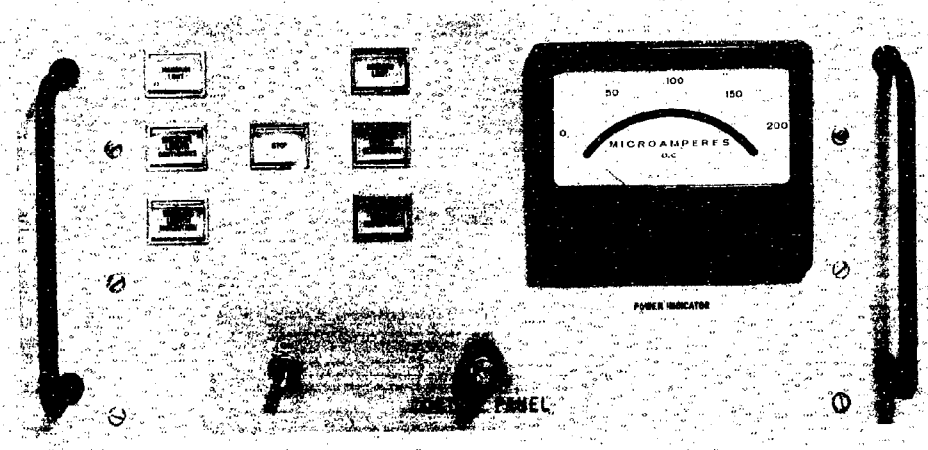

FIGURE 16. CONTROL PANEL

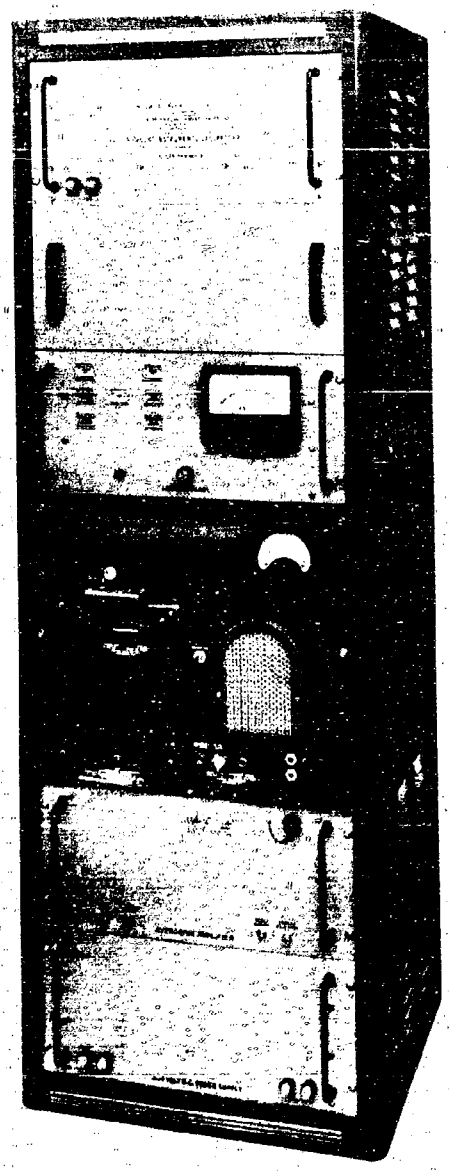

FIGURE 17. INSTRUMENTATION RACK

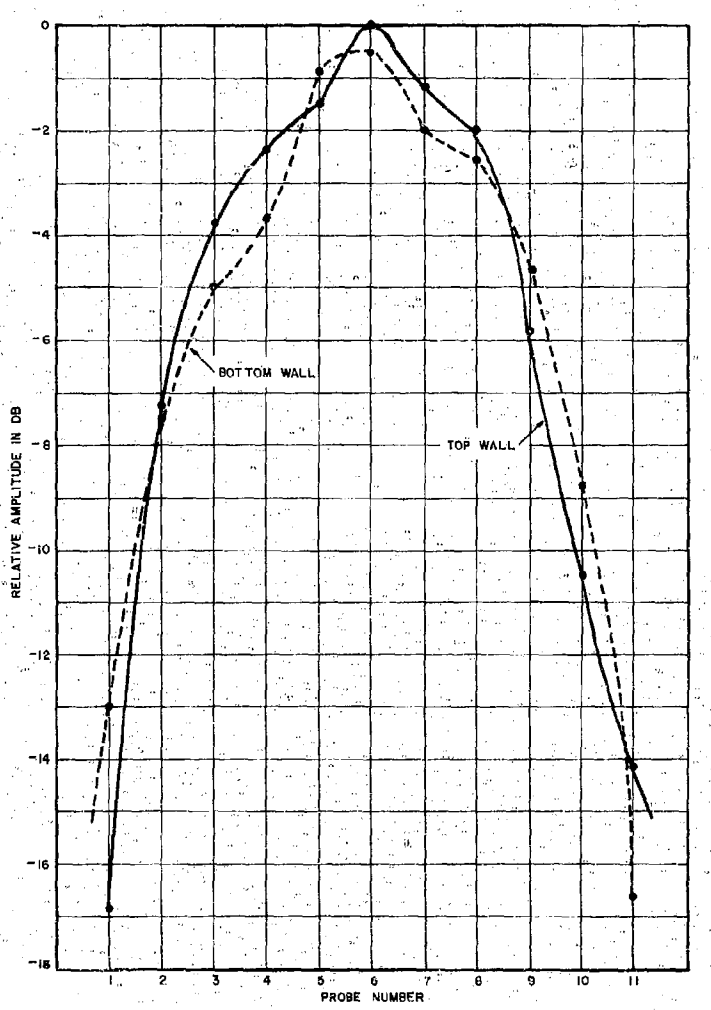

FIGURE 18. MEASURED TE_{10} ELECTRIC-FIELD AMPLITUDE AT 4.3 GC

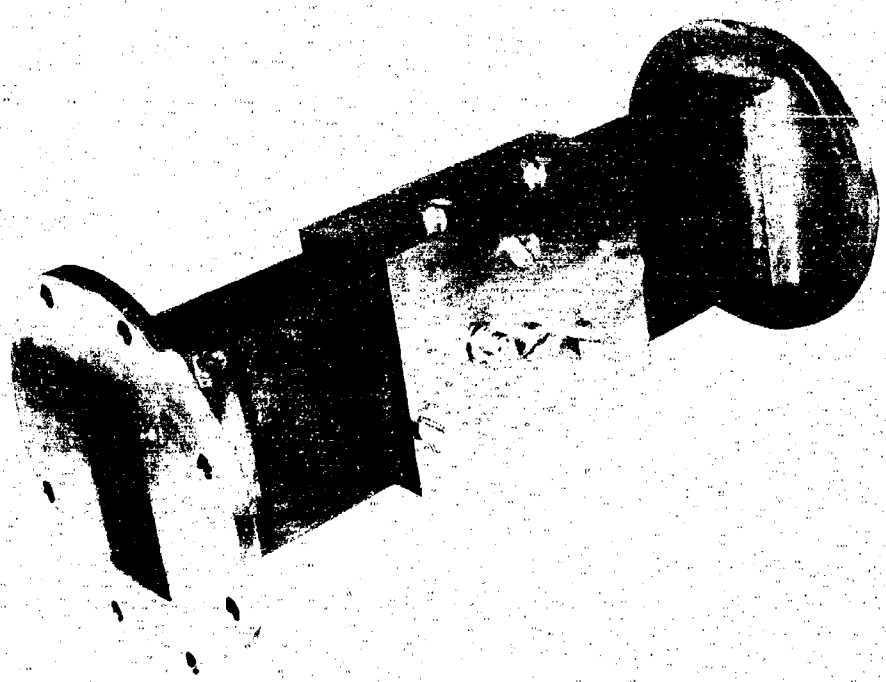

FIGURE 19. MODE LAUNCHER

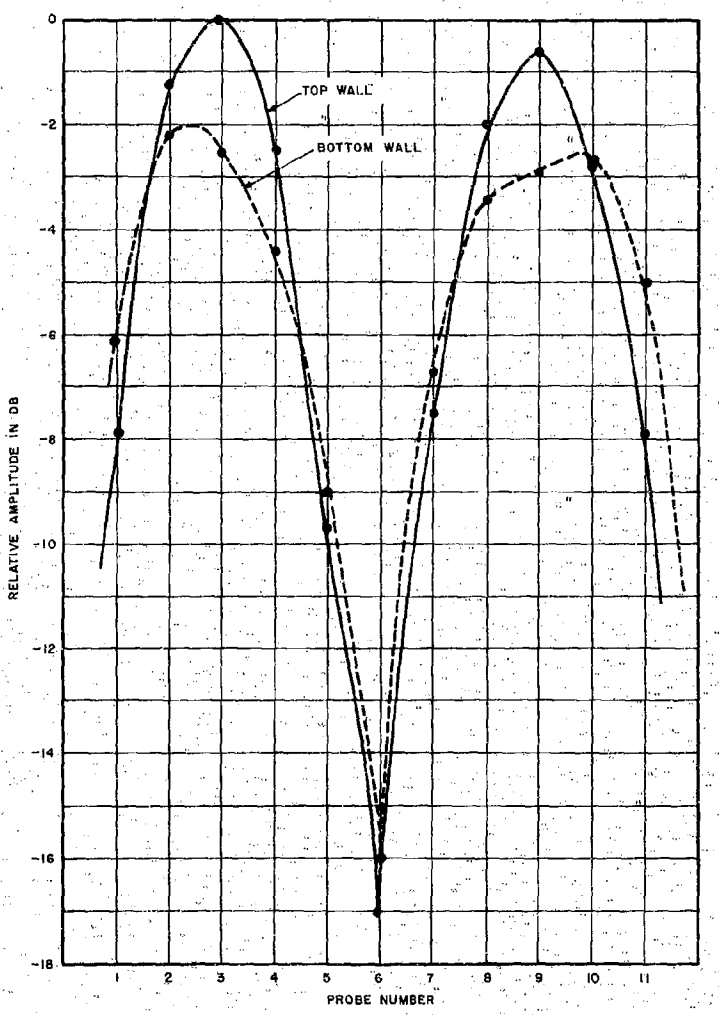

FIGURE 20. MEASURED TE_{20} ELECTRIC-FIELD AMPLITUDE AT 4.3 GC

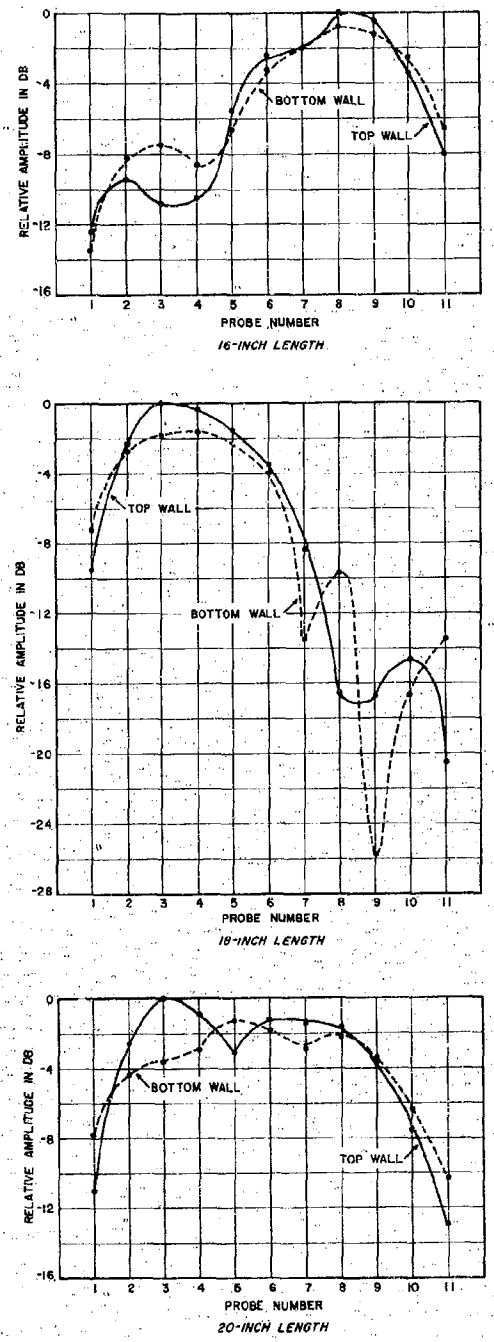

FIGURE 21. MEASURED TE_{10} AND TE_{20} ELECTRIC-FIELD AMPLITUDE AT 4.3 GC FOR VARIOUS DISPERSIVE LENGTHS

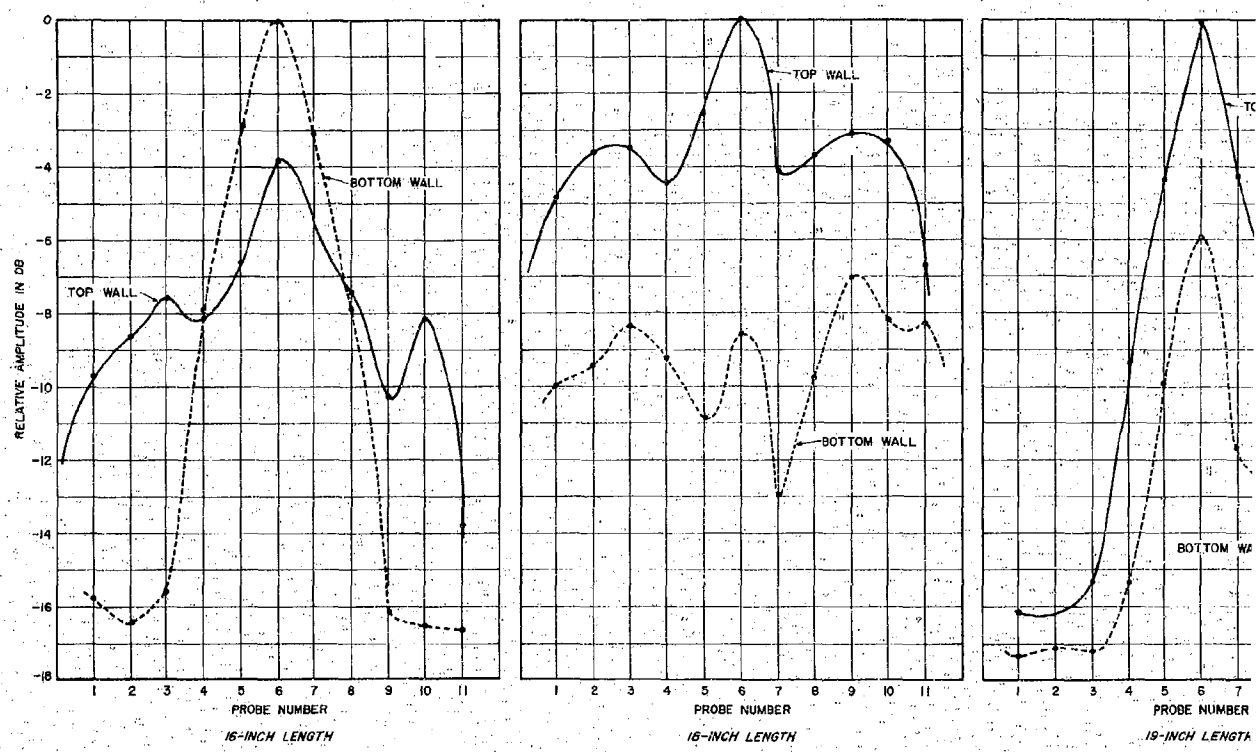
RELATIVE AMPLITUDE IN DB
0
-2
-4
-6
-8
-10
-12
-14
-16
-18
TOP WALL
BOTTOM WALL
1 2 3 4 5 6 7 8 9 10 11
PROBE NUMBER
16-INCH LENGTH
TOP WALL
BOTTOM WALL
1 2 3 4 5 6 7 8 9 10 11
PROBE NUMBER
18-INCH LENGTH
1 2 3 4 5 6 7
PROBE NUMBER
19-INCH LENGTH

1

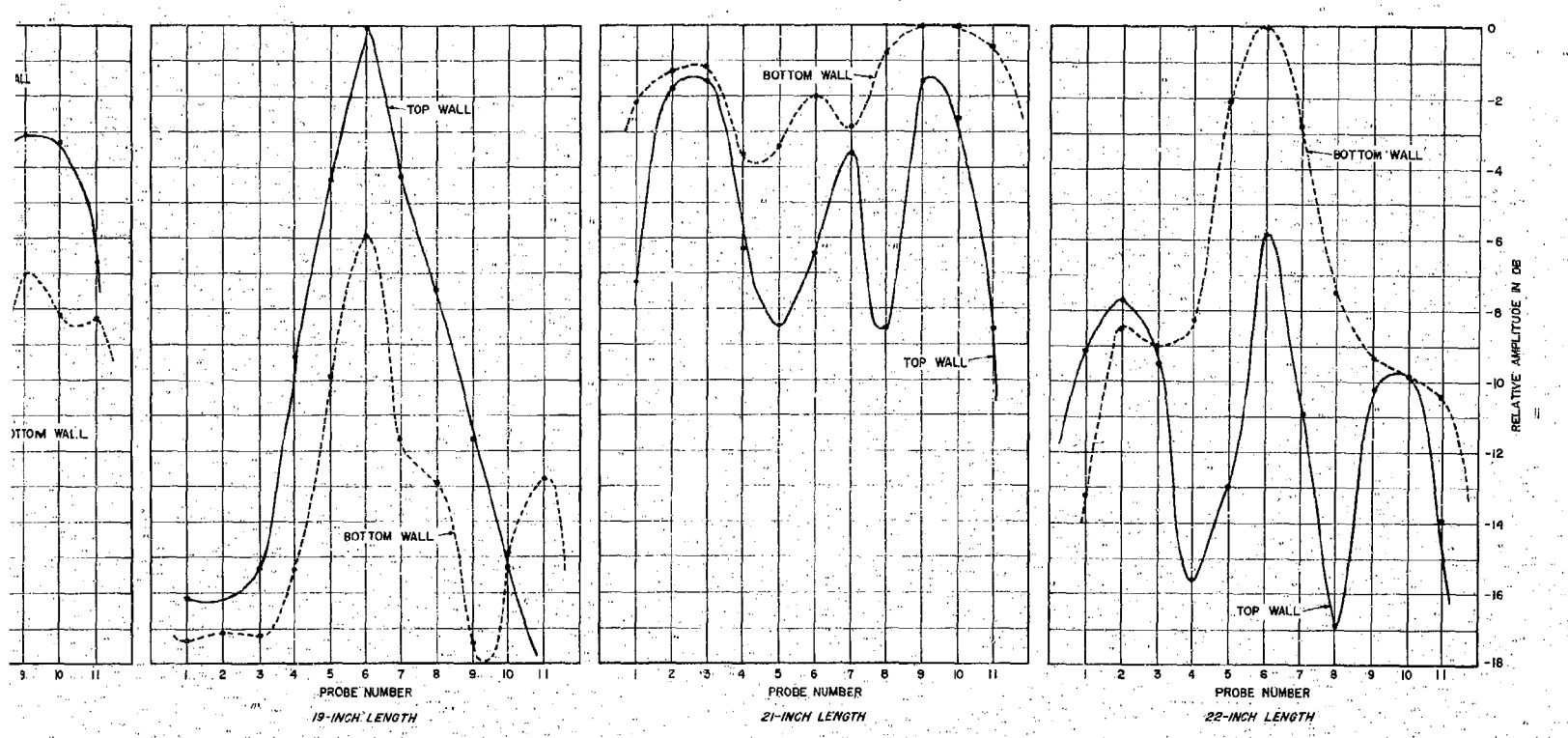

FIGURE 22. MEASURED MULTIMODE ELECTRIC-FIELD AMPLITUDE AT 7.0 GC FOR VARIOUS DISPERSIVE LENGTHS

2

FIGURE 22

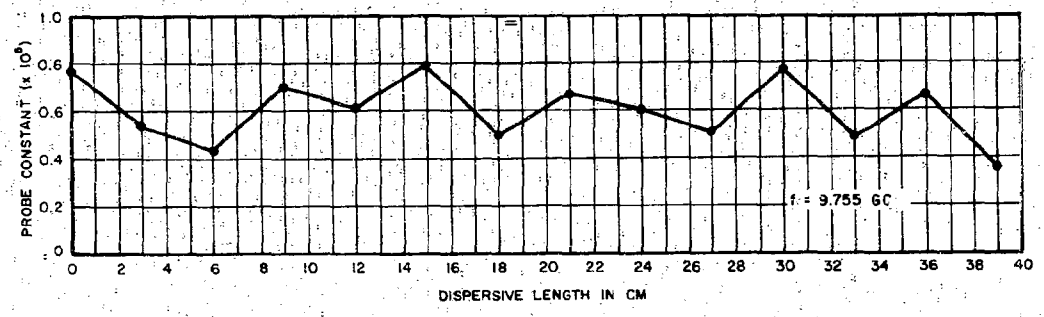

A. BROAD-WALL ELECTRIC PROBE FEED

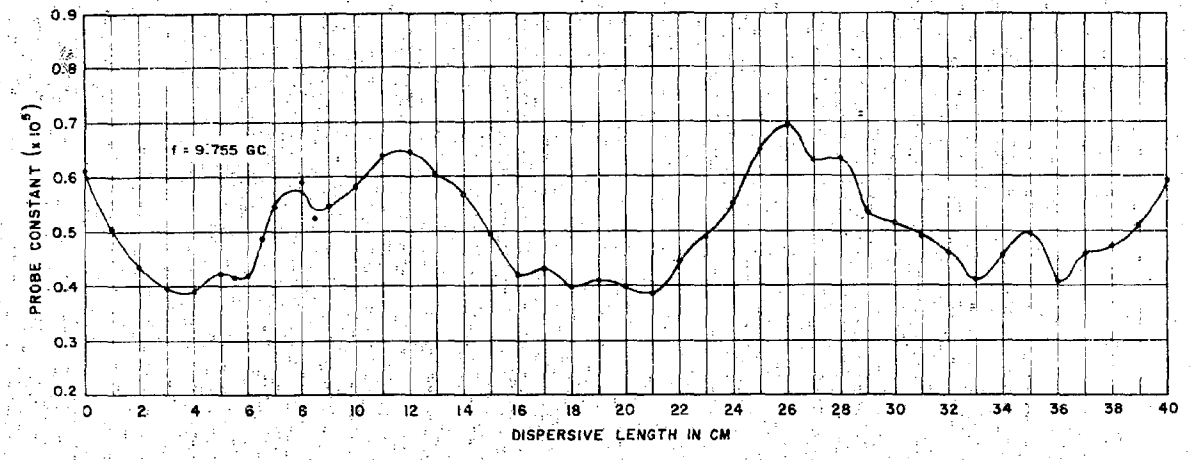

B. DOORKNOB FEED

FIGURE 23. RATIO OF WAVEGUIDE POWER TO AVERAGE PROBE-COUPLED POWER VS LENGTH OF DISPERSIVE LINE STRETCHER

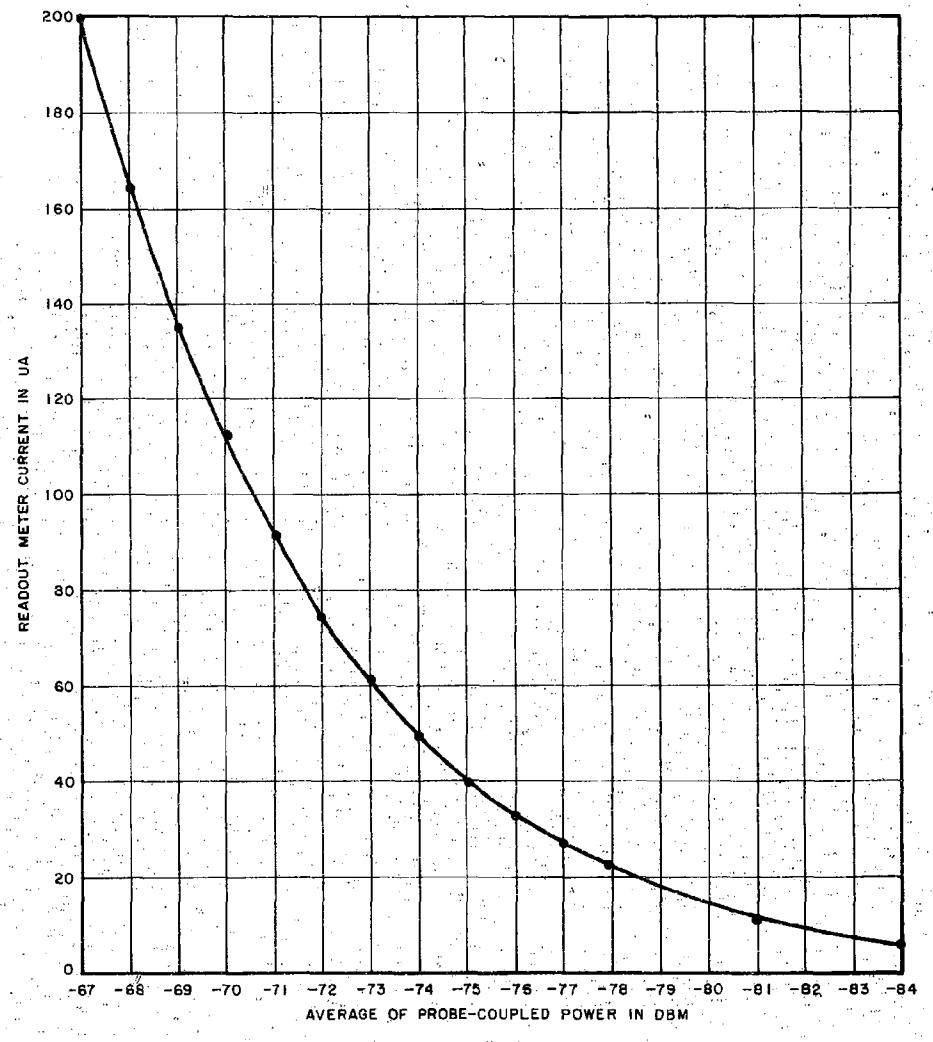

FIGURE 24. AVERAGING AMPLIFIER CALIBRATION CURVE

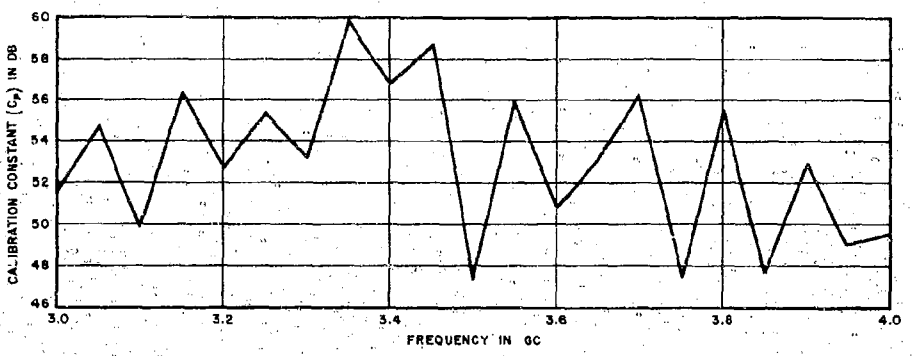

A. 3 TO 4 GC

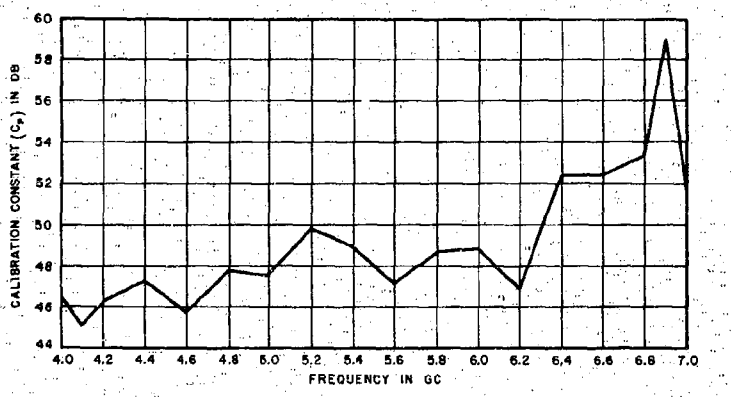

B. 4 TO 7 GC

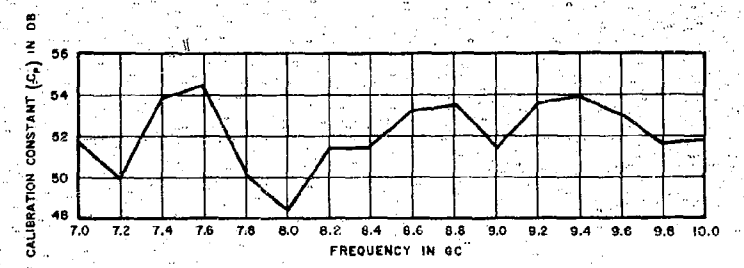

C. 7 TO 10 GC

FIGURE 25. FIXED PROBE CALIBRATION CONSTANT

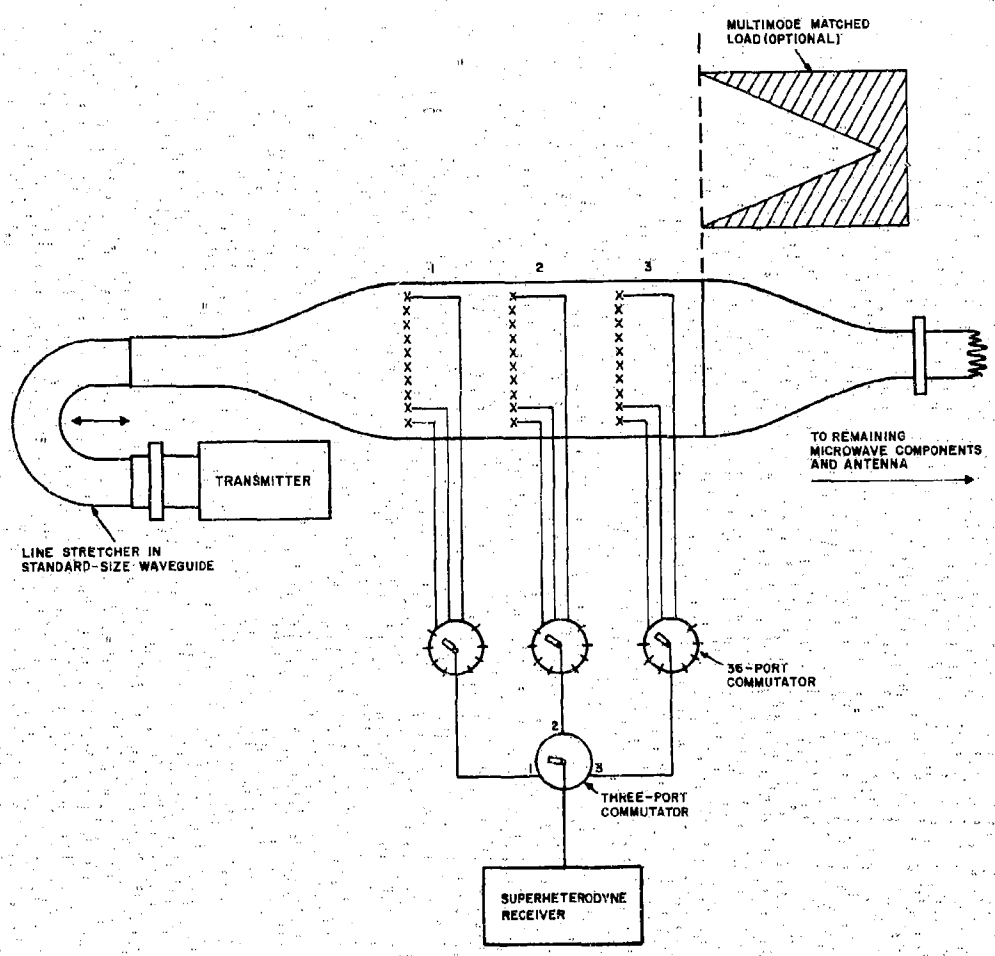

FIGURE 26. DIAGRAM OF EQUIPMENT TO MEASURE SPURIOUS EMISSION POWER ABSORBED BY MISMATCHED ANTENNA

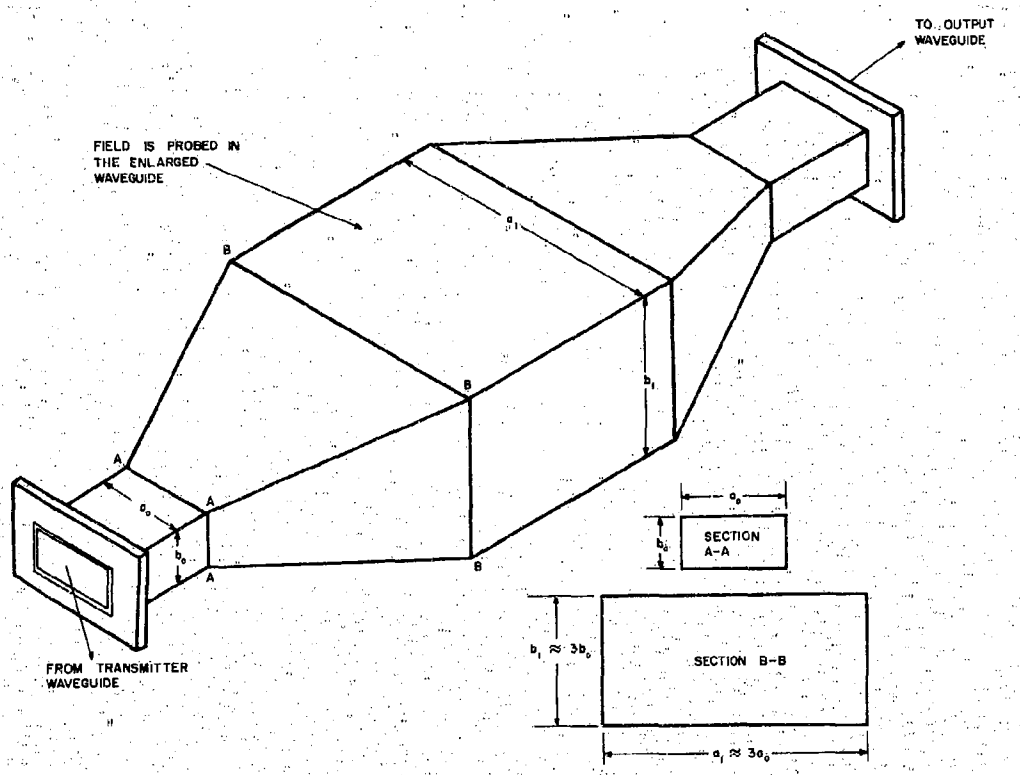

A. ENLARGED WAVEGUIDE

FIGURE 27. ENLARGED WAVEGUIDE AND ARRANGEMENT OF MOVABLE PROBES FOR MEASURING $|E_x|$ and $|E_y|$ (SHEET 1 OF 2)

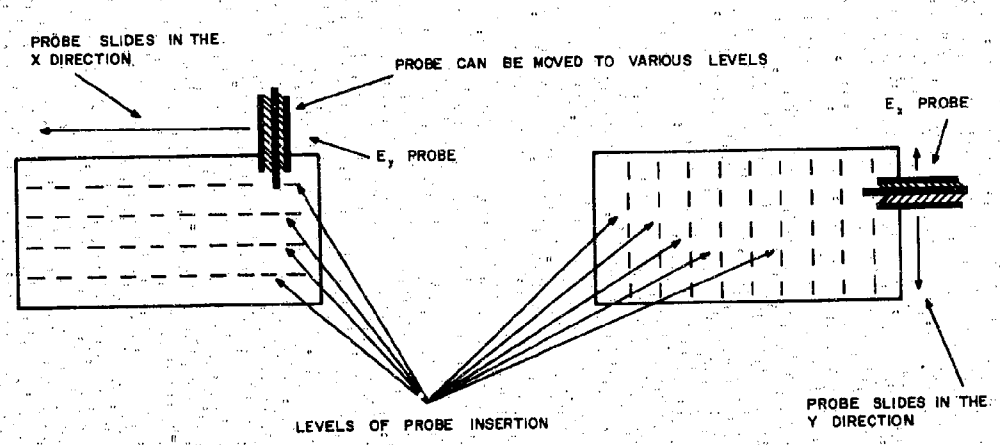

PROBE FOR SAMPLING $|E_y|$ AS A FUNCTION OF X AND Y

PROBE FOR SAMPLING $|E_x|$ AS A FUNCTION OF X AND Y

B. E_x AND E_y PROBES

FIGURE 27
(SHEET 2 OF 2)

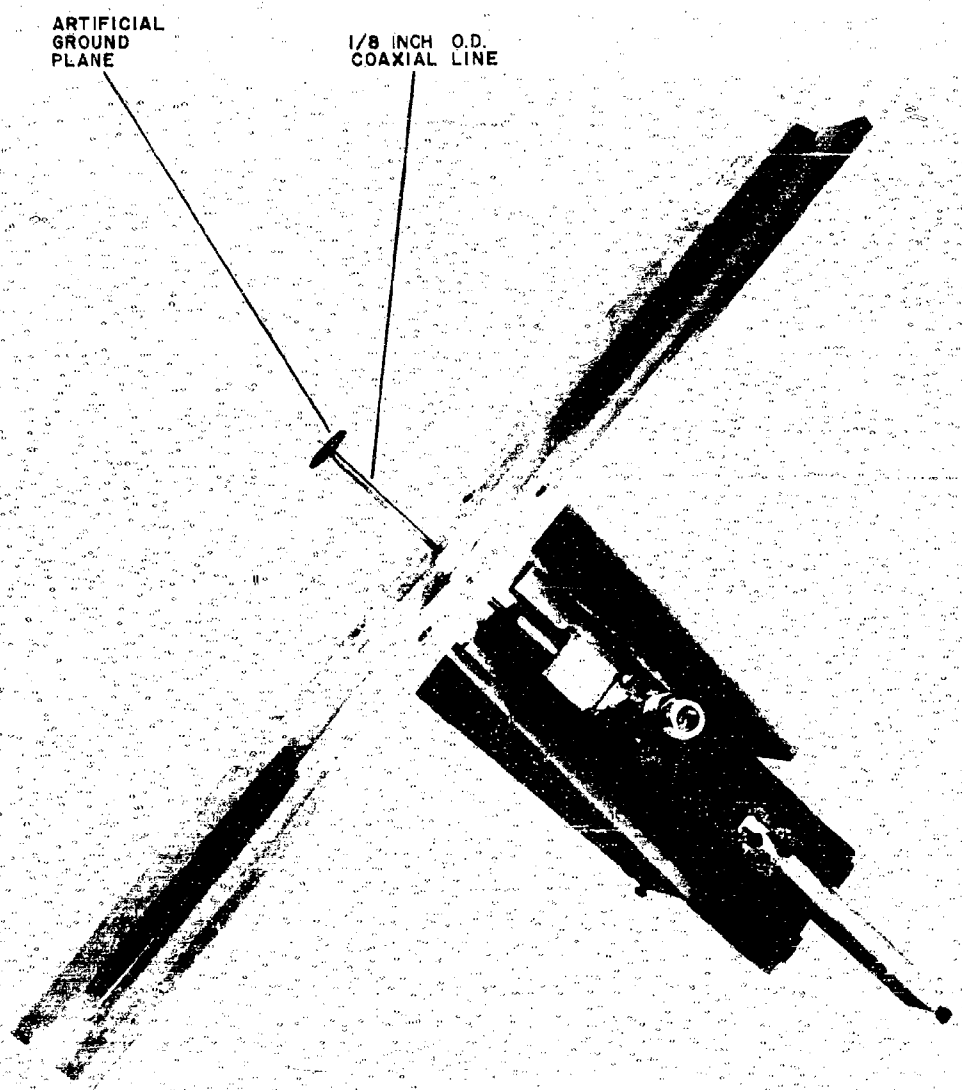

A. PROBE AND CARRIAGE ASSEMBLY

FIGURE 28. PROBE AND CARRIAGE ASSEMBLY AND PROBE AND ENLARGED SECTION OF WAVEGUIDE
(SHEET 1 OF 2)

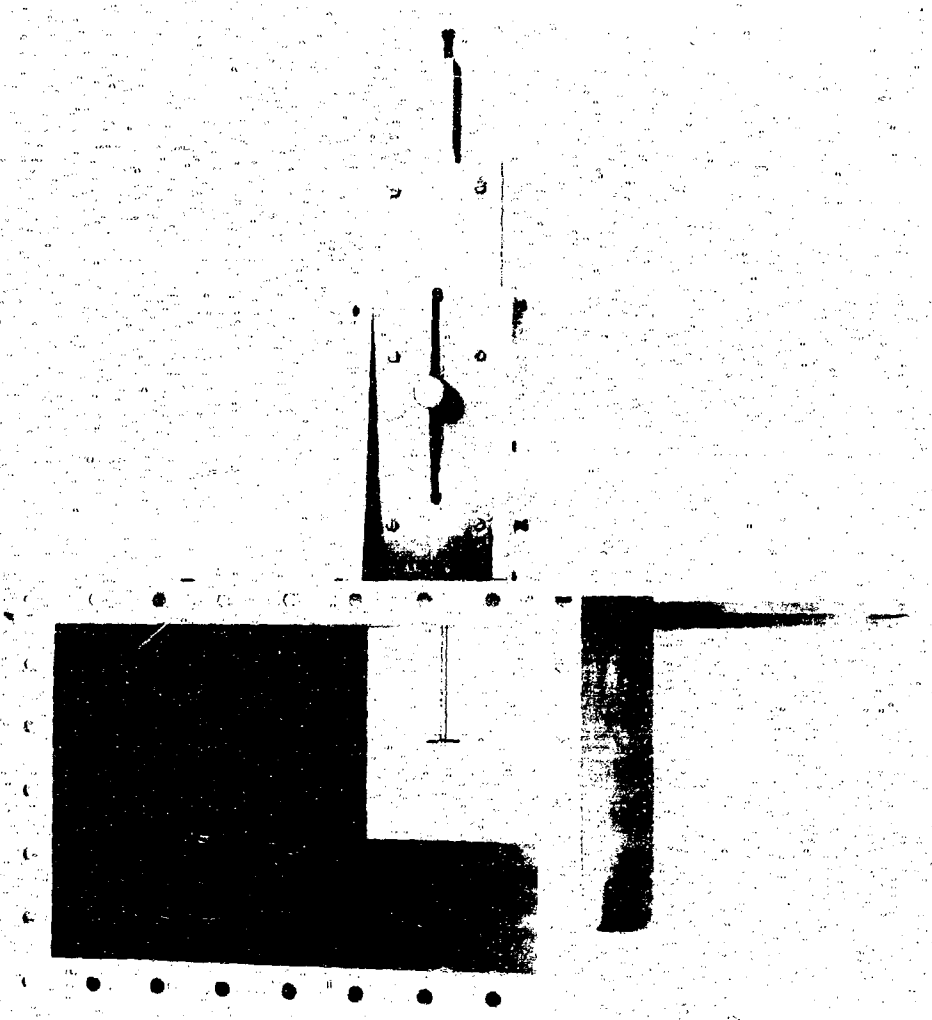

B. PROBE AND ENLARGED SECTION OF WAVEGUIDE

FIGURE 28
(SHEET 2 OF 2)

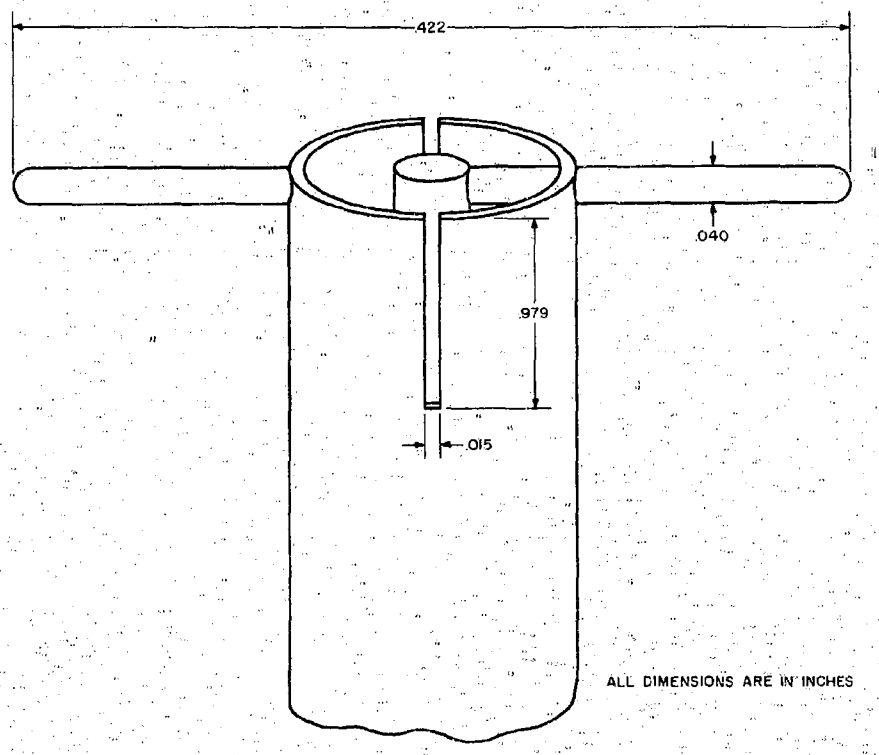

FIGURE 29. SLOTTED BALANCED DIPOLE PROBE

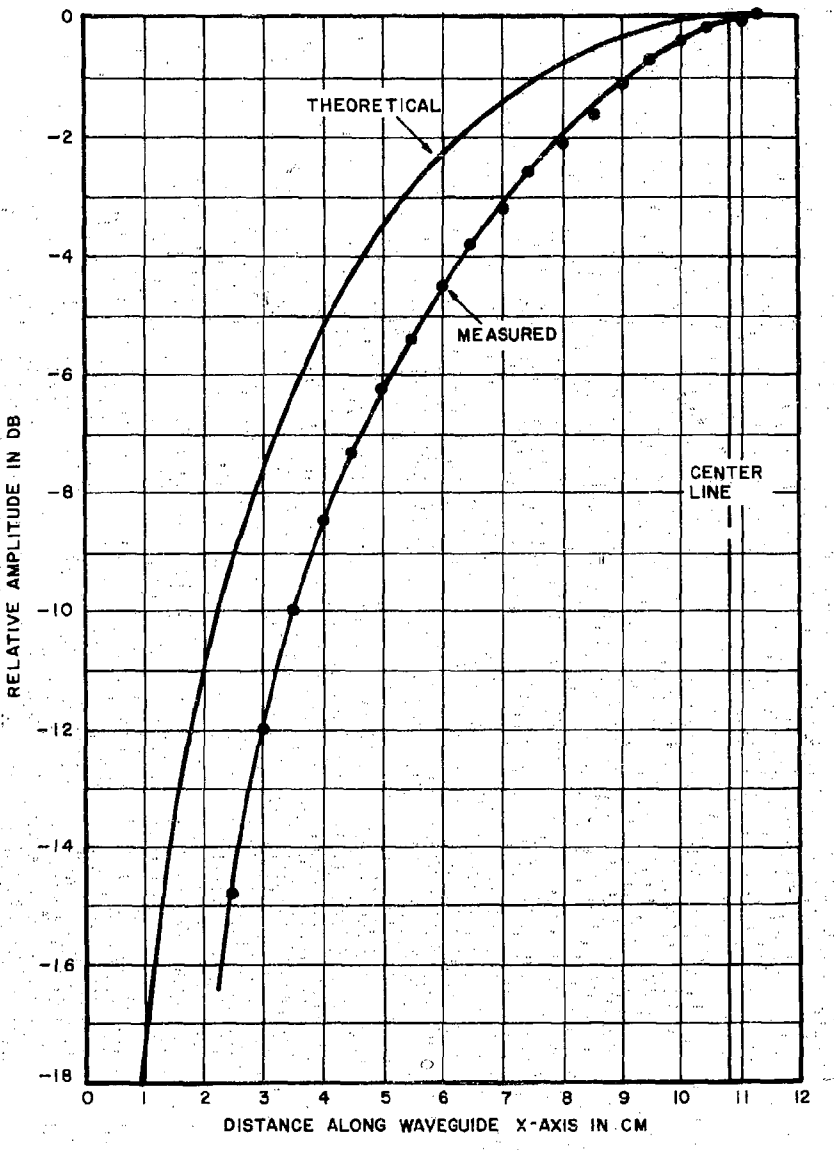

FIGURE 30. TE_{10} ELECTRIC-FIELD AMPLITUDE MEASURED WITH SLOTTED DIPOLE AT 3.8 GC

FIGURE 31. BALANCED DIPOLE PROBE

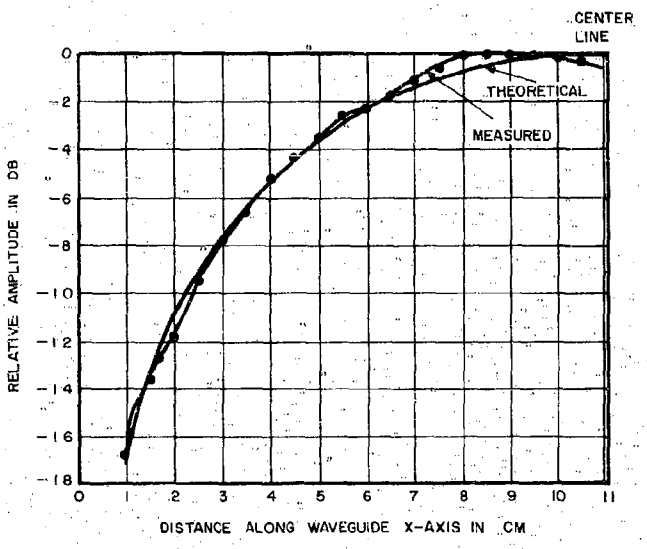

FIGURE 32. TE_{10} ELECTRIC-FIELD AMPLITUDE MEASURED WITH BALANCED DIPOLE PROBE AT 4.3 GC

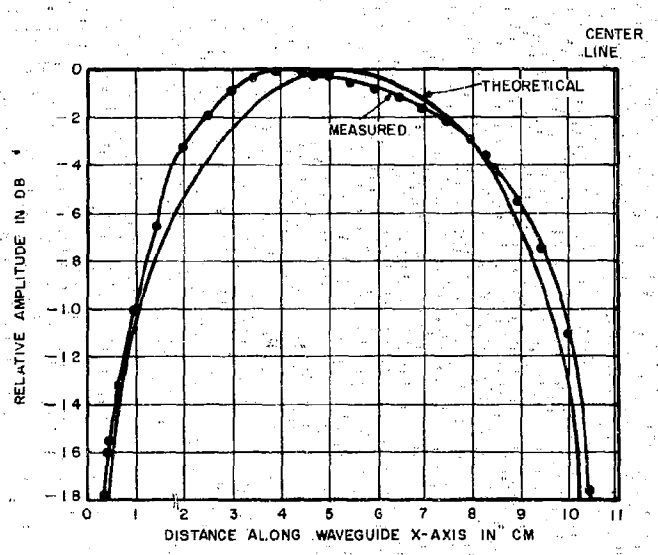

FIGURE 33. TE_{20} ELECTRIC-FIELD AMPLITUDE OBTAINED WITH BALANCED DIPOLE PROBE AT 4.3 GC

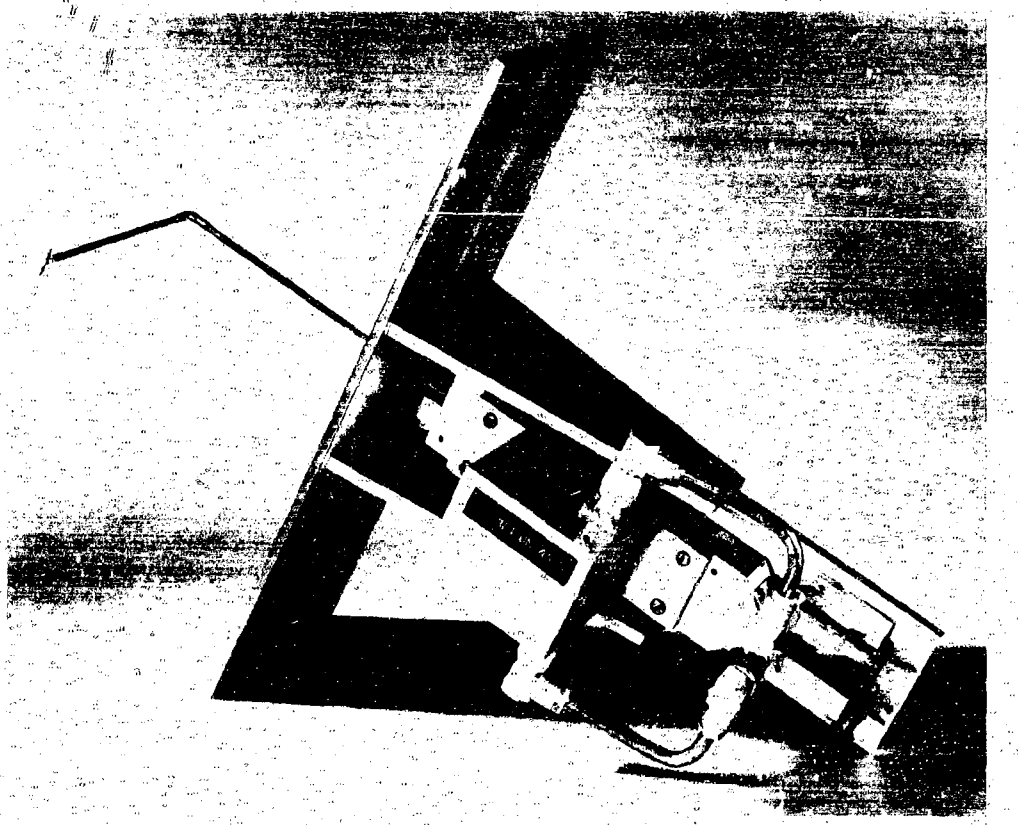

FIGURE 34. Z-AXIS BALANCED DIPOLE PROBE

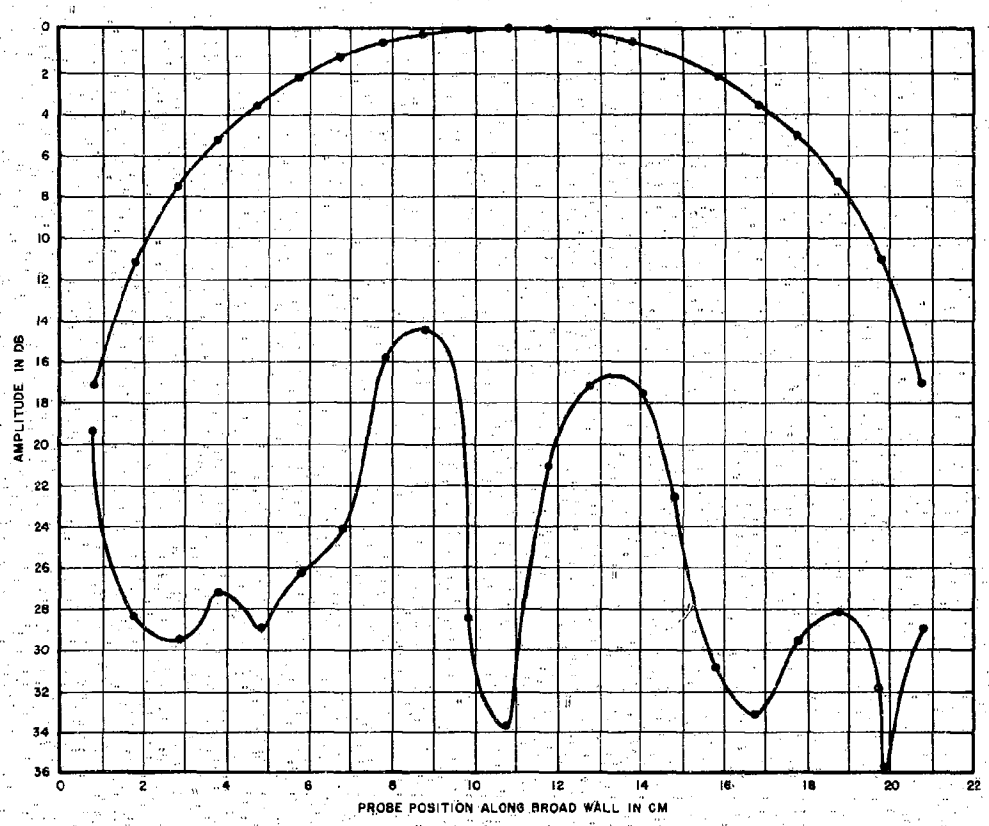

FIGURE 35. ELECTRIC-FIELD PLOT OBTAINED WITH $|E_x|$ and $|E_y|$ PROBES WITH DOMINANT MODE PROPAGATING IN SMALL GUIDE AT 3.8 GC

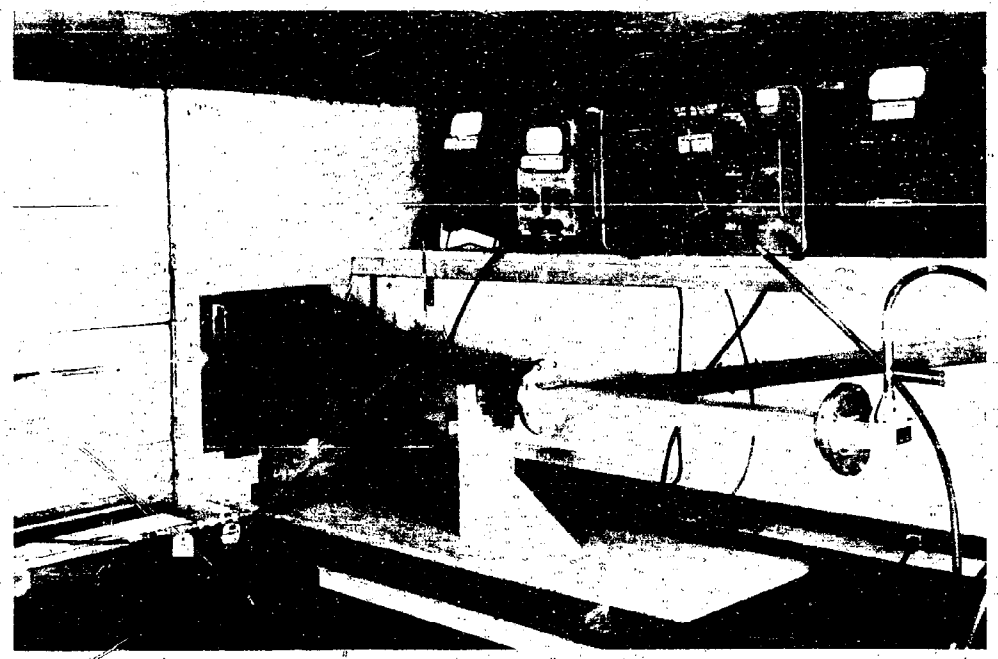

FIGURE 36. FREE-SPACE MEASUREMENT SETUP

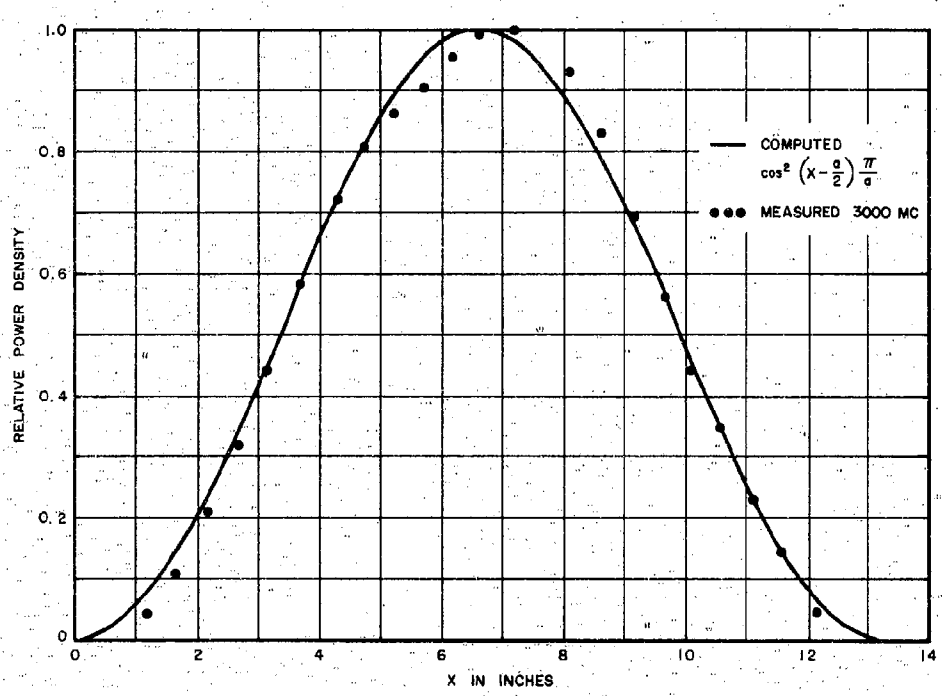

FIGURE 37. COMPARISON OF DENSITIES OF MEASURED POWER AND COMPUTED POWER OF S-BAND HORN FOR TE_{10} MODE

APPENDIX I

POWER FLOW IN RECTANGULAR WAVEGUIDE IN TERMS OF POWER MEASURED BY PROBES AT THE BOUNDARY

An expression is derived for power flow in rectangular waveguide as a function of the power measured by electric probes located at the boundary of the guide in a plane transverse to the direction of propagation.

The power flow in an arbitrarily large rectangular waveguide (Figure I-1), as shown in Appendix II, is

$$P = \frac{1}{\eta} \int_0^b \int_0^a \left(|E_x|^2 + |E_y|^2 \right) dx\, dy \qquad \text{(I-1)}$$

where

η = intrinsic impedance--120π for free space,

E_x, E_y = rms values of x- and y-components of the electric field

Now, from the general theory of propagation in rectangular waveguide,

$$E_x = \sum_{m=0}^{M} \sum_{n=0}^{N} E_{mnx} \cos \frac{m\pi x}{a} \sin \frac{n\pi y}{b} \qquad \text{(I-2)}$$

and

$$E_y = \sum_{m=0}^{M} \sum_{n=0}^{N} E_{mny} \sin \frac{m\pi x}{a} \cos \frac{n\pi y}{b} \qquad \text{(I-3)}$$

where E_{mnx} and E_{mny} are the x- and y-components of the electric field of the mode whose indices are m,n. Substituting equations I-2 and I-3 into equation I-1 yields

$$P = \frac{1}{\eta}\int_0^b\int_0^a\left[\left(\sum_{m=0}^{M}\sum_{n=0}^{N} E_{mnx}\cos\frac{m\pi x}{a}\sin\frac{n\pi y}{b}\right)\left(\sum_{m=0}^{M}\sum_{n=0}^{N} E^*_{mnx}\cos\frac{m\pi x}{a}\sin\frac{n\pi y}{b}\right) + \left(\sum_{m=0}^{M}\sum_{n=0}^{N} E_{mny}\sin\frac{m\pi x}{a}\cos\frac{n\pi y}{b}\right)\left(\sum_{m=0}^{M}\sum_{n=0}^{N} E^*_{mnx}\sin\frac{m\pi x}{a}\cos\frac{n\pi y}{b}\right)\right] dx\, dy \qquad \text{(I-4)}$$

When the integrations in equation I-4 are carried out, the result is

$$P = \frac{ab}{2\eta}\left(\sum_{n=1}^{N}\left|E_{onx}\right|^2 + \sum_{m=1}^{M}\left|E_{moy}\right|^2\right) + \frac{ab}{4\eta}\sum_{m=1}^{M}\sum_{n=1}^{N}\left(\left|E_{mnx}\right|^2 + \left|E_{mny}\right|^2\right) \qquad \text{(I-5)}$$

The average of the power coupled by a large number of identical electric probes located on the periphery of a waveguide can be approximated by

---

* Asterisk indicates the complex conjugate.

$$P_p = \frac{ab}{2\eta\delta C}\left\{\frac{1}{a}\int_0^a \left|E_y\right|^2_{y=0} dx + \frac{1}{a}\int_0^a \left|E_y\right|^2_{y=b} dx + \frac{1}{b}\int_0^b \left|E_x\right|^2_{x=0} dy + \frac{1}{b}\int_0^b \left|E_x\right|^2_{x=a} dy\right\} \qquad \text{(I-6)}$$

where δ is a constant to be determined and where

E = electric field in the waveguide at a probe location,

E_p = electric field coupled by the probe,

and

$$C = \frac{\left|E\right|^2}{\left|E_p\right|^2}$$

When equations I-2 and I-3 are substituted in equation I-6 and the integrations performed, the result is

$$P_p = \frac{ab}{4\eta\delta C}\left(\sum_{n=1}^{N}\left|E_{onx}\right|^2 + \sum_{m=1}^{M}\left|E_{moy}\right|^2\right) + \frac{ab}{4\eta\delta C}\sum_{n=1}^{N}\sum_{m=1}^{M}\left(\left|E_{mnx}\right|^2 + \left|E_{mny}\right|^2\right) + \frac{ab}{8\eta\delta C}\sum_{m=0}^{M}\left\{\sum_{n_2=0}^{N}\sum_{n_1=0}^{N} E_{mn_1y}\, E^*_{mn_2y}\left[1 + (-1)^{n_1+n_2}\right]\right\} + \frac{ab}{8\eta\delta C}\sum_{n=0}^{N}\left\{\sum_{m_1=0}^{M}\sum_{m_2=0}^{M} E_{m_1nx}E^*_{m_2nx}\left[1 + (-1)^{m_1+m_2}\right]\right\} \qquad \text{(I-7)}$$

A comparison of equations I-5 and I-7 shows that the first two terms of equation I-7 are very similar to the power, P, in the waveguide. Disregarding the second two terms of equation I-7 momentarily and defining

$$E' = \sum_{n=1}^{N}\left|E_{onx}\right|^2 + \sum_{m=1}^{M}\left|E_{moy}\right|^2 \qquad \text{(I-8)}$$

$$E'' = \sum_{n=1}^{N}\sum_{m=1}^{M}\left(\left|E_{mnx}\right|^2 + \left|E_{mny}\right|^2\right) \qquad \text{(I-9)}$$

---

* Asterisk indicates the complex conjugate.

the ratio of CP_p to P is

$$\frac{CP_p}{P} = \frac{\frac{1}{2\delta}(E' + E'')}{\left(E' + \frac{E''}{2}\right)} \qquad \text{(I-10)}$$

If E'' is zero (no power in modes with neither m nor n zero), the waveguide power will be

$$P = CP_p \qquad \left(\delta = \frac{1}{2}\right) \qquad \text{(I-11)}$$

If E' is zero (no power in modes with either m or n zero), the waveguide power will be

$$P = CP_p \qquad (\delta = 1) \qquad \text{(I-12)}$$

In general, the ratio of E'' to E' can not be known exactly; however, a value of δ can be chosen that will minimize the error in

$$P = C_p P_p \qquad \text{(I-13)}$$

where

$$C_p \equiv \delta_{opt}\, C.$$

This optimum value of δ, δ_{opt}, is chosen for the range of E''/E' that is expected in practice. If it is assumed that the range of E''/E' is from 0 to 2, then*

$$\delta_{opt} = 0.612 \qquad \text{(I-14)}$$

---

* δ_{opt} has been calculated by the method used in Appendix V.

Using this value for δ, the maximum error for the range from 0 to 2 is ± 0.88 db.

Data on the modal power distribution of two magnetrons is quoted in reference 12. The first case is the third harmonic of an S-band magnetron, where E''/E' is 0.126. Using $\delta_{opt} = 0.612$, the error would be -0.63 db. The second case is the fifth harmonic of an L-band magnetron, where E''/E' is 1.37. Using the same δ_{opt}, the error would be 0.60 db.

With equation I-13, the first two terms of equation I-8 may be identified as P/C_p, and equation I-13 then becomes

$$P_p = \frac{P}{C_p} + \mathcal{E} \qquad \text{(I-15)}$$

where $\mathcal{E}$ represents the remaining terms in equation I-7. The terms in $\mathcal{E}$ are error terms, since they cause the power computed from equation I-14 to differ from the waveguide power.

The first error term is

$$\frac{\mathcal{E}}{1} = |E_{01x}||E_{21x}| \cos\left[\phi_1 + (\beta_{21} - \beta_{01})\, \ell\right] \qquad \text{(I-16)}$$

where

ϕ_1 = initial phase difference between E_{01x} and E_{21x}

β_{01}, β_{21} = phase constants of the 0,1 and 2,1 modes

ℓ = length of S-band waveguide

The cutoff frequency of the 2,1 mode in S-band waveguide is 6.06 kMc. Hence, below this frequency, $\mathcal{E}$ is zero and equation I-13 can be used directly to compute the waveguide power from a single measurement of P_p. Above 6.06 kMc, the 0,1 and 2,1 modes can exist in S-band waveguide. If the

transmitting tube-to-waveguide transistion launches these modes, $\mathcal{E}_1$ will not be zero. However, since $\mathcal{E}$ is the only term in equation I-15 that depends on ℓ, $\mathcal{E}_1$ can be made to cancel. If a line stretcher in the S-band waveguide (which is dispersive) is adjusted to obtain the maximum and minimum values of P_p, the result is

$$P_{p\ max} = \frac{P}{C_p} + \mathcal{E}_1 \qquad \text{(I-17)}$$

$$P_{p\ min} = \frac{P}{C_p} = \mathcal{E}_1 \qquad \text{(I-18)}$$

Averaging these two equations causes $\mathcal{E}_1$ to cancel and the result is equation I-13, where P_p is now interpreted as the peak-to-dip average $(P_{p\ max} + P_{p\ min})/2$.

Above 7.65 kMc, the second error term

$$\frac{\mathcal{E}}{2} = |E_{11x}|\,|E_{31x}| \cos\left[\phi_2 + (\beta_{31} - \beta_{11})\,\ell\right] \qquad \text{(I-19)}$$

can exist in the S-band waveguide. At 10 kMc, it is possible to have seven error terms. However, in a practical measurement, it is unlikely that all of them will have sufficient amplitude to cause an appreciable error. In particular, modes whose m indices are even will not be launched by symmetrical coaxial-to-waveguide transitions that are located in the center of the broad wall of the waveguide. Furthermore, modes that are close to their cutoff frequency are difficult to launch. For these reasons, it is believed that, in practice, one error term will be dominant, and the use of the line stretcher to obtain the peak-to-dip average will result in accurate power measurements.

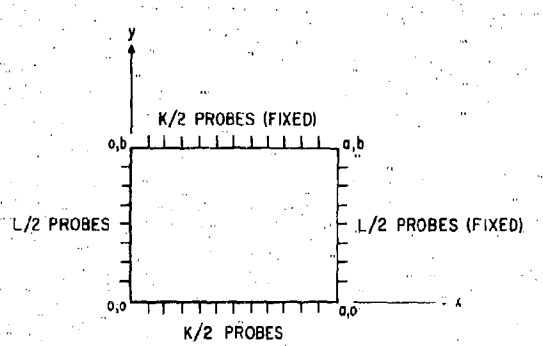

FIGURE I-1. CROSS SECTION OF ENLARGED WAVEGUIDE WITH FIXED PROBES

APPENDIX II

POWER FLOW IN MULTIMODE RECTANGULAR WAVEGUIDE

This appendix derives the expression for the total incident power flowing in a rectangular waveguide that contains an arbitrary set of TE and TM modes. Total power is obtained from integration of the Poynting vector. To solve for the incident power, we assume that the E and H fields are measured when the waveguide termination is matched for all modes.

The coordinate system is shown in Figure II-1. The time-average power flow in the z direction is given by

$$P = \int_0^b \int_0^a \left[\mathrm{Re}\ \bar{E} x \bar{H}^*\right] \cdot \bar{z} dxdy \qquad \text{(II-1)}$$

where $\bar{E}$ and $\bar{H}$ are the rms values of the electric and magnetic fields, respectively, and $\bar{z}$ is a unit vector in the z direction.

Expanding the fields into their components, gives the following simplification to equation II-1:

$$P = \int_0^b \int_0^a \mathrm{Re}(E_x H_y^* - E_y H_x^*) dxdy \qquad \text{(II-2)}$$

We desire an expression that gives P in terms of the E fields only. This is obtained by eliminating H by means of the Maxwell equation

$$\nabla x \bar{E} = -j\omega\mu\bar{H} \qquad \text{(II-3a)}$$

This generates the following relationships:

$$H_x = -\frac{1}{j\omega\mu}\left(\frac{\partial E_z}{\partial y} - \frac{\partial E_y}{\partial z}\right) \qquad \text{(II-3b)}$$

and

$$H_y = -\frac{1}{j\omega\mu}\left(\frac{\partial E_x}{\partial z} - \frac{\partial E_z}{\partial x}\right) \qquad \text{(II-3c)}$$

Substituting the above H_x and H_y expressions in equation II-2 gives the result for power flow in a rectangular waveguide:

$$P = \mathrm{Re}\,\frac{1}{j\omega\mu}\int_0^b\int_0^a\left[E_x\left(\frac{\partial E_x}{\partial z}\right)^* + E_y\left(\frac{\partial E_y}{\partial z}\right)^*\right]dxdy$$

$$-\mathrm{Re}\,\frac{1}{j\omega\mu}\int_0^b\int_0^a\left[E_x\left(\frac{\partial E_z}{\partial x}\right)^* + E_y\left(\frac{\partial E_z}{\partial y}\right)^*\right]dxdy \qquad \text{(II-4)}$$

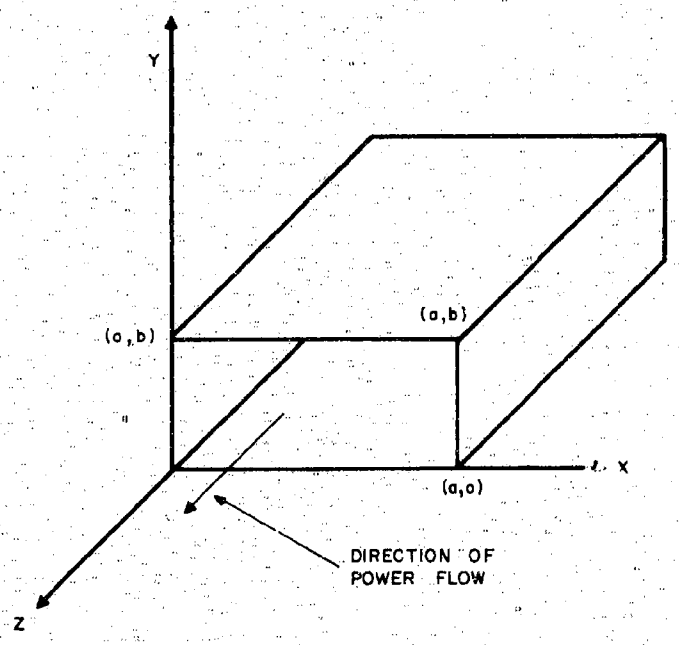

FIGURE II-1. COORDINATE SYSTEM FOR RECTANGULAR WAVEGUIDE

APPENDIX III

POWER FLOW IN ENLARGED WAVEGUIDE

This appendix shows that the general expression for power flow in arbitrarily large rectangular waveguide (equation II-4) reduces to

$$P = \frac{1}{\eta} \int_0^b \int_0^a \left(|E_x|^2 + |E_y|^2 \right) dxdy \qquad \text{(III-1)}$$

where η is the intrinsic impedance, 120π for free space.

Expressions for the error using equation III-1 are also derived.

Let us first examine the first two terms of equation II-4.

$$I_1 = \mathrm{Re}\, \frac{1}{j\omega\mu} \int_0^b \int_0^a \left[E_x \left(\frac{\partial E_x}{\partial z} \right)^* + E_y \left(\frac{\partial E_y}{\partial z} \right)^* \right] dxdy \qquad \text{(III-2)}$$

For a given mode, $\frac{\partial E_x}{\partial z}^* = j\frac{2\pi}{\lambda_g} E_x$ and $\frac{\partial E_y}{\partial z} = j\frac{2\pi}{\lambda_g} E_y$ (λ_g is the guide wavelength). If the highest-order propagating mode is limited to that consistent with the standard guide, λ_g will approach the free-space wavelength λ, if the wave is tapered to an arbitrarily large guide. This enables us to say that

$$I_1 = \frac{2\pi}{\omega\mu\lambda} \int_0^b \int_0^a \left(|E_x|^2 + |E_y|^2 \right) dxdy \qquad \text{(III-3)}$$

Since λ is the same for any mode, equation III-3 need not be separately integrated for each mode. By noting that $\omega\lambda = 2\pi(\mu\epsilon)^{-1/2}$, equation III-3 reduces to

$$I_1 = \frac{1}{\eta}\int_0^b\int_0^a \left(\left|E_x\right|^2 + \left|E_y\right|^2\right)dxdy \qquad \text{(III-4)}$$

The right-hand side of equation III-4 is identical with the right-hand side of equation III-1. This implies that the latter two terms of equation II-4 must be zero. That is,

$$I_2 = \mathrm{Re}\,\frac{1}{j\omega\mu}\int_0^b\int_0^a \left[E_x\left(\frac{\partial E_z}{\partial x}\right)^* + E_y\left(\frac{\partial E_z}{\partial y}\right)^*\right]dxdy = 0 \qquad \text{(III-5)}$$

We will show that I_2 must approach zero as the waveguide cross-section approaches infinity.

Examination of I_2 shows that only TM modes could contribute. We should therefore evaluate I_2 for a typical TM mode, and take the limit as a and b approach infinity. The expression for the electric field components of a TM_{mn} mode is:

$$E_x = -\frac{2V_1}{a}\,\frac{m}{\sqrt{m^2b/a + n^2a/b}}\cos\frac{m\pi x}{a}\sin\frac{n\pi y}{b}$$

$$E_y = -\frac{2V_1}{b}\,\frac{n}{\sqrt{m^2b/a + n^2a/b}}\sin\frac{m\pi x}{a}\cos\frac{n\pi y}{b} \qquad \text{(III-6)}$$

$$E_z = -\frac{jV_1\lambda_g}{ab}\sqrt{m^2b/a + n^2a/b}\,\sin\frac{m\pi x}{a}\sin\frac{n\pi y}{b}$$

where V_1 is the mode-voltage amplitude for a particular mode.

We can obtain $\frac{\partial E_z}{\partial x}$ and $\frac{\partial E_z}{\partial y}$ from the preceding;

$$\frac{\partial E_z}{\partial x} = \frac{-jV_1\lambda_g m\pi}{a^2 b} \sqrt{m^2 b/a + n^2 a/b} \cos\frac{m\pi x}{a} \sin\frac{n\pi y}{b}$$

and

$$\frac{\partial E_z}{\partial y} = \frac{-jV_1\lambda_g n\pi}{ab^2} \sqrt{m^2 b/a + n^2 a/b} \sin\frac{m\pi x}{a} \sin\frac{n\pi y}{b} \qquad \text{(III-7)}$$

Substituting equations III-6 and III-7 into equation III-5 gives

$$I_2 = \frac{1}{\omega\mu}\int_0^b\int_0^a \left[\frac{2m^2\pi V_1^2\lambda_g}{a^3 b}\cos^2\frac{m\pi x}{a}\sin^2\frac{n\pi y}{b} + \frac{2n^2\pi V_1^2\lambda_g}{ab^3}\sin^2\frac{m\pi x}{a}\cos^2\frac{n\pi y}{b}\right]dxdy = \frac{\pi}{2}\frac{V_1^2\lambda_g}{\omega\mu}\left[\frac{m^2}{a^2} + \frac{n^2}{b^2}\right]$$

(III-8)

Equation III-8 shows that $I_2 \longrightarrow 0$ as a and $b \longrightarrow \infty$ for finite m, n, and λ_g. Since the gradual tapered section connecting the large waveguide section to the standard size guide will preserve the bounded modal content of the standard guide, the condition of finite m and n is fully justified. λ_g must be finite because it approaches the value of λ in the large guide. We have therefore proved that equation III-1 is correct.

Since, in practice, we are limiting the a and b dimensions of the large guide to about three times the standard guide values, it is essential to show that the error in using equation III-1 is small. The error can be estimated by taking the worst case of a mode that is just slightly above cutoff in the standard guide and comparing the exact power flow (equation II-4) with that predicted by equation III-1. This error will be an upper bound because most of the other modes will be far from cutoff (closer to a plane-wave condition).

Substituting equation III-6 in equation III-1, and performing the indicated integrations, gives $P = V_1^2/\eta$ for the ideal plane-wave case. Substituting equations III-6 and III-7 in equation II-4 gives the exact power flow for a given TM mode.

$$I_1 + I_2 = \frac{V_1^2}{\eta}\left[\frac{\lambda}{\lambda g} + \frac{\lambda g \lambda}{4}\left(\frac{m^2}{a^2} + \frac{n^2}{b^2}\right)\right] = \frac{V_1^2}{\eta}\left[1 - \left(\frac{f_c}{f}\right)^2\right]^{-1/2} \tag{III-9}$$

The fractional error is

$$\epsilon_{TM} = \frac{\frac{V_1^2}{\eta}\left\{1 - \left[1 - \left(\frac{f_c}{f}\right)^2\right]^{-1/2}\right\}}{\frac{V_1^2}{\eta}\left[1 - \left(\frac{f_c}{f}\right)^2\right]^{-1/2}} = \left[1 - \left(\frac{f_c}{f}\right)^2\right]^{1/2} - 1 \approx -1/2\left(\frac{f_c}{f}\right)^2 \text{ for } \frac{f_c}{f} << 1 \tag{III-10}$$

A similar analysis for a TE mode would give a fractional error of

$$\epsilon_{TE} = \left[1 - \left(\frac{f_c}{f}\right)^2\right]^{-1/2} - 1 \approx +1/2\left(\frac{f_c}{f}\right)^2 \text{ for } \frac{f_c}{f} << 1 \tag{III-11}$$

We can now evaluate the error for enlarged guide three times the size of a standard guide. The maximum error occurs for $\frac{f_c}{f} = 1/3$. Substitution of $\frac{f_c}{f} = 1/3$ in either equation III-10 or III-11 predicts an error of 6 percent.

APPENDIX IV

DETERMINATION OF AVERAGE PROBE POWER USING A COMMUTATOR-AVERAGING TECHNIQUE

A method for automatically determining the average of the power coupled by the probes is described. Automatic sampling of the probe power can be achieved with a continuously rotating commutator. The equations describing the operation of the commutator are derived.

It will be assumed that the angular transmission function is exactly the same for each commutator segment. This transmission function is shown in Figure IV-1.

Since the segments are identical, rotating the commutator through 360 degrees results in the total-commutator transmission function shown in Figure IV-2.

The output power of the jth commutator segment is

$$P_{oj} = T(\theta)P_{ij}$$

where

P_{ij} = input power from the jth probe ($j = 1, 2, \ldots J$),
$T(\theta)$ = transmission function of a segment,
θ = angle of wiper arm from any convenient reference point.

The input power will be different for each probe. The output power of all the commutator segments is shown in Figure IV-3. The total area under this curve is

$$A = \int_0^{2\pi} P_{i1}\, T(\theta)d\theta + \int_0^{2\pi} P_{i2}\, T(\theta)d\theta + \ldots + \int_0^{2\pi} P_{ij}\, T(\theta)d\theta$$

$$= \left(P_{i1} + P_{i2} + \ldots + P_{ij}\right) \int_0^{2\pi} T(\theta)d\theta \qquad \text{(IV-1)}$$

$$= P_p \int_0^{2\pi} T(\theta)d\theta$$

$$P_p = \frac{A}{\int_0^{2\pi} T(\theta)d\theta} \qquad \text{(IV-2)}$$

If an average-reading meter is used to read the average value, Q, of the commutator output power over one cycle, then

$$A = 2\pi Q \qquad \text{(IV-3)}$$

Therefore

$$P_p = \frac{2\pi Q}{\int_0^{2\pi} T(\theta)d\theta} \qquad \text{(IV-4)}$$

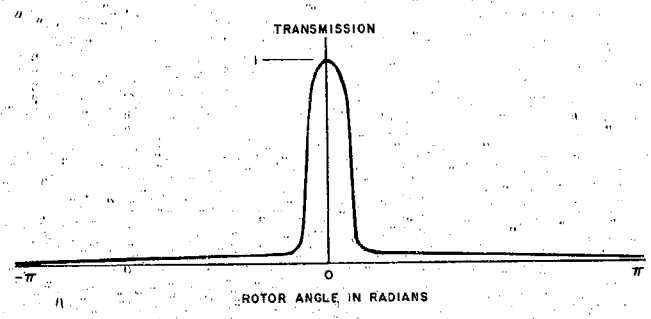

FIGURE IV-1. TRANSMISSION AS A FUNCTION OF ROTOR ANGLE FOR A SINGLE COMMUTATOR SEGMENT

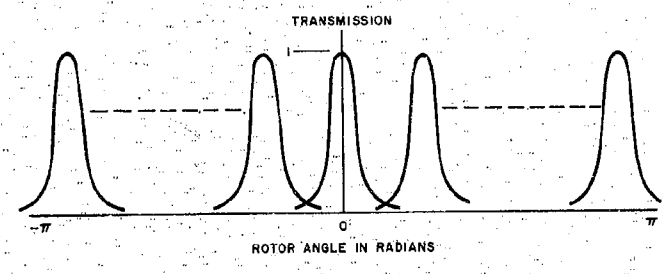

FIGURE IV-2. TRANSMISSION AS A FUNCTION OF ROTOR ANGLE FOR ALL COMMUTATOR SEGMENTS

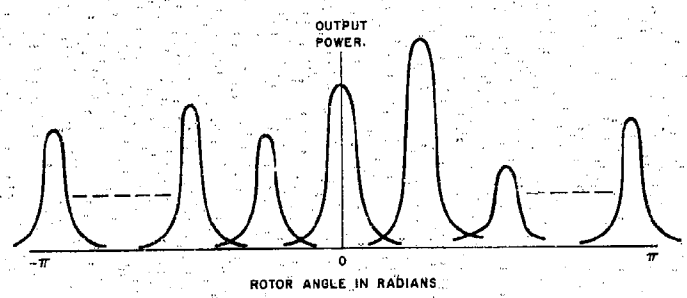

FIGURE IV-3. OUTPUT POWER AS A FUNCTION OF ROTOR ANGLE FOR ALL COMMUTATOR SEGMENTS

APPENDIX V
COMMUTATOR AVERAGING CORRECTION

In a new method for averaging the power coupled by the fixed probes, the sum of the power coupled by all the probes is divided by the total number of probes. This method is readily adaptable to automation.

In the original method, the average of the coupled power is

$$P_p = \frac{1}{2}\left(\frac{P_b}{K} + \frac{P_n}{L}\right) \qquad \text{(V-1)}$$

where

P_b = sum of powers coupled by broad-wall probes
P_n = sum of powers coupled by narrow-wall probes
K = number of broad-wall probes, 22
L = number of narrow-wall probes, 14

When a series of manually operated switches is used for sampling, P_b and P_n can be measured separately, and, after division by the appropriate constant, P_p is computed.

The system is automated by replacing the switches by a rotating commutator. It is not now possible to average the broad-wall and narrow-wall powers separately. An average can be obtained by using

$$P_p' = \frac{1}{2}\left(\frac{P_b + P_n}{K + L}\right) \qquad \text{(V-2)}$$

Clearly, P_p' is not the same as P_p. To minimize the discrepancy, P_p' is multiplied by a constant $\frac{1}{\xi}$, which can be optimized

for the range of powers expected. The error is

$$D = \frac{P_p'}{P_p} = \frac{\frac{1}{2\xi}\left(\frac{P_b + P_n}{K + L}\right)}{\frac{1}{2}\left(\frac{P_b}{K} + \frac{P_n}{L}\right)} \qquad \text{(V-3)}$$

$$D = \frac{K(R + 1)}{\xi(K + L)(R + \frac{K}{L})} \qquad \text{(V-4)}$$

where R is $\frac{P_b}{P_n}$.

Measurements made to date indicate that values of R between 2 and 100 will be satisfactory for most cases. If ξ is now chosen to make the logarithmic error 10 log D, equal in magnitude and opposite in sign for R = 2 and R = 100, then

$$\frac{K(100 + 1)}{\xi(K + L)(100 + \frac{K}{L})} = \frac{\xi(K + L)(2 + \frac{K}{L})}{K(2 + 1)} \qquad \text{(V-5)}$$

from which

$$\xi = 0.560$$

and

$$D = 1.092\,\frac{R + 1}{R + 1.57} \qquad \text{(V-6)}$$

For R = 2

$$D = 0.915 \qquad \text{or } -0.37 \text{ db}$$

For R = 100

$$D = 1.083 \qquad \text{or } +0.37 \text{ db}$$

The error is zero at R = 5.33 and is maximum at R = 2 and R = 100.

For the commutator,

$$P_p' = \frac{P_b + P_n}{2\xi(K + L)} = 0.0248(P_b + P_n) \qquad \text{(V-7)}$$

The sum of all the powers sampled by the commutator must therefore be multiplied by 0.0248 to give an indication which differs from the true average by 0.37 db or less.

APPENDIX VI

DERIVATION OF RECEIVER NOISE FIGURE AND BANDWIDTH PRODUCT

Let V_{noise} be the voltage which, when applied to tne input terminals of the receiver, will produce a receiver output power equal to the receiver output noise power. Also, let V_x and V_y be the voltages presented to the input terminals of the receiver by two probes coupling to E_x and E_y in the waveguide.

As shown in Appendix III

$$P_z = \sqrt{\frac{\epsilon}{\mu}} \int_o^b \int_o^a \left(|E_x|^2 + |E_y|^2 \right) dxdy \qquad \text{(VI-1)}$$

$$= \sqrt{\frac{\epsilon}{\mu}} \frac{1}{k_p^2} \int_o^b \int_o^a \left(V_x^2 + Y_y^2 \right) dxdy \qquad \text{(VI-2)}$$

where

$$V_x = k_p \, |E_x|$$

$$V_y = k_p \, |E_y|$$

To obtain an upper bound on the error, assume an E-field distribution such as with the TE_{30} mode (Figure VI-1). An ideal (noiseless) receiver will reproduce this distribution with no error. With receiver noise present, however,

the receiver output is greater (Figure VI-2). The difference between the two outputs depends on the E-field distribution; the more times the probed voltage drops below the noise level, the greater the error. An upper limit on the error is obtained by assuming that the noise is contributing along the entire waveguide cross section.

The power in the guide has been shown to be

$$P = \sqrt{\frac{\epsilon}{\mu}} \int_0^b \int_0^a \left(\left| E_x \right|^2 + \left| E_y \right|^2 \right) dxdy$$

Substituting

$$V_x = k_p \left| E_x \right|$$

$$V_y = k_p \left| E_y \right|$$

$$P = \sqrt{\frac{\epsilon}{\mu}} \frac{1}{k_p^2} \int_0^b \int_0^a \left(V_x^2 + V_y^2 \right) dxdy \qquad \text{(VI-3)}$$

For an upper limit on the error, V_{noise}^2 is integrated over the guide cross section, resulting in

$$P_{noise} = \sqrt{\frac{\epsilon}{\mu}} \frac{1}{k_p^2} \int_0^b \int_0^a \left(V_{noise}^2 + V_{noise}^2 \right) dxdy$$

$$= 2 \sqrt{\frac{\epsilon}{\mu}} \frac{V_{noise}^2}{k_p^2} ab \qquad \text{(VI-4)}$$

but

$$V^2_{noise} = kTBFR_c \qquad \text{(VI-5)}$$

where

k = Boltzmann's constant,
T = temperature in degrees Kelvin,
B = receiver bandwidth,
F = receiver noise figure,
R_c = receiver input resistance.

Substituting equation VI-5 in equation VI-4,

$$P_{noise} = \frac{2ab}{k_p^2}\sqrt{\frac{\epsilon}{\mu}}\ kTBFR_c \qquad \text{(VI-6)}$$

The error in the power measurement is defined as

$$E = -10 \log \frac{P_z^1}{P_z}$$

where

P_z^1 = power measured if P_{noise} is neglected,
P_z = true power.

Since

$$P_z^1 = P_z - P_{noise}$$

$$E = -10 \log \left(1 - \frac{P_{noise}}{P_z}\right) \qquad \text{(VI-7)}$$

Substituting equation VI-6 in equation VI-7,

$$1 - 10^{-E/10} = 2ab \sqrt{\frac{\epsilon}{\mu}} \frac{kTBFZ_c}{k_p^2 P_z}$$

or

$$BF = \frac{\left(1 - 10^{-E/10}\right) P_z k_p^2}{2ab \sqrt{\frac{\epsilon}{\mu}} kTR_c} \qquad \text{(VI-8)}$$

The probe coupling constant k_p will now be related to the more easily measurable insertion loss of the same probe located at the center of the broad wall of a guide propagating power in the dominant mode only. The insertion loss L is defined as

$$L = 10 \log \frac{P}{P_c} \qquad \text{(VI-9)}$$

where

P = power propagating in waveguide,
P_c = power coupled to coaxial line by the probe.

Now

$$P_c = \frac{\left|V_c\right|^2}{R_c} \qquad \text{(VI-10)}$$

Substituting equation VI-2 in equation VI-9,

$$P_c = k_p^2 \frac{E_{max}^2}{R_c} \qquad \text{(VI-11)}$$

where E_{max} is RMS value of the electric field strength at the center of the guide.

But

$$E_{max}^2 = \frac{2P}{ab\sqrt{\frac{\epsilon}{\mu}}} \qquad \text{(VI-12)}$$

if the dominant mode is far above cutoff. Therefore, by equations VI-10, VI-11, and VI-9,

$$\frac{P}{P_c} = \frac{ab}{2}\sqrt{\frac{\epsilon}{\mu}}\,\frac{R_c}{k_p^2} = 10^{L/10} \qquad \text{(VI-13)}$$

or

$$k_p^2 = \frac{ab}{2}\sqrt{\frac{\epsilon}{\mu}}\,\frac{R_c}{10^{L/10}}. \qquad \text{(VI-14)}$$

Substituting equation VI-14 in equation VI-8,

$$BF = \frac{\left(1 - 10^{-F/10}\right) P_z}{4kT\ 10^{L/10}}. \qquad \text{(VI-15)}$$

If P_z is set equal to the minimum power level which is required to be detected,

$$BF = \frac{\left(1 - 10^{-E/10}\right) P_{min}}{4kT\ 10^{L/10}} \qquad \text{(VI-16)}$$

gives the maximum permissible noise figure and bandwidth product of the receiver.

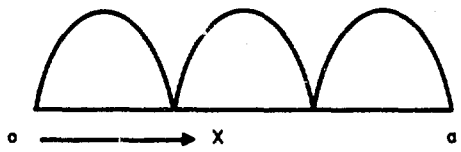

FIGURE VI-1. E-FIELD DISTRIBUTION WITH TE_{30}

FIGURE VI-2. RECEIVER OUTPUT WHEN NOISE IS PRESENT IN RECEIVER

APPENDIX VII

DIFFERENCE BETWEEN TOP-WALL AND BOTTOM-WALL ELECTRIC FIELDS FOR TE_{10}- AND TE_{51}-MODE PROPAGATION

Expressions will be derived for the top-wall and bottom-wall electric fields with TE_{10}- and TE_{51}-mode propagation in terms of the ratio of top-wall to side-wall maximum field amplitude. The TE_{51} mode was chosen since it can exist in the enlarged guide at frequencies at which appreciable differences between the top-wall and bottom-wall fields were observed despite very small contributions from the side-wall probes. Furthermore, the appearance of the field plots suggested a mode with a relatively high m index.

Assume the existence of the TE_{10} and TE_{51} modes in time phase. The field components are

$$E_{10y} = -\frac{A_{10}}{a} \sin \alpha \qquad \text{(VII-1)}$$

$$E_{51y} = -\frac{A_{51}}{a} (5) \sin 5\alpha \cos \beta \qquad \text{(VII-2)}$$

$$E_{10x} = 0 \qquad \text{(VII-3)}$$

$$E_{51x} = \frac{A_{51}}{b} \cos 5\alpha \sin \beta \qquad \text{(VII-4)}$$

where

A_{10}, A_{51} = arbitrary amplitude factors of the TE_{10} and TE_{51} modes

a = wide dimension of waveguide

b = narrow dimension of waveguide

$\alpha = \frac{\pi x}{a}$ in radians

$\beta = \frac{\pi y}{b}$ in radians

At y = 0, the total electric field is

$$E_y\Big|_{y=0} = -\frac{1}{a}(A_{10} \sin \alpha + 5A_{51} \sin 5\alpha) \qquad \text{(VII-5)}$$

At y = b, the total electric field is

$$E_y\Big|_{y=b} = -\frac{1}{a}(A_{10} \sin \alpha - 5A_{51} \sin 5\alpha) \qquad \text{(VII-6)}$$

At y = 0, the maximum field occurs for $\alpha = \pi/2$.

$$E_{y\ max}\Big|_{y=0} = -\frac{1}{a}(A_{10} + 5A_{51}) \qquad \text{(VII-7)}$$

At x = a, the total electric field is

$$E_x = -\frac{A_{51}}{b} \sin \beta \qquad \text{(VII-8)}$$

The maximum field occurs for $\beta = \pi/2$

$$E_{x\ max}\Big|_{x=a} = -\frac{A_{51}}{b} \qquad \text{(VII-9)}$$

The ratio of the maximum top-wall electric field to the maximum side-wall electric field is

$$R \equiv \frac{E_{y\ max}\Big|_{y=0}}{E_{x\ max}\Big|_{x=a}} = \frac{b}{a}\left(\frac{A_{10}}{A_{51}} + 5\right) \qquad \text{(VII-10)}$$

From equation VII-10,

$$A_{51} = \frac{A_{10}}{\frac{aR}{b} - 5} \qquad \text{(VII-11)}$$

and from equation VII-7

$$E_{y\ max}\Big|_{y=0} = -\frac{A_{10}}{a}\,\frac{\frac{aR}{5b}}{\frac{aR}{5b} - 1} \qquad \text{(VII-12)}$$

Substituting equation VII-11 into equation VII-5 and VII-6 yields

$$E_y\Big|_{y=0} = -\frac{A_{10}}{a}\left(\sin\alpha + \frac{1}{\frac{aR}{5b} - 1}\sin 5\alpha\right) \qquad \text{(VII-13)}$$

$$E_y\Big|_{y=b} = -\frac{A_{10}}{a}\left(\sin\alpha - \frac{1}{\frac{aR}{5b} - 1}\sin 5\alpha\right) \qquad \text{(VII-14)}$$

Normalizing equations VII-12 and VII-13 with respect to equation VII-12 and simplifying yields

$$E_{yo} \equiv \frac{E_y\Big|_{y=0}}{E_{y\ max}\Big|_{y=0}} = \left(1 - \frac{5b}{aR}\right)\left(\sin\alpha + \frac{\sin 5\alpha}{\frac{aR}{5b} - 1}\right) \qquad \text{(VII-15)}$$

$$E'_{yb} \equiv \frac{E_y\Big|_{y=b}}{E_{y\ max}\Big|_{y=0}} = \left(1 - \frac{5b}{aR}\right)\left(\sin\alpha - \frac{\sin 5\alpha}{\frac{aR}{5b} - 1}\right) \qquad \text{(VII-16)}$$

Equations VII-15 and VII-16 are the expressions for the top-wall and bottom-wall electric-field strengths in terms of R. These equations have been computed for R equals 20 and 25 db, using the actual dimensions of the enlarged waveguide for a and b. The results of the computations are shown in Figures VII-1 and VII-2.

These figures show that, for a contribution from the side-wall probes that is small relative to that from the top-wall or bottom-wall probes, there can be enough E_y from a higher-order mode to cause considerable asymmetry in the top-wall and bottom-wall electric fields. For this asymmetry to occur, the mode index n of the higher-order mode must be odd.

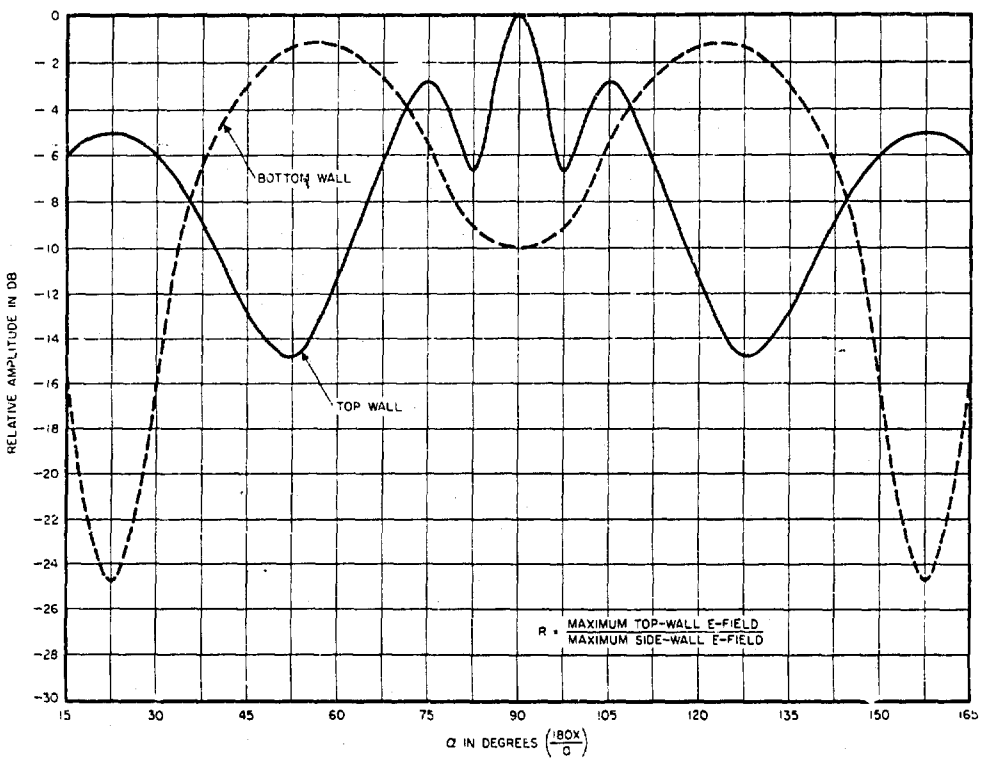

FIGURE VII-1. TE_{10} AND TE_{51} ELECTRIC-FIELD AMPLITUDE FOR R = 20 DB

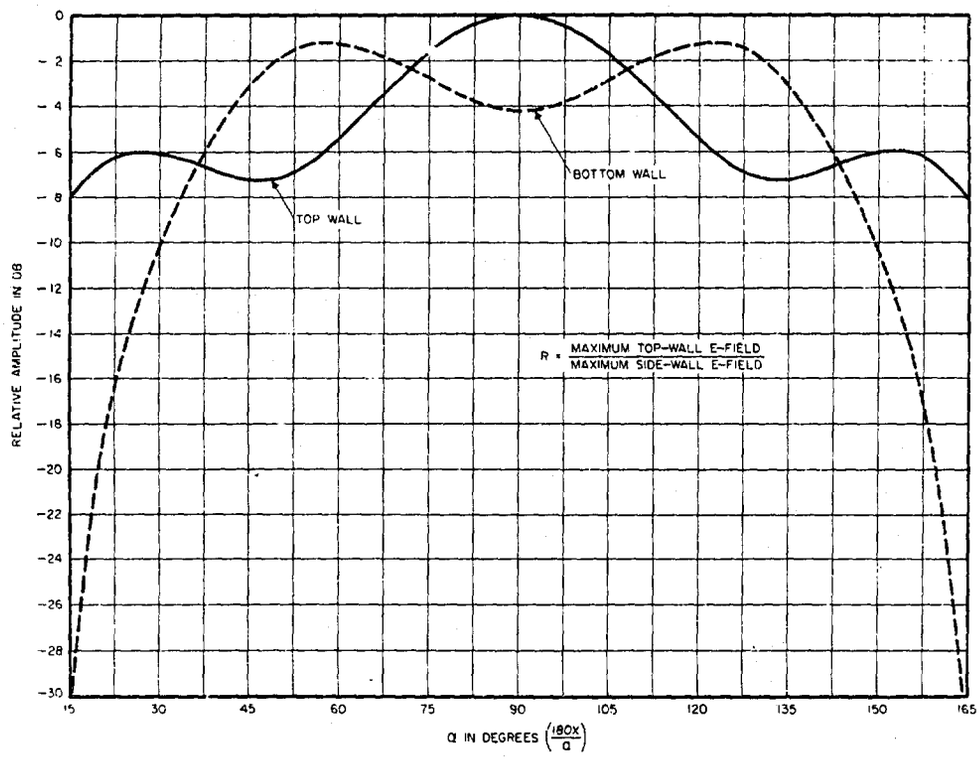

FIGURE VII-2. TE_{10} AND TE_{51} ELECTRIC-FIELD AMPLITUDE FOR R = 25 DB

APPENDIX VIII

MEASUREMENTS IN PRESENCE OF MULTIMODE MISMATCHES

An analysis of the power measured by the fixed probes in the presence of an arbitrary mismatched termination is given below. It is shown that power into a mismatched load can be measured by varying the phase of the load's reflection coefficient and the length of the dispersive line stretcher.

The electric field components in an oversize waveguide that is terminated in a multimode mismatched load (having reflection coefficients Γ_{mn}) is

$$E_x = \sum_{n=o}^{N} \sum_{m=o}^{M} E_{mn_x} \left[1 + \Gamma_{mn} \epsilon^{j2\beta_{mn}z} \right] \cos \frac{m\pi x}{a} \sin \frac{n\pi y}{b}$$

and (VIII-1)

$$E_y = \sum_{n=o}^{N} \sum_{m=o}^{M} E_{mn_y} \left[1 + \Gamma_{mn} \epsilon^{j2\beta_{mn}z} \right] \sin \frac{m\pi x}{a} \cos \frac{n\pi y}{b}$$

where

Γ_{mn} = the reflection coefficient for the mn mode at z = o;

β_{mn} = the propagation constant for the mn mode.

The true power delivered to the multimode mismatch is the sum of the absorbed power in each mode, which is

$$P = \frac{ab}{4\eta} \sum_{m=o}^{M} \sum_{n=o}^{N} \left[|E_{mn_x}|^2 (1 + \delta_{on}) + |E_{mn_y}|^2 (1 + \delta_{mo}) \right] \left[1 - |\Gamma_{mn}|^2 \right] \quad \text{(VIII-2)}$$

where δ_{on} and δ_{mo} are Kronecker deltas that are zero for all modes but on and mo.

Let us now evaluate the information gained from the fixed-probe averages taken with a sliding termination. The boundary fields are

$$E_{\substack{x \\ x=o}} = \sum_{n=o}^{N} \sum_{m=o}^{M} E_{mn_x} \left[1 + |\Gamma_{mn}| \, \epsilon^{j\phi_{mn}} \right] \sin \frac{n\pi y}{b}$$

$$E_{\substack{x \\ x=a}} = \sum_{n=o}^{N} \sum_{m=o}^{M} E_{mn_x} (-1)^m \left[1 + |\Gamma_{mn}| \, \epsilon^{j\phi_{mn}} \right] \sin \frac{n\pi y}{b} \quad \text{(VIII-3)}$$

and

$$E_{\substack{y \\ y=o}} = \sum_{n=o}^{N} \sum_{m=o}^{M} E_{mn_y} \sin \frac{m\pi x}{a} \left[1 + |\Gamma_{mn}| \, \epsilon^{j\phi_{mn}} \right]$$

$$E_{\substack{y \\ y=b}} = \sum_{n=o}^{N} \sum_{m=o}^{M} E_{mn_y} (-1)^n \sin \frac{m\pi x}{a} \left[1 + |\Gamma_{mn}| \, \epsilon^{j\phi_{mn}} \right] \quad \text{(VIII-4)}$$

where

$$\phi_{mn} = 2\beta_{mn} z + \psi_{mn},$$

$$\psi_{mn} = \text{the phase of } \Gamma_{mn}.$$

These fields can also be expressed as

$$E_{x_{x=o}} = \sum_{n=o}^{N} E_n \sin \frac{n\pi y}{b}, \quad E_{x_{x=a}} = \sum_{n=o}^{N} E_n^1 \sin \frac{n\pi y}{b}$$

$$E_{y_{y=o}} = \sum_{m=o}^{M} E_m \sin \frac{m\pi x}{a}, \quad E_{y_{y=b}} = \sum_{m=o}^{M} E_m^1 \sin \frac{m\pi x}{a} \qquad \text{(VIII-5)}$$

where

$$E_n = \sum_{m=o}^{M} E_{mn_x} \left[1 + |\Gamma_{mn}| \, \epsilon^{j\phi_{mn}}\right]; \quad E_n^1 = \sum_{m=o}^{M} (-1)^m E_{mn_x} \left[1 + |\Gamma_{mn}| \, \epsilon^{j\phi_{mn}}\right]$$

$$E_m = \sum_{n=o}^{N} E_{mn_y} \left[1 + |\Gamma_{mn}| \, \epsilon^{j\phi_{mn}}\right]; \quad E_m^1 = \sum_{n=o}^{N} (-1)^n E_{mn_y} \left[1 + |\Gamma_{mn}| \, \epsilon^{j\phi_{mn}}\right]$$

Assuming a large number of sampling probes on all four walls, the average power is

$$
\begin{aligned}
P_p = \frac{ab}{4\delta C\eta} \Bigg\{ & \sum_{n=1}^{N} \left|E_{on_x}\right|^2 \left[1 + \left|\Gamma_{on}\right|^2 + 2\left|\Gamma_{on}\right| \cos\left(2\beta_{on}z + \psi_{on}\right)\right] \\
& + \sum_{m=1}^{M} \left|E_{mo_x}\right|^2 \left[1 + \left|\Gamma_{mo}\right|^2 + 2\left|\Gamma_{mo}\right| \cos\left(2\beta_{mo}z + \psi_{mo}\right)\right] \\
& + \sum_{n=1}^{N} \sum_{m=1}^{M} \left|E_{mn_x}\right|^2 \left[1 + \left|\Gamma_{mn}\right|^2 + 2\left|\Gamma_{mn}\right| \cos\left(2\beta_{mn}z + \psi_{mn}\right)\right] \\
& + \sum_{n=1}^{N} \sum_{m=1}^{M} \left|E_{mn_y}\right|^2 \left[1 + \left|\Gamma_{mn}\right|^2 + 2\left|\Gamma_{mn}\right| \cos\left(2\beta_{mn}z + \psi_{mn}\right)\right] \Bigg\} \\
& + \frac{ab}{8\delta C\eta} \sum_{m=o}^{M} \left\{ \sum_{n_2=o}^{N} \sum_{n_1=o}^{N} E_{mn_{1_y}} E^*_{mn_{2_y}} \left[1 + (-1)^{n_1+n_2}\right] \right\} \qquad \text{(VIII-6)} \\
& \left[1 + \left|\Gamma_{mn_1}\right| \left|\Gamma_{mn_2}\right| \epsilon^{j\left(2z\beta_{mn_1} + \psi_{mn_1} - 2z\beta_{mn_2} - \psi_{mn_2}\right)}\right. \\
& \left. + \left|\Gamma_{mn_1}\right| \epsilon^{j\left(2\beta_{mn_1}z + \psi_{mn_1}\right)} + \left|\Gamma_{mn_2}\right| \epsilon^{j\left(2\beta_{mn_2}z + \psi_{mn_2}\right)}\right] \\
& + \frac{ab}{8\delta C\eta} \sum_{n=o}^{N} \left\{ \sum_{m_1=o}^{M} \sum_{m_2=o}^{M} E_{m_1n_x} E^*_{m_2n_x} \left[1 + (-1)^{m_1+m_2}\right] \right\} \\
& \left[1 + \left|\Gamma_{m_1n}\right| \left|\Gamma_{m_2n}\right| \epsilon^{j\left(2z\beta_{m_1n} + \psi_{m_1n} - 2z\beta_{m_2n} - \psi_{m_2n}\right)}\right. \\
& \left. + \left|\Gamma_{m_1n}\right| \epsilon^{j\left(2\beta_{m_1n}z + \psi_{m_1n}\right)} + \left|\Gamma_{m_2n}\right| \epsilon^{j\left(2\beta_{m_2n}z + \psi_{m_2n}\right)}\right]
\end{aligned}
$$

Here again, the form of the result is the sum of $|E_{mn}|^2$ values plus cross-product terms of the form $E_{mn_1} E^*_{mn_2}$ The cross-product summation must be a real number but can be plus or minus. If the line stretcher is used in the standard-size waveguide, the cross-product terms will be minimized because of the equal likelihood of plus or minus real values. The remaining terms are still the squared ones (the first four summation expressions), which must always be real and positive.

The P_p expression is further simplified when the phases of the reflection coefficients are varied. This can be done by moving a line stretcher in the oversize waveguide located between the fixed-probe section and the mismatched load. The variation in P_p with the position of this line stretcher will be sinusoidal because all β_{mn}'s are, to a very good approximation, equal to the free space $\beta(\beta_o)$ in the oversize waveguide (provided that no new modes are generated in the oversize waveguide). The P_p expression (without the cross-product terms) is

$$P_p = \frac{ab}{4\delta C\eta} \sum_{m=o}^{M} \sum_{n=o}^{N} \left(|E_{mn_x}|^2 + |E_{mn_y}|^2\right) \left[1 + |\Gamma_{mn}|^2 + 2|\Gamma_{mn}| \cos\left(2\beta_o z - \psi_{mn}\right)\right] \quad \text{(VIII-7)}$$

which, after varying the oversize-waveguide line stretcher and taking the average value of P_p, gives

$$P_a = \frac{ab}{4\delta C\eta} \left\{ \sum_{m=o}^{M} \sum_{n=o}^{N} \left(|E_{mn_x}|^2 + |E_{mn_y}|^2\right) + \sum_{m=o}^{M} \sum_{n=o}^{N} |\Gamma_{mn}|^2 \left(|E_{mn_x}|^2 + |E_{mn_y}|^2\right) \right\} \quad \text{(VIII-8)}$$

Equation II-8 can be expressed as

$$P_a = P_M + P_R \qquad \text{(VIII-9)}$$

where

P_M = the power delivered to a multimode matched load,

P_R = the reflected power from the multimode mismatched termination.

We wish to measure the power absorbed by the mismatched termination, which is

$$P_T = P_M - P_R, \text{or } P_R = P_M - P_T \qquad \text{(VIII-10)}$$

Substitution of P_R from equation II-10 in equation II-9 gives

$$P_T = 2\ P_M - P_a \qquad \text{(VIII-11)}$$

DISTRIBUTION LIST FOR REPORT NO. 1112-1

Copy No.	Address	Number of Copies
1-4	* RADC (RAUMA, ATTN: L.F. Moses) Griffiss AFB, N.Y.	4
5	* RADC (RAAPT) Griffiss AFB, N.Y.	1
6	* RADC (RAALD) Griffiss AFB, N.Y.	1
7	* GEEIA (ROZMCAT) Griffiss AFB, N.Y.	1
8	* RADC (RAIS, ATTN: Mr. Malloy) Griffiss AFB, N.Y.	1
9	* U.S. Army Electronics R&D Labs Liaison Office RADC Griffiss AFB, N.Y.	1
10	* AUL (3T) Maxwell AFB, Alabama	1
11	ASD (ASAPRD) Wright-Patterson AFB, Ohio	1
12	Chief, Naval Research Lab ATTN: Code 2027 Washington 25, D.C.	1
13	RTD (RTGS) Bolling AFB Washington 25, D.C.	1
14	AFSC (SCSE) Andrews AFB Washington 25, D.C.	1

* Mandatory.

Reproduced From
Best Available Copy

DISTRIBUTION LIST FOR REPORT NO. 1112-1 (cont)

Copy No.	Address		Number of Copies
15	Commanding General US Army Electronics Proving Ground ATTN: Technical Documents Library Ft Huachuca, Arizona		1
16-25	* ASTIA (TISIA-2) Arlington Hall Station Arlington 12, Virginia	[If not releasable to ASTIA, IAW AFR 205-43, send the 10 copies to RADC (RAAPP-2) for secondary distribution]	Minimum of 10 copies
26	Hq USAF (AFCOA) Washington 25, DC		1
27	AFOSR (SRAS/Dr. G. R. Eber) Holloman AFB, New Mexico		1
28	Commander Naval Missile Center Tech Library (Code No. 3022) Pt Mugu, California		1
29	Redstone Scientific Information Center U.S. Army Missile Command Redstone Arsenal, Alabama		1
30	Commanding General White Sands Missile Range New Mexico ATTN: Technical Library		1
31	ESD (ESRL) L. G. Hanscom Fld Bedford, Massachusetts		1
32	APGC (PGAPI) Eglin AFB, Florida		1

* Mandatory.

Reproduced From
Best Available Copy

DISTRIBUTION LIST FOR REPORT NO. 1112-1 (cont)

Copy No.	Address	Number of Copies
33	AFSWC (SWOI) Kirtland AFB, New Mexico	1
34	Georgia Institute of Technology ATTN: Mr. Bruce Warren Atlanta 13, Georgia	1
35	American Electronics Laboratories, Inc. ATTN: Mr. C. J. Fowler Richardson Road Colmar, Pennsylvania	1
36	University of Pennsylvania ATTN: Prof. O. D. Salati 34 Walnut Street Philadelphia 4, Pennsylvania	1
37	USASRDL (Mr. S. Weitz) Ft Monmouth, New Jersey	1
38	Electro-Mechanics Co. ATTN: Dr. F. J. Morris and Mr. W. Cronenwett P.O. Box 802 Austin 64, Texas	1
39	Stanford Research Institute ATTN: Dr. L. Young Menlo Park, California	1
40	GEEIA (ROZMWT, Mr. D.R. Clark) Griffiss AFB, NY	1
41	Armour Research Foundation ATTN: Mr. B. Ebstein 10 West 35th Street Chicago, Illinois	1
42	ASD (ASRNCS-2, Mr. H. Bartman) Wright-Patterson AFB, Ohio	1
43-44	Electromagnetic Compatibility Analysis Center ATTN: Mr. Benjamin Lindeman U.S. Naval Engineering Experimental Station Annapolis, Maryland	2

Reproduced From
Best Available Copy

DISTRIBUTION LIST FOR REPORT NO. 1112-1 (cont)

Copy No.	Address	Number of Copies
45	RADC (RAUMM, Mr. Porter) Griffiss AFB, NY	1
46	Navy Air Navigation Electronic Project Weapons System Test Division (Mr. O. D. Stewart) Naval Air Test Center Patuxent River, Maryland	1
47	Radio Corporation of America ATTN: Mr. A. Matheson P.O. Box 588 Burlington, Massachusetts	1
48	Radiation Incorporated ATTN: Mr. W.F. Quinlivan P.O. Box 37 Melbourne, Florida	1
49	U.S. Naval Civil Engineering Laboratory ATTN: Mr. D. Clark Port Hueneme, California	1
50	Sperry Microwave Electronic Company Division of Sperry Rand Corporation ATTN: Mr. R.W. Smith Clearwater, Florida	1
51	Bendix Corporation Bendix Radio Division ATTN: Mr. A.E.F. Grempler Towson, Maryland	1
52	Jansky & Bailey ATTN: Mr. K. Heisler, Jr. 1339 Wisconsin Ave. N.W. Washington, D.C.	1
53	White Electromagnetic, Inc. ATTN: J.E. McShulskis 4903 Auburn Avenue Bethesda 14, Maryland	1
54	RADC (RAUMI, Mr. R. Powers) Griffiss AFB, N.Y.	1
55	RADC (RAUM, Mr. Zaccari) Griffiss AFB, N.Y.	1

Reproduced From
Best Available Copy

DISTRIBUTION LIST FOR REPORT NO. 1112-1 (cont)

Copy No.	Address	Number of Copies
56	ESD (ESRDV, Mr. Dix) L.G. Hanscom Fld Bedford, Massachusetts	1
57	AFSC (SCRC, Capt. Zimmerman) Andrews AFB Washington, D.C.	1
58	RTD (RTHE, Mr. S. Tepper) Bolling AFB Washington, D.C.	1

This Document
Reproduced From
Best Available Copy